Markovianity of Trabecular Networks

Dissertation

zur Erlangung des akademischen Grades
Doktor der Ingenieurwissenschaften
(Dr.-Ing.)
der Technischen Fakultät
der Christian-Albrechts-Universität zu Kiel

Wolfram Timm

Kiel
2006

1. Gutachter: Prof. Dr. G. Sommer

2. Gutachter: Prof. Dr. C.-C. Glüer

3. Gutachter: Prof. Dr. G. Pfister

Datum der mündlichen Prüfung: 6. Oktober 2006

To my wife Susanne

Abstract

Clinically established methods to diagnose osteoporosis, a systemic disease with multiple implications to the human's well being are bound to the bone mineral density. Since it is well known, that the bone structure changes under osteoporosis, this thesis investigates, whether structural changes represent information independent of bone mineral density, and whether this structural information, obtained by innovative mathematical techniques improves first the ability to distinguish between osteoporotic and healthy structures, second the measurement of a risk to belong to the osteoporotic group, and third the prediction of a biomechanical measure, the failure load, compared to existing standard structural measures. This in vitro study utilised mainly Micro-Computer Tomography (μ-CT) and for some proof of concept High-Resolution Computer Tomography (HRCT) to obtain digital datasets of trabecular structures. Having the aim to preserve and exploit the complexity inherent to trabecular structures, the following methods of the theory of Markov processes were investigated: Markov random fields, Markov point processes, a Markov graph based method of conditional entropy as well as Hidden Markov Models. These techniques allowed both to focus on the investigation of simpler, non-complex substructures and at the same time keep structural information of the whole structure by investigating these substructures in parallel. The study confirmed the independency of structural information from bone mineral density. Moreover, both a measure of clustering based on Markov point processes and the Markov graph based conditional entropy improved the discrimination of osteoporotic and healthy trabecular networks compared to standard structural variables. Furthermore, the explanation of failure load was improved beyond bone mineral density by the application of entropy. Additionally, the standardised odds ratios were higher again for the Markov graph based conditional entropy than for the standard variables and the bone mineral density. Summarising, by building a bridge between natural patterns of human cancellous bone to mathematical and stochastic algorithms capable of modeling complex structures this in vitro study proposed a successful way to catch the specifics of these natural patterns and to improve the current structural analysis methods.

Contents

Chapter 1

Introduction

Osteoporosis, a disease of bone, can be viewed from different perspectives: medicine, biomechanics, physics, computer science and more fields of research related. The medical perspective is clearly given by the need of diagnostics and prevention of osteoporosis. The attempt to describe the changes of osteoporosis on bone by utilisation of computer science, specifically statistical motivated pattern recognition is subject of investigation of this work. Thus, after a short introduction to the medical aspects of osteoporosis, an introduction to characterisations of natural structures and the relationship between osteoporosis and structural descriptions is given. Additionally, the basic idea of the statistical technique of Markov processes which are central to this work is given informally. A formal introduction to the Markov theory can be found in section 2.4.

1.1   Osteoporosis: a medical perspective

Osteoporosis is responsible for more than 1.5 million fractures per year in the United States including vertebral and non-vertebral fractures of the hip and wrist [1]. In Germany between four an six million people suffer from osteoporosis; this skeletal disease and its aftereffects are one of the most frequent reasons for medical consultations [2].

Approximately 30% of postmenopausal white women in the United States have osteoporosis, and 16% show osteoporotic characteristics at the lumbar spine in particular [3]. The strength of the spinal trabecular bone declines by a factor of 4-5 from the age of 20 to 80[4]. The lifetime incidence of hip fracture for a person at age 50 is 17 to 22.7 percent in women and 6 to 11 percent in men [5, 6].

Osteoporosis specifically because of resulting fractures has an impact on mortality [7], quality of life [8], and of course increases the costs of the health system [1, 9].
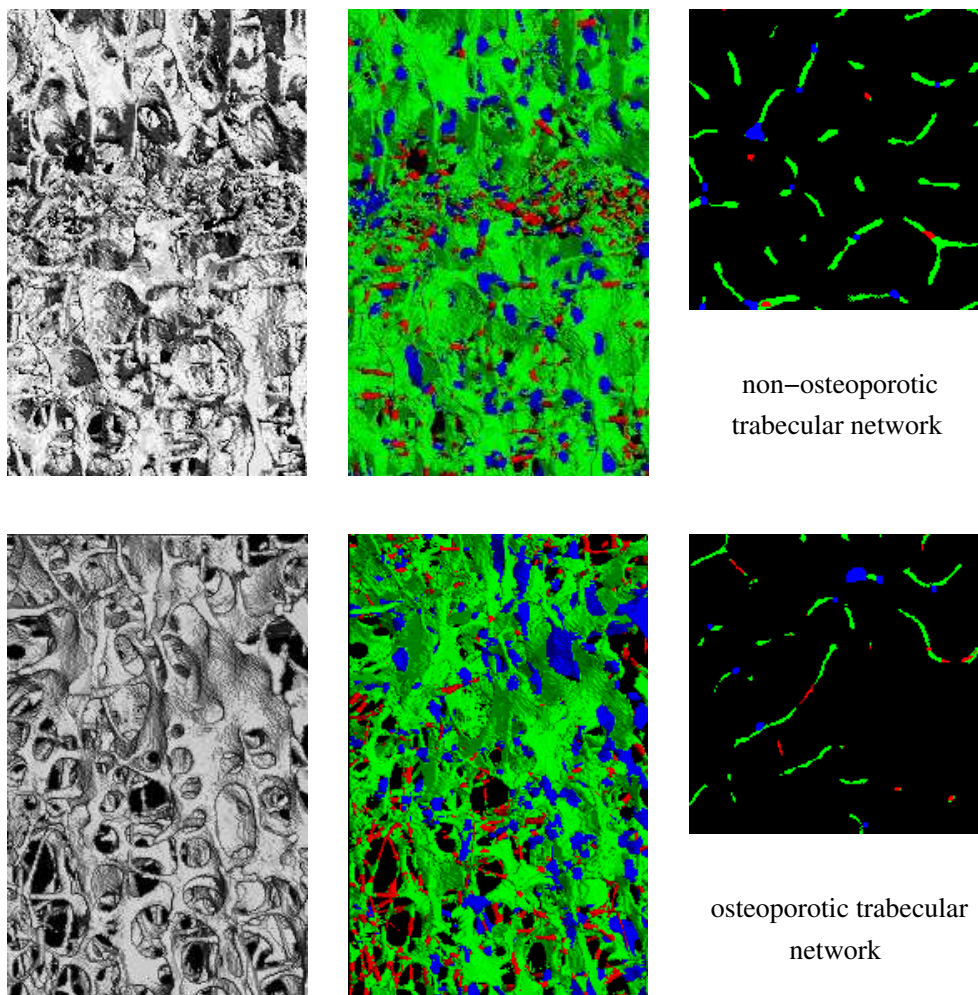
Figure 1.1: <u>Upper row:</u> Biopsy of a healthy vertebra showing a dense trabecular network. <u>Lower row:</u> Biopsy of a vertebra characterised by osteoporotic changes like a sparse, thinned and perforated trabecular network, lowered bone volume (per total volume) and a higher portion of rod like trabeculae (red bone connections). <u>Left column:</u> A grey value rendering of the biopsies obtained from a human female vertebra reconstructed with a Micro-CT with a high resolution of $(25\mu m)^3$ voxel size. <u>Middle column:</u> Topological map colour-coding the local dimension of each part of the network: rods (red), plate-like (green) and junction-like (blue) trabeculae build the network which is subject to change under osteoporosis. <u>Right column:</u> Horizontal slice through the volume showing differences in the thickness of the trabeculae.

Since this disease is preventable when diagnosed early enough or its progress can be decelerated, diagnostic techniques are of major importance. Standard techniques clini-

cally established determine the bone mineral density, while some of the newer techniques investigate the inner structure of the bone: the trabecular network [10] (see figure 1.1).

Since osteoporosis changes not only the bone mass but also the organisation of this mass, the structure, this study investigates standard structural measures applied to osteoporotic and healthy trabecular networks and proposes the application of new techniques borrowed from mathematics, more precisely from the Markov theory.

The National Institutes of Health (NIH) sponsored a Consensus Development Conference, where the following statement about the definition of osteoporosis was given [11]:

> Osteoporosis is defined as a skeletal disorder characterised by compromised bone strength predisposing to an increased risk of fracture. Bone strength reflects the integration of two main features: bone density and bone quality. Bone density is expressed as grams of mineral per area or volume and in any given individual is determined by peak bone mass and amount of bone loss. Bone quality refers to architecture, turnover, damage accumulation (e.g., micro-fractures) and mineralisation.

According to this definition, two main aspects are important when diagnosing osteoporosis: **Bone density** and **bone quality**. The results from research are in agreement with this definition: the bone fragility of osteoporosis is not fully explained by a deficit in bone mass [12]. In order to diagnose osteoporosis measures of these two aspects have been developed and are still subject to investigation:

Some measures of bone integrity

- Mechanical testing (a biomechanical test method which reaches a failure load and tries to quantify stress/strain curves. Non-destructive methods using loads below the failure load are available, too.)

- Vibration analysis (determination of elasticity)

- Finite Element Modelling (FEM, integrity test by material properties and structure)

- Histomorphometry (gold standard for determining several aspects like two-dimensional structural analysis and degree of mineralisation)

- Quantitative Computed Tomography (determination of bone mineral density, first attempts to extract structural properties in vivo)

- pQCT (high-resolution method for density and/or structural analysis)

- Micro-CT (structural analysis at the level of 10-30μm)

- Radiogrammetry (quantification of bone mineral density)

- Magnetic Resonance Imaging (structural evaluations in vivo)

- Quantitative Ultrasound (mechanical bone properties reflecting material and structural properties)

- etc.

This list, which is not exhaustive, depicts some of the variety of bone measurements. Since bone integrity is determined by its density and quality, some measures combine both aspects to some extend.

This study investigates measures which allow pure structural evaluations based on Micro-CT-generated digital models of the inner bone structure, the trabecular networks.

After discussing measures of bone density in the next section structural evaluations are the objective of the subsequent section 1.1.2.

1.1.1   Bone density

The World Health Organisation defined osteoporosis in terms of bone density: a patient's bone mineral density is referenced to that of a young adult's (30 years) normal value (mean of normal population). This so called T-Score defines the degree of osteoporosis in terms of the number of standard deviations below the reference value mentioned above (see table 1.1).

T-Score	Range
0	normal status
-1	Osteopenia
-2.5	Osteoporosis
Fracture	Osteoporosis

Table 1.1: Definition of osteoporosis according to the WHO

As outlined in the last row of table 1.1, a prevalent vertebral fracture is sufficient to diagnose osteoporosis.

Clinically established measures of bone density are [13]

- Dual Energy X-ray Absorptiometry (DXA)
  The basic principle of DXA is the attenuation of X-rays applied in a planar fashion. The attenuation is caused by soft tissue and bone mineral in the hard tissue. Low dose X-rays of two different energies are used to distinguish between bone and soft tissue, giving a very accurate measurement of bone density.

- QCT (Quantitative Computer Tomography)
  While DXA is a planar measure, QCT combines the capabilities of the three-dimensional reconstruction of the object investigated with the principle of attenuation. Since for Quantitative Computer Tomographies a calibration phantom is used, the bone mineral density is determined directly from the phantom and the grey values measured.

The outcome of bone densitometry measurements are always integrated scalar values, although bone is a complex organised structure.

1.1.2 Bone quality

According to the National Osteoporosis Foundation bone quality is covering the architecture, the bone turnover, the damage accumulation (e.g., micro-fractures) and the mineralisation of bone.

The architecture can be viewed as the organisation of bone mass, i.e. the structural design of a trabecular network. This architecture is steadily modified in terms of breaking down and building up parts of the bone, i.e. by the bone turnover. In a healthy system, this process of breaking down and building up bone by cells called osteoclasts and osteoblasts is a nearly perfectly coupled system, with one phase stimulating the other. Under Osteoporosis (or osteopenia, which is a pre-stage of osteoporosis) these two processes become out of sync, the breakdown of bone eventually overtakes the build up.

While bone and thus trabecular networks are exposed to both physiological and non-physiological forces, small damages like single cracked trabeculae may occur while the overall architecture still remains functional. These micro-cracks [14] may be repaired or add up cumulatively while compromising bone strength up to a state where the overall structure may be vulnerable.

The mineralisation of bone is an aspect of bone quality which deals with the amount of calcium and phosphor crystals embedded in the collagen structure, while the type and quality of collagen again may differ and thus impacts the quality of bone [15].

Bone quality in general is an issue of bone integrity. That is the ability of bone to withstand those loads which defined its Gestalt. Unusual loads, i.e. loads which the bone

is not trained to withstand may lead to fractures. These fractures can be detected by a clinically established method to diagnose osteoporotic fractures and thus osteoporosis itself: the application of semiquantitative and quantitative morphometric assessment which allows to assess prevalent and/or incident vertebral fractures [16].

The focus of this study is on another aspect of bone quality: its bone structure and its measures. Imaging techniques applied to the assessment of trabecular bone structure include conventional radiography, magnification radiography, high-resolution CT (HRCT) and high-resolution MR imaging (HRMRI). The best results were obtained using high-resolution tomographic techniques [10].

Most of the studies evaluating structure analysis show that structural parameters[1] and bone mineral density both predict bone strength and osteoporotic fractures, and that combining both techniques yields the best results in the diagnosis of osteoporosis [10].

In consequence, a new structural measure (also called *structural variable*) has to be proven to represent information independent of bone mineral density. Statistically, tests have to be performed which are adjusted by bone mineral density to assess the discriminative power of the structural variables investigated.

Subsequently, bone is introduced as a structural object, which is subject to change under osteoporosis.

1.1.3   Bone as a structure

The macroscopic structure of bone can be divided into the corticalis, a thin compact osseus surface and the spongious inner part, which is surrounded by the corticalis.

Trabecular bone, also called cancellous bone or spongiosa, consists of delicate bars and sheets of bone, the trabeculae, which branch and intersect to form a sponge-like network. It is found at the end of long bones, in vertebrae and in flat bones like the pelvis.

This network built of osseus rods, plates and junctions is called trabecular network. As depicted in figure 1.1 and described in the next section, this structure is subject to change under osteoporosis. The subject of this work is to define a quantitative, comprehensive measure of the complex, interactive elements of the trabecular network.

---

[1]The scientific community often uses the term structural *parameter* to describe a measurement of structural characteristics. However, since formally a parameter specifies a system in terms of adjusting it by selecting a certain value for that parameter, the correct term is *variable*, since a measurement obtains some quantified characteristics stored in a variable instead of adjusting a parameter. Although in this work the identifier structural variable is used, the user should keep in mind that most authors speak about structural parameters.

1.1.4 Osteoporotic changes of trabecular networks

Investigations of changes of the trabecular network are done longitudinal in animal studies [17] as well as cross-sectional in human cadaver or in in-vivo biopsy studies [12].

Much of the cancellous bone deficit found in post-menopausal women with established osteoporosis can be attributed to loss of entire trabecular elements rather than to generalised thinning of trabeculae [12].

Under ovariectomy, for example, which causes a menopause with decrease of oestrogen and thus induces osteoporosis, the bone volume per total volume (BV/TV) decreases (together with the bone mineral density), the separation of trabeculae increases (Tb.Sp), and the number of trabeculae decreases (Tb.N). Additionally, the more plate like trabeculae of a healthy trabecular network perforate and migrate to rod like trabeculae as measured by the Structure Model Index (SMI) [18].

Osteoporotic changes may go hand in hand with age related changes: it is known [4] that with age

- There is a loss of connectivity because of osteoclastic perforations of horizontal struts

- There is an increase in anisotropy - again due to a loss of horizontal struts

- The changes in the network can lead to the slenderness ratio between vertical and horizontal struts reaching a certain magnitude and thereby inducing buckling under compression.

- Micro-damage and micro-fractures will occur - mainly in these very loaded vertical struts. Micro-fractures will be repaired by micro-callus formation, and these calluses will later be removed by the remodelling process.

- Bone material quality will slightly change, leading to a decrease in collagen content and a relative increase in the degree of mineralisation.

Structural changes are the subject of investigation of this thesis. While numerous possibilities exist to quantify structural aspects (see next chapter), a key questions may be not only to define a set of measures which are orthogonal in terms of minimal redundancy. A key question may be the informational content a structural measure carries expressed in the ability to recreate a similar structure based on the structural variable itself.

These and further structural aspects are discussed in the next chapter.

1.2   Osteoporosis: a perspective of computer science

Structural variables, often called structural parameters in the scientific literature, have been the subject of investigation for years now and are measured with many modalities like synchrotron Micro-Computer Tomography (Micro-CT) [19], High-Resolution CT (HRCT) [10, 20, 21, 22], Micro-Magnet Resonance Tomography (Micro-MR) [23], and High-Resolution-MR [24, 25].

There are many different fields of structural descriptions (see figure 1.2) which partly overlap, and which partly provide orthogonal information to each other. Some possibilities to characterise a structure concentrate on specifying aspects of Gestalt, distribution, topology, (dis-)order, complexity, texture and fractal properties. Although a comprehensive comparison of multiple structural variables available in the scientific community would be of interest, the numerous possibilities make it difficult to bring all these approaches together.

On many Micro-CT devices variables describing the Gestalt of trabecular networks are supported by the software provided with the device. In this study, a Micro-CT from Stratec (Pforzheim, Germany) was used, which was not delivered with software for structural characterisations. Hence, the author of this study created a structural evaluation software which is capable of measuring the established standard variables described in section 2.3. These standard variables [26] serve as the reference structural description against which all methods newly investigated within the context of cancellous bone are compared to.

During the course of this chapter, some general considerations about the standard approaches applied to trabecular networks are discussed which lead to the question whether these established measures provide comprehensive information or if they lack the potential to include the central aspects important for structures exposed to mechanical forces (see section 2.3).

After discussing the standard structural variables, the different theoretical fields utilised in this work are reviewed as far as needed to position the main hypothesis (see section 1.3) in its context. Two basic methods are borrowed from statistics which are utilised in this study: first, the probability theory interprets structures as realisation of a stochastic process. The Markov methods applied to these realisations are bound to the probability theory, too, since the Markov property discussed in section 2.4.1 is a formulation of local probabilities. Since the new techniques introduced are to be compared to established methods, statistics again provides methods for this task. Hence, the second method is the use of variance analysis to compare the discriminative power of the Markov approaches between the groups investigated. Each method provides one or more structural measures, which are random variables in theory and structural variables in practise (see figure 1.3).
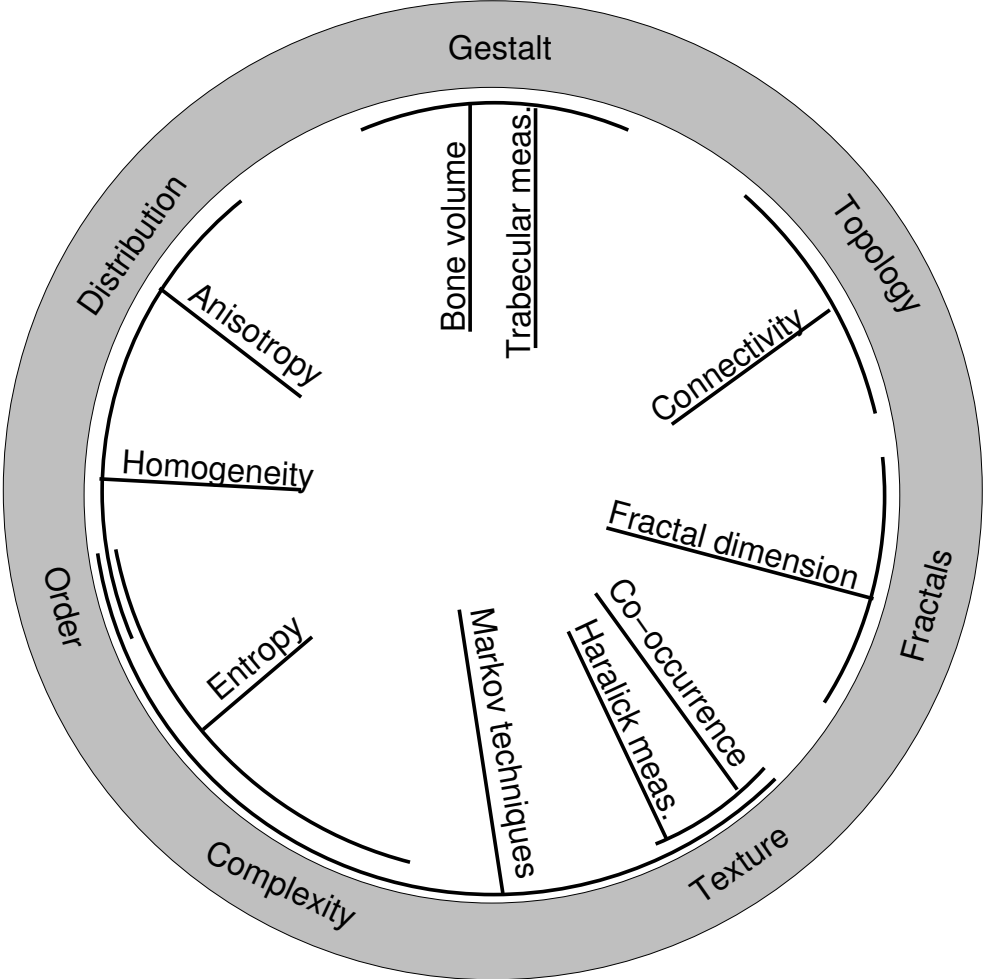
Figure 1.2: A selection of structural characterisations used in the field of structural related research of osteoporosis. The Markov techniques applied to trabecular networks are investigated in this study (including the entropy approach which is related to the Markov property) and compared to the established Gestalt parameters.

Trabecular
Networks

Structural variable

Realisations   Random variable

Markov point
processes

Markov Random
Fields

Markov Graphs

Markov Models —————————————— Stochastic processes   Variance analysis

Probability theory

Statistics

Thesis
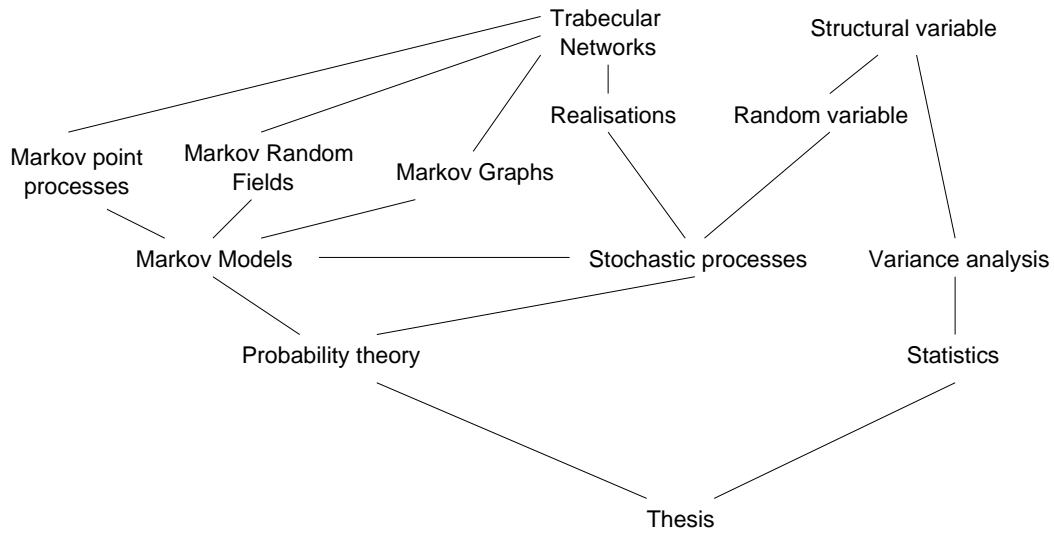
Figure 1.3: Statistics serves for both the incorporation of new techniques into the field of structural characterisation of stochastic realisations and the statistical evaluation of the ability of these methods to characterise structure. The probability theory is the framework which motivates the interpretation of trabecular networks as realisations of a stochastic process. Markov techniques allow to model overall probabilities in terms of local characteristics found in trabecular networks. Additionally, quantitative measurements based on Markov properties serve as innovative structural features for the characterisation of trabecular networks. These structural evaluations are called structural variables in the context of trabecular networks and at the same time are random variables of a stochastic process (see section 1.2.3). The discriminative power of the structural variables defined within this work is tested by statistical techniques of the variance analysis. The latter built the second arm of the graph.
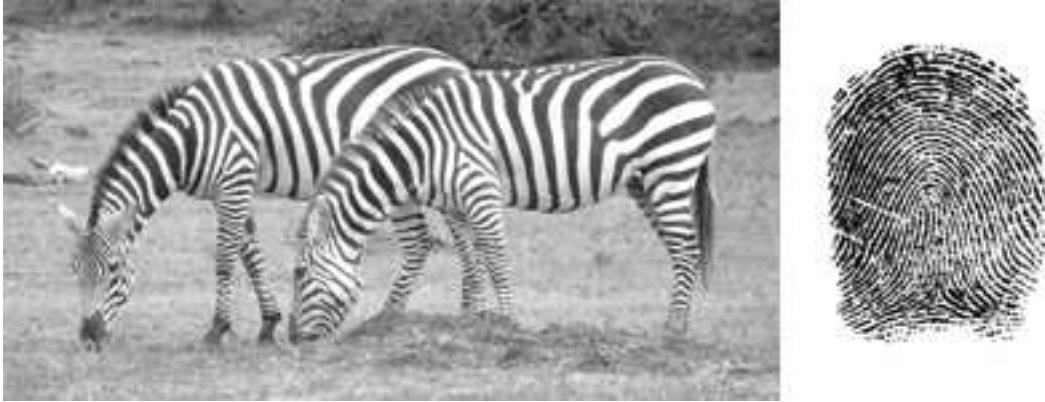
Figure 1.4: Two examples of realisations of natural stochastic processes showing common concepts while being individually different: <u>Left:</u> Striped patterns of zebras. <u>Right:</u> Human fingerprints. Both examples look similar in a global sense but show local differences.

1.2.1 Simultaneous equality and inequality

Investigating the question what is typical of a structure, common concepts or equality is to be formalised. When looking for the individual, on the same time subtle differences allow for differentiation. The concepts of equality (on a coarser level) and inequality (on a finer level) are concurrent as can be found in biology: prominent examples are zebras (see figure 1.4). The typical striped pattern is a common concept shared by all zebras, while each individual shows a different realisation of this pattern. This phenomenon is frequently observable: a group of natural objects shares typical common aspects but differ with respect to local characteristics. Another example is a human fingerprint. Of the millions of fingerprints collected and compared since the onset of maintaining fingerprint files by the FBI in 1924 till the year 1984, no two fingerprints were considered to be identical [27]. The palm print is one of the most reliable physiological characteristics that distinguishes individuals[28]. The individuality of human beings determined by genetics (and other factors) is in line with the individuality of the genetically determined fingerprints [29] although sharing concepts as mostly parallel lines and junctions of lines, etc. exist. The reason for the omnipresent differences between fingerprints or, more general, skin ridges is the number of variables modifying the structure during its development [30].

Trabecular networks as given in figure 1.1 which are in the centre of investigation in this study, are natural examples of similar but different structures for which structural measures are needed to describe them.

1.2.2   Information preservation

If an integral sums up the area under a curve, the shape of the area is not preserved under the operation of the integral. The loss of information of a measure may lower its power when conclusions are based on it. An indication of the amount of information preserved by a certain measure can be extracted from the variability of the set of structures which leads to the same result when applied to this measure. The problem of the loss of basic structural properties under the representation of integrative measures and the idea of structural regeneration of measures is discussed within the next two sections:

1.2.2.1   Loss of information by integration

Since the standard measures introduced in the previous section are integrative scores averaging quantifications of characteristics over the whole volume of interest, the question may arise, whether non-integrative aspects of structures are modelled sufficiently. To clarify this point, see figure 1.5. In this visualisation the scenario is given that two structures consisting of vertical trabeculae like struts are exposed to a load in vertical direction. Although the integrative measures bone volume to total volume (BV/TV) and trabecular number ($Tb.N$) for the above, regular structure and the bottom, irregular structure respond with the same value when horizontal test lines are provided, the load applied to the trabeculae may differ considerably. Although this is a simplified model of structures neglecting several factors like horizontal trabeculae and non-horizontal test lines it may exemplify that the integration of characteristics over a whole volume is not sufficient to model the difference of these two structures.

A hypothesis of this work is that the main deficit of the integrative structural approaches defined in section 2.3 above is the lack of modelling local relationships, or, in other words, the informational content of a measure increases and leads to a better discrimination between the structures if local relationships are included into the measure. For example, the increased load of the middle trabeculae of the bottom structure in figure 1.5 exists as locally there are no neighbouring supportive trabeculae to the middle one. A measure which would have incorporated a distance between the trabeculae would successfully discriminate these two simple structures.

1.2.2.2   Information specification: Families of structures

As discussed, a loss of information when applying an integrative measure to a structure may have the consequence, that the structure is not specified well by the measure, i.e. that different structured patterns belong to the same measurement result. An ideal measure would preserve all information necessary to reconstruct the typical characteristics from
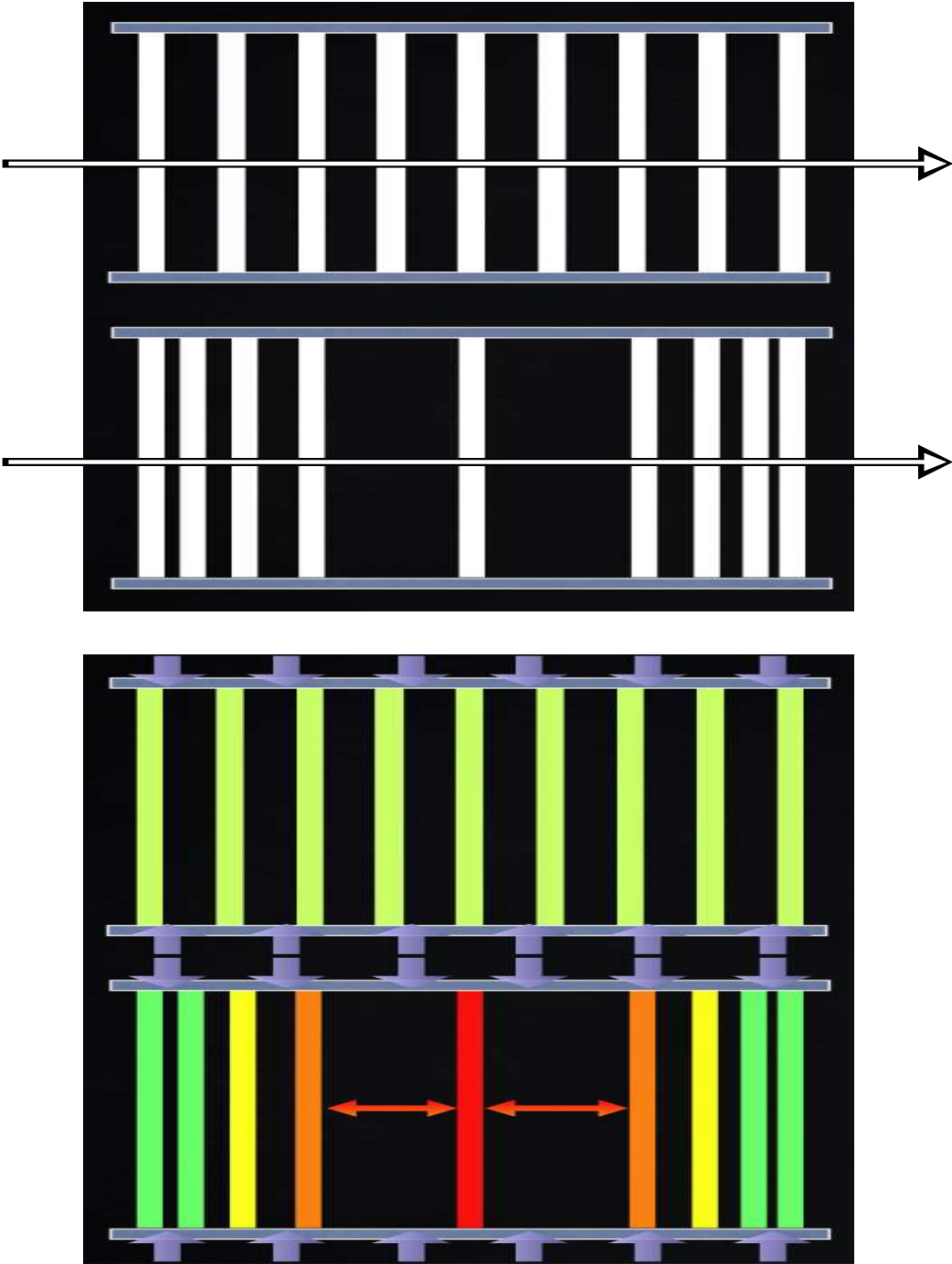
Figure 1.5: Top: structures (white), evaluated in one direction (arrow) with the same number of phase changes (black ↦ white, white ↦ black) and the same fraction of structure (white) versus background (black): a) regular pattern, b) irregular pattern. The standard structural variables principally do not take into account the differences of the regular and the irregular pattern. Thus, the regular and the irregular pattern result in the same structural values if evaluated one dimensional. Bottom: qualitative visualisation of an estimated load applied from above (and below) to the regular and irregular structure. The distance a structure has with regard to its nearest neighbour is positively correlated with the load it has to withstand (highest load on middle, red column).

its measure. In this case, the structure is described by a measurement exactly. But a structural characterisation of a complex structure is a complex problem, since the space of structural measures is high-dimensional. In practise, for complex patterns structural characterisations may not preserve all information contained in a structure. Nevertheless, when a high amount of information is preserved, a reconstructed structure s_1 should show similar structural characteristics to a second structure s_2 reconstructed on the same measurement result with regard to some similarity measure.

Since it may be impossible to describe complex structural characteristics completely, there is no inverse mapping from a result of a structural measurement to a unique structure; repeated inverse mappings will result in similar, but in detail different structural samples: A family of structures.

Summarising, a structural measurement describing the typical structural characteristics will map only similar structures to almost the same result and generate only similar structures from a specific measurement value by an appropriate method. In other words, an optimal structural measure could be described as being robust.

The concept described above supports both the partition of trabecular networks into two groups of in each case similarly looking healthy and osteoporotic structures and the need to minimise overlaps of structural measures (see figure 1.7).

1.2.3   Structures as realisations of stochastic processes

The interpretation of natural structures as realisations of stochastic processes (and thus members of similarly looking structure families) is exemplified in terms of biological instances of structures first. As discussed in the following section this leads to a mathematical theory which may be appropriate to model similarities expressed in terms of probability.

A natural structure $\omega \in \Omega$ thus may be interpreted as realisation of a stochastical process X [31], i.e. it is drawn from the probability distribution of X. If structural characteristics are of interest, a certain measure is evaluated over the set of realisations. Each of these structural measurements is indexed by a set I, thus for a sample ω of the sample space Ω we are interested in certain features $t \in I$ (or derived features like structural parameters $D(t), t \in I$) when investigating the stochastic process:

$$X(\omega, t) : \Omega \times I \mapsto \mathbb{R} \tag{1.1}$$

Thus, $x(\omega, \cdot)$ as a realisation of the stochastic process X is the object under investigation with regard to structural characteristics $t \in I$. Here, I shares the dimension of the
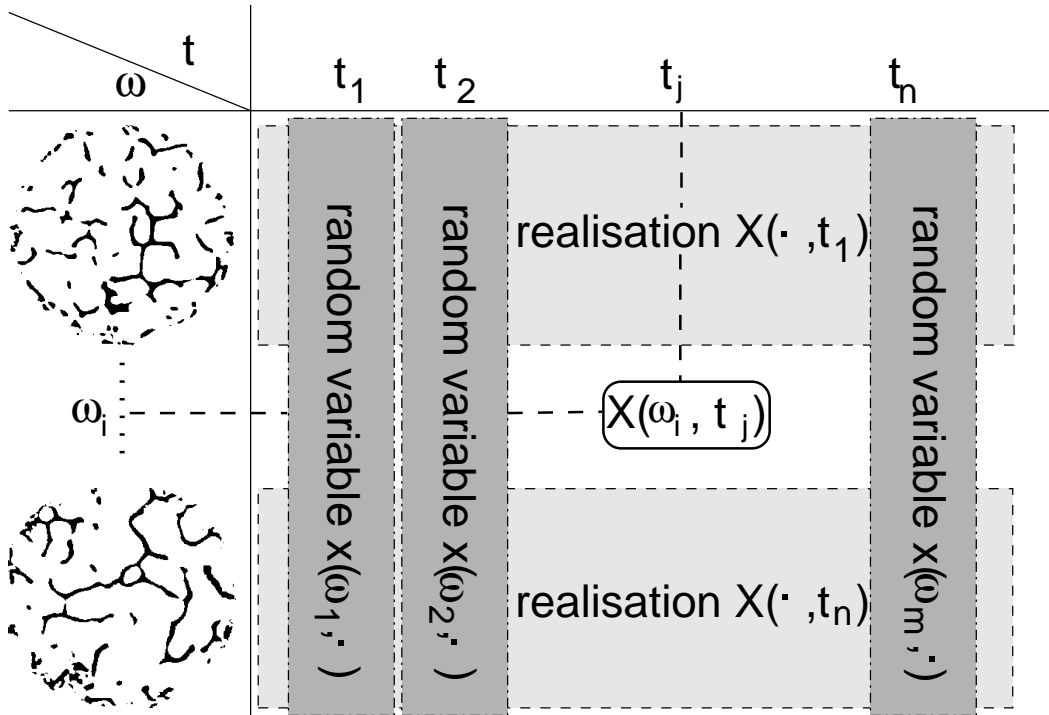
Figure 1.6: A stochastic process given by a set of natural structures (here: slices of trabecular bone networks) organised in rows, and a set of structural variables, stored in columns, allowing to investigate the property t_j (or computed/derived features of t_j: $D(t_j)$) of the realisation ω_i: $X(\omega_i, t_j)$

structure. Thus, for two-dimensional structures, I is two-dimensional, too, like $I = \mathbb{R}^2$. Additionally, $X(\cdot, t)$ represents a random variable, i.e. a structural variable of X evaluated over the set of realisations ω_i (see figure 1.6).

The variability of a structural variable may lead to the situation that a group of subjects which is rated as pathologic is not separated well from another group which was classified as healthy (see figure 1.7) with regard to a certain structural characteristic. Thus, for some subjects a structural measurement may result in a value which is shared by the pathologic and by the healthy cluster. To analyse whether there is a difference between these two groups, the variance of the groups is investigated.

Thus, from a statistical point of view, the amount of variance is to be determined which explains the difference of a structural variable found in both groups of subjects.
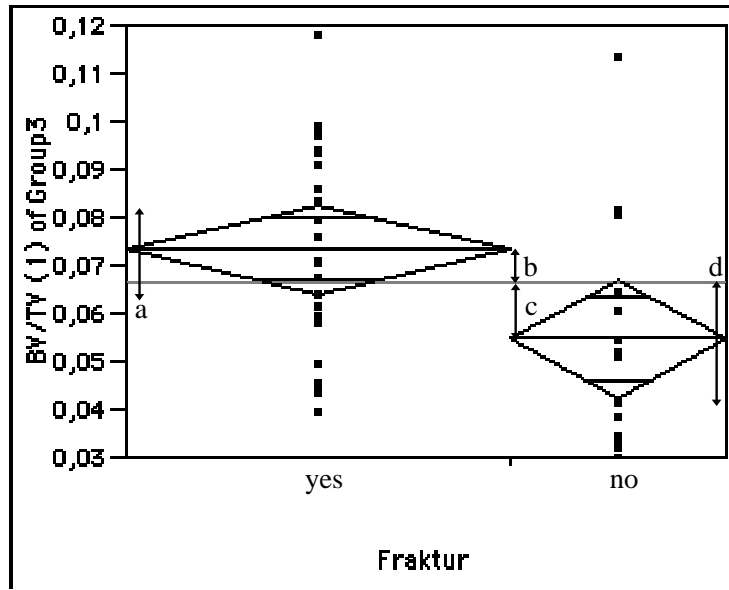
Figure 1.7: Two clusters in a one dimensional feature space of Bone Volume per Total Volume (BV/TV), i.e. the feature BV/TV derived from $X(\cdot, t_{ij})$ investigated is the sum of voxels t_{ij} classified as bone by thresholding $(S \mapsto \{0, 1\}, S(t) = 1 \quad \text{iff} \quad t > threshold)$ divided by all voxels evaluated. Variances a and d are not explained by the structural variable BV/TV, while variances b and c are explained by BV/TV

1.2.4   The expected benefit of Markov-based structural characterisations

The application of Markov techniques to the field of structural characterisations of trabecular networks has two main advantages:

- Breakdown of complexity: A trabecular network is composed by numerous connections of different topological elements. Thus, multiple interactions have to be modelled to characterise a trabecular network comprehensively instead of measuring global characteristics.

- Preservation of structural information: By modelling local interactions, Markov methods allow to regenerate realisations similar to the original structure and hence carry structural information not captured by simple standard structural measures.

A structure may show a certain degree of complexity which makes it difficult to describe this structure in a comprehensive way. One possibility to find a description which tries to catch as most features as possible is to combine simple characterisations to a vector of observations assigned to a structure. This spans a multidimensional space of characterisations, while the redundancy between the single dimensions is needed to be investigated. Although an orthogonal subspace cannot be defined since the concept of linear combinations of measures known from vector spaces is difficult to apply to the heterogeneous set of structural measures, one is interested in defining a comprehensive set of structural characterisations while on the same time lowering the redundancy and thus the cardinality of this set.

Instead of collecting different measures of structure to increase the comprehensiveness of the combined measure, Markov techniques handle complexity by not assessing a whole structure at once, but characterising local parts of a structure in parallel. Thus, a Markov technique investigates a limited view of the structure multiple times and combines the results. Since structures often can be described as repeated and modified features over a space, the idea of looking at local features at all positions or subsets of positions at the same time reduces the complexity of the measure to the complexity of the local feature. The parallelism of this approach ensures to capture the information typical of the structure investigated although the spatial range of the measure was decreased.

Modelling local interactions allows to reconstruct families of structures based on a Markov-based characterisation using a Metropolis-Hastings algorithm [32], for example. The amount of structural information captured is appropriate to describe the structure in terms of typical structural concepts shared by the family of similar structures while at the same time allowing for small differences of the structures.
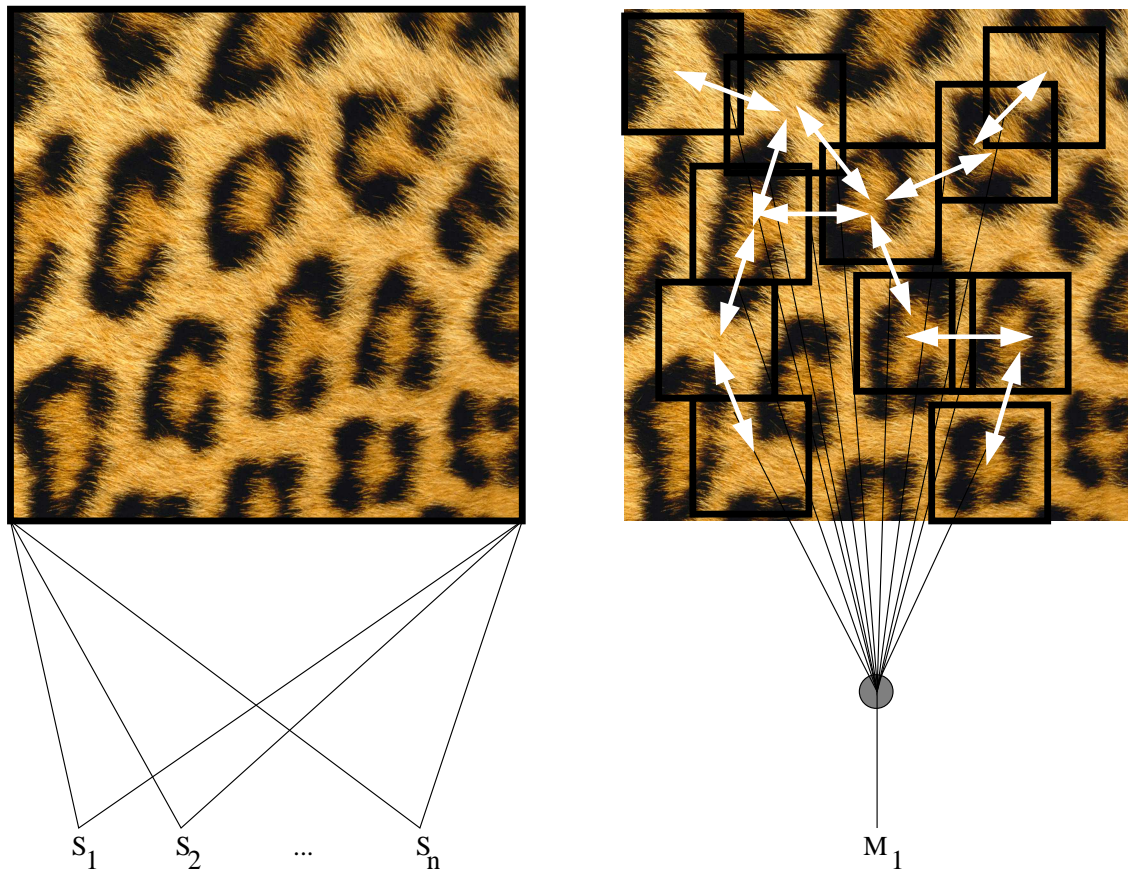
Figure 1.8: <u>Left:</u> The whole structure is evaluated with respect to a certain measure S_1. To increase the comprehensiveness of the measure, further measures are performed and the results are collected to a descriptive vector $< S_1, \ldots, S_n >$. <u>Right:</u> The scale of the Markov-based investigation is smaller compared to the conventional structural evaluation presented on the left side. Due to the local range the measure itself can be evaluated at a certain position and in parallel at neighboured locations. The relationship between a Markov measure at a certain position and at its neighbour positions is central to the approach. For example, a measure detecting a black area inside usually is neighboured to a measure which contains a non-black region with a higher probability for a certain distance. By specifying the spatial relationship between black and non-black areas a powerful description for the pattern can be given which is not possible with a measure integrating over a whole structure as given on the left side. Of course, a combination of different Markov measures is possible, too.

Hence, Markov methods are expected to capture the typical properties of the stochastic realisations given by trabecular networks of the two families of *healthy* and *osteoporotic* samples.

1.3 Hypothesis

The considerations of this chapter are condensed into the following hypothesis:

- Within the mathematical framework of Markov-based methods certain concepts, specifically Markov point processes, Markov graphs, Hidden Markov Models and the conditional entropy are applicable to the structural characterisation of human trabecular networks. Thus the benefits of Markov theory, that is the breakdown of complexity and the capture of essential structural information can be utilised for the investigation of structural changes of osteoporotic networks.

- With regard to the integrative standard structural measures based on bone mineral density (BMD), bone volume to total volume fraction (BV/TV) and trabecular number ($Tb.N$), the use of Markov based measures leads to

    - a better explanation of the variance between the two groups of osteoporotic and healthy trabecular networks.
    - an improvement of the explanation of the failure load of neighboured vertebrae.

1.4 Presentation of research

Different parts of this research were presented at several scientific congresses on an ongoing basis:

Year	Conference
2000	High Resolution imaging by a new micro-CT for the assessment of novel shape-based structural and geometrical parameters at periheral sites. W Timm,R Barkmann, R Scheffczyk, E-M Lochmüller,C Glaser, M Heller, C-C Glüer, 14th International Bone Densitometry Workshop, Warnemünde, in Osteoporosis International, Vol 11, Supplement 3, pp. s9-s10
2000	3D Assessment of Bone Structure of Whole Vertebra Bodies by a New Micro-CT. W Timm, R Barkmann, B Stampa, E M Lochmueller, M Heller, C-C Glueer, Journal of Bone and Mineral Research, Vol. 15, Suppl. 1, p. S522, ASBMR 22nd Annual Meeting
2000	*Young Investigators Award*, sponsored by Synarc, Project title: Classification of Structures by Markov Random Fields: Application to Osteoporotic Bone, 14th International Bone Densitometry Workshop, Warnemünde
2001	Frakturdiskriminierung durch neu entwickelte geometrische und konturbasierte Strukturparameter und ein neues Mikro-CT an Phalangen in vitro. W Timm, R Barkmann, R Scheffczyk, A Mohr, E-M Lochmüller, C Glaser, M Heller, C-C Glüer, 82. Deutscher Röntgenkongress, Wiesbaden, in RöFo, Band 173, S. s23
2002	Stochastic Modelling of Trabecular Networks. W Timm, C-C Glüer, Proceedings of 15th International Bone Densitometry Workshop, Monterey, CA
2002	Fracture discrimination by structural parameters is superior to bone density: an in vitro study. W. Timm, C. Sieber, F. Eckstein, E-M Lochmüller, M. Heller, C-C Glüer,4th Baltic Bone and Cartilage, Binz, Rügen, in Acta Orthopädica Scandinavica, Vol. 73, Supplementum 304, S. 25
2003	Vergleich der sequentiellen und sprialen hochauflösenden Computertomographie zur Strukturanalyse von trabekulären Knochenstrukturen. W Timm, M Heller, C-C Glüer, 84. Deutscher Röntgenkongress, Wiesbaden, RöFo, Band 175, Supplement 1, S. S262
2003	Umfassende Strukturcharakterisierung trabekulärer Netzwerke durch Stochastische Modellierung zur Frakturdiskriminierung. W Timm, C-C Glüer, M Heller, Osteologie 2003, Göttingen, 2003, Osteologie, Band 12, Supplement 1, p. 38
2004	Degree of order determined by local conditional entropy: a new technique to assess osteoporotic changes of trabecular networks, W Timm, C.-C. Glüer, G. Sommer, Medical Imaging 2004, San Diego, CA, USA, Proceedings of the SPIE, Volume 5370, pp. 1292-1303, (Poster Award)

Chapter 2

Materials and Methods

In this chapter, first the set of study data is described. After discussing the modalities utilised in this study, the generation of the computerised representations of the study population is given. Subsequently, the standard structural variables are given as reference methods, followed by an introduction and discussion of the innovative Markov measures used in this study. These are threefold: Node probabilities as well as measures of entropy are based on Markov graphs, while configuration patterns of trabecular networks are build on Markov point processes. Finally, Hidden Markov Models were introduced to give a method for the detection of structures.

2.1 Data set

The data set investigated in this study is subsequently described in terms of the vertebrae used, the characterisation of the osteoporotic status of the donors and the preparation of the bones.

2.1.1 Study population and study groups

The Anatomical Institute of the Ludwigs-Maximilians-University München provided 209 human vertebra T12 excised in anatomical courses. The aim was to identify two sets of vertebra:

1. An osteoporotic group *FX*

2. A non-osteoporotic group *Non-FX*

Grade	Deformity	Height Reduction
0	no	0
1	mild	$< 20\%$
2	medium	$20\% - 40\%$
3	severe	$> 40\%$

Table 2.1: Grading of severity of fractures based on a spine radiography assessment.

Group	Number	Mean Age	StdDev Age
FX	14	83.29	± 6.24
Non-FX	25	80.68	± 7.19
All	39	81.62	± 6.9

Table 2.2: The groups of vertebra used in this study.

Every vertebra included in the finale measurement suite had to fulfil the following conditions

- The vertebra had to stem from a female donor (in order to exclude sexual differences from the investigation and focus on structural differences).

- For the donor no disease was known for the point of time when the vertebra was excised.

- The vertebra itself was not fractured (although a fracture in the same spine at another vertebra is allowed and leads to an assignment to the fracture group, see table 2.1)

To decide whether a vertebra had to be assigned to one of these groups (or not to fit to any of these groups), an experienced radiologist assessed radiographs taken from the donors and graded each vertebra into one of the following groups: grade 0 (no fracture), grade 1 (mild deformity), grade 2 (medium deformity), grade 3 (severe deformity). Quantitative deformity levels are given in table 2.1.

Thus, the osteoporotic group (also called fracture group) consisted of vertebrae which were themselves non-fractured, but stemmed from a spine which included a fractured vertebra. For a vertebra assigned to the Non-FX group (also called healthy group), all vertebrae of this spine were assessed fracture-free. To clearly separate the fracture from the healthy group, all vertebrae with fracture grade 1 were excluded. The resulting groups are listed in table 2.2.

Finally, a dataset of 14 fractured vertebrae (FX group) and 25 non-fractured vertebrae (Non-FX group) was defined for the investigations of this study.

2.1.2 Preparation of bone specimens

Each vertebra was cut entirely from the spine through the intervertebral discs and stored in a formaldehyde atmosphere. After completion of the first whole vertebra-measurement (see section 2.2.2.1) by the μCT, all vertebrae were frozen by $-18°C$ to increase stability and subsequently a cylindrical biopsy from the centre of the vertebral body was obtained with a diamond saw. The diameter of the biopsies was $8mm$ while the height was determined by the height of the vertebral body.

2.1.3 Overview of study data utilisation

The further study data utilisation during the study can be retrieved from figure 2.1. The data set retrieved with a voxel side length of $156\mu m$ provided a basis for the investigation of node probabilities in chapter 2.4.5.1.1. On the data set obtained with an even higher resolution ($25\mu m$ voxel side length) the approach of local conditional entropy was built in chapter 2.4.5.1.4. For this approach a classification of each voxel into its membership to one, two or three-dimensional trabecular structures was performed, described in section 2.4.5.2.3. A restriction of the same dataset to the set of voxels classified as three-dimensional built the data basis for the point process based measures explored in chapter 2.4.4.4.

2.2 Measurement procedures

During the last years techniques became available capable of obtaining vertebral measurements with a resolution showing details of the trabecular network: High Resolution Computer Tomography provides high resolution measurements both in vitro and in vivo. However, in vitro techniques work with small objects and are conceptional capable of producing a better quality compared to in vivo techniques. Both techniques were used in this study and are introduced in the following two sections.

2.2.1 High Resolution Computer Tomography (HRCT)

Since during the last years modern Computer Tomographs were installed into the clinical routine which are capable of measuring in vivo voxel sizes around $150\mu m$ [33], the resolution obtained in vivo overlaps the range of thicknesses found for trabecular networks. Although voxel sizes of below $(150\mu m)^3$ are obtainable since the field of view of a reconstruction can be adjusted to define smaller voxels, the possibility to reconstruct small voxels does not mean that the corresponding optical resolution is actually reached.
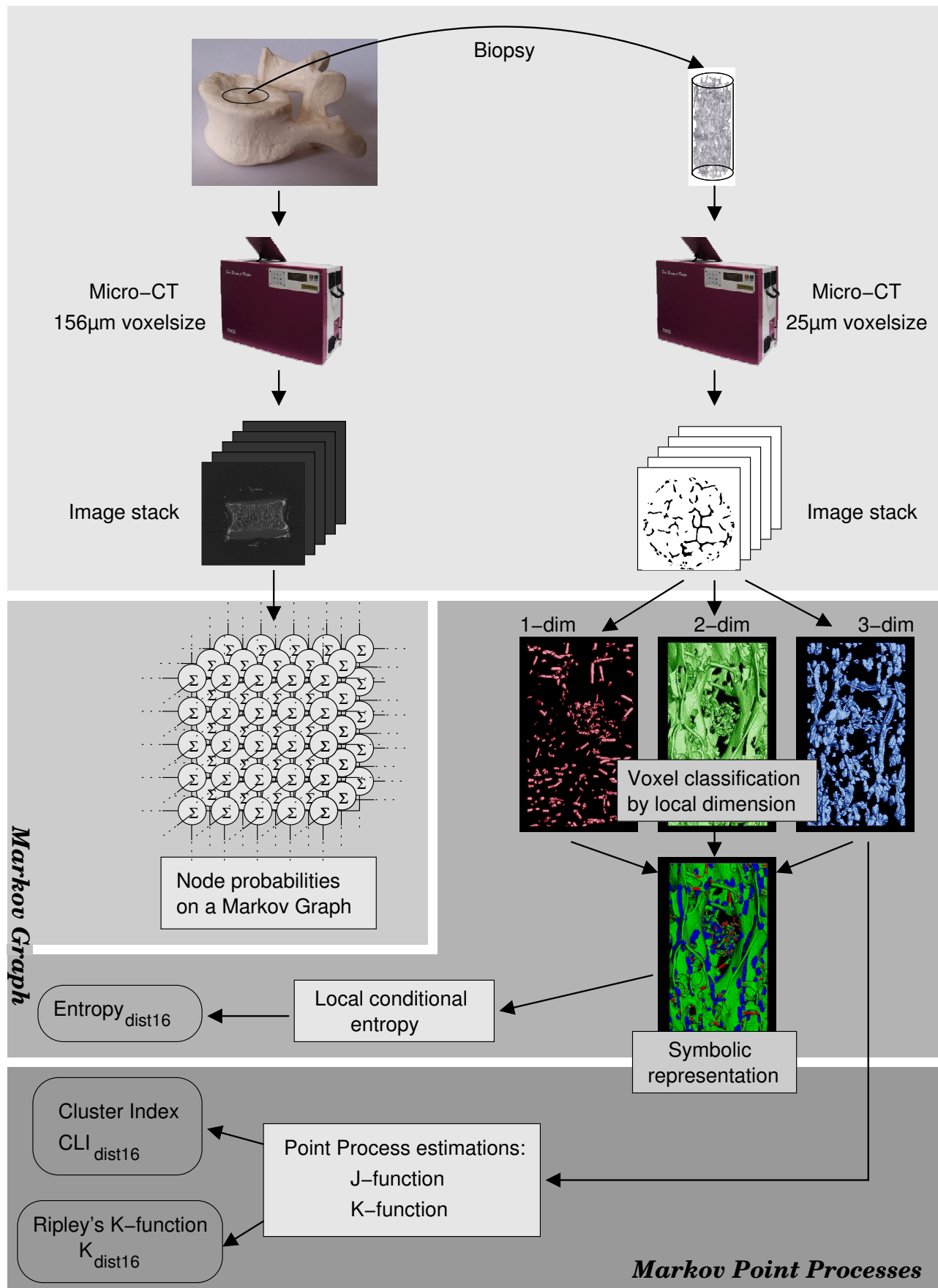
Figure 2.1: Flow of data and investigation during the study

The High Resolution Computer Tomography (HRCT) protocol applied in vivo to a female's patient vertebra T12 during a different study resulted in a dataset depicted in figure 2.2. The parameters used of the protocol performed on a Sensation 16 (Siemens, Erlangen, Germany) were: 120kVp, 360mAs, slice thickness of 0.3mm, voxel size of $150\mu m \times 150\mu m \times 300\mu m$, and a reconstruction kernel B80s using a helical scan.

Without quantification figure 2.2 depicts the main task to be solved when investigating in vivo HRCT measurements: the differentiation of peaks induced by noise from peaks induced by (trabecular) bone. Markov techniques utilising stochastic principles may be adequate to discriminate bone structures to be evaluated from noise structures to be neglected as introduced in section 2.4.6.1 and investigated in section 2.4.6.3 as proof of concept. A further possibility to handle noise as a random point process is discussed in the outlook (section 5.1.1.2).

2.2.2 Micro-CT measurements

The facility of the micro-CT to measure objects up to $8cm$ diameter was exploited by measuring the vertebra twice: first, a high resolution reconstruction was obtained to generate a dataset depicting the trabecular network at a coarser scale. Second, a very high resolution scan with biopsies taken from the vertebrae allowed to exhibit the trabecular network at the highest level of detail available with this Micro-CT device.

2.2.2.1 Reconstructions: High- and very high resolution

The Micro-CT device *FanBeam µ-Scope* (Stratec, Pforzheim, Germany, see figure 2.3) were used to generate the digital datasets of the study samples. This is a desktop Computer Tomograph capable of measuring small specimens with diameters of up to $8cm$, allowing to obtain two scales of resolution from the study sample set:

- A low resolution scan of the *whole* vertebra with a voxel size of $156\mu m$. The scan of each vertebra resulted in a dataset of $512 \times 512 \times 400$ voxels.

- A high resolution scan of a biopsy taken from the vertebra with a voxel size of $25\mu m$. From each vertebra a central biopsy of 8mm diameter and 10 mm length was obtained. Scanning each biopsy resulted in a dataset of 512 x 512 x 1000 isotropic voxels of 25 micrometres side length.

These measurements assigned to each voxel a continuous representation of the corresponding density of the biopsy. For subsequent investigations the proprietary 4 byte float format
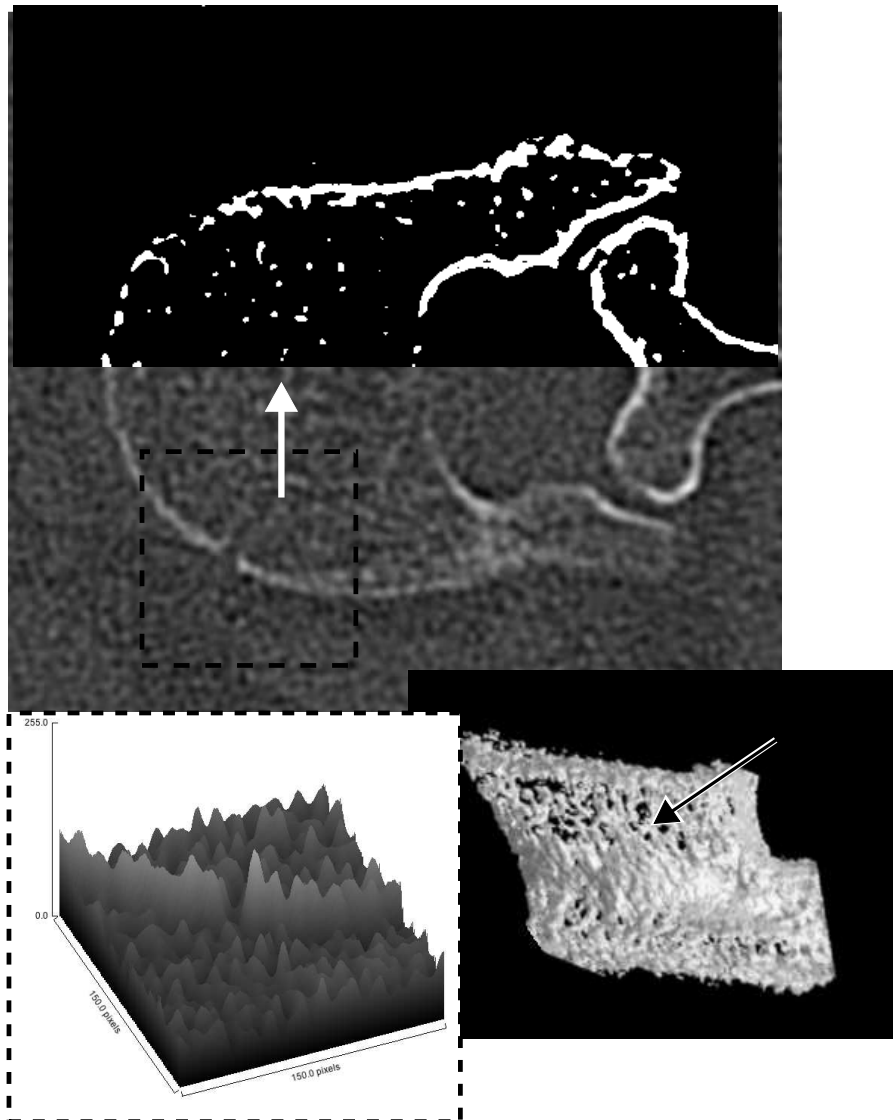
Figure 2.2: HRCT reconstruction of a human vertebra T12. Upper half: binarisation of original dataset visualised in the lower half of the larger figure. Bottom left: surface plot of the rectangular area of the grey value reconstruction. Bottom right: three-dimensional rendering of the half vertebra shown above (processes virtually cut off). The corresponding viewing angles are depicted by the arrows.

of the Micro-CT device was transformed into a grey value range of 256 shades. Since the analogue to digital processing of the device used 10 bits only, a 8 bit representation were

Figure 2.3: Micro-CT FanBeam μ-Scope used in the study.

estimated as appropriate to represent binary structures like bone.

All measurements were performed with a voltage of $40kV$, a current of $200mA$, an exposure period of 0.2 seconds per profile obtained, and 250 profiles per slice. A beam hardening correction was active.

2.2.2.2 Voxel sizes in HRCT and Micro-CT

Although the voxel sizes for HRCT ($150\mu m$) and Micro-CT ($156\mu m$) are comparable, the corresponding resolution is showing a certain difference due to technical reasons: First, the HRCT protocol was obtained in vivo, which means that the vertebra of interest was surrounded by soft tissue absorbing x-rays and modifying the x-ray spectrum. During the in vitro measurements of the Micro-CT the vertebrae investigated were excised and free from most of their soft tissue. Second, a clinical scanner typically scans in the time frame of a few seconds to at maximum a minute or two, while a Micro-CT device scans the same object in vitro in several hours. Hence, the nominal values of voxel sizes correspond to different corresponding resolutions.

2.2.3 Preprocessing: binarisation

A binarised representation of the trabecular architecture is used for the further investigations. While the binarisation of the Micro-CT representations of the trabecular networks is performed using simple thresholding, the Hidden-Markov approach presented in chapter 2.4.6 for HRCT measurements is following a different approach based on prior knowledge
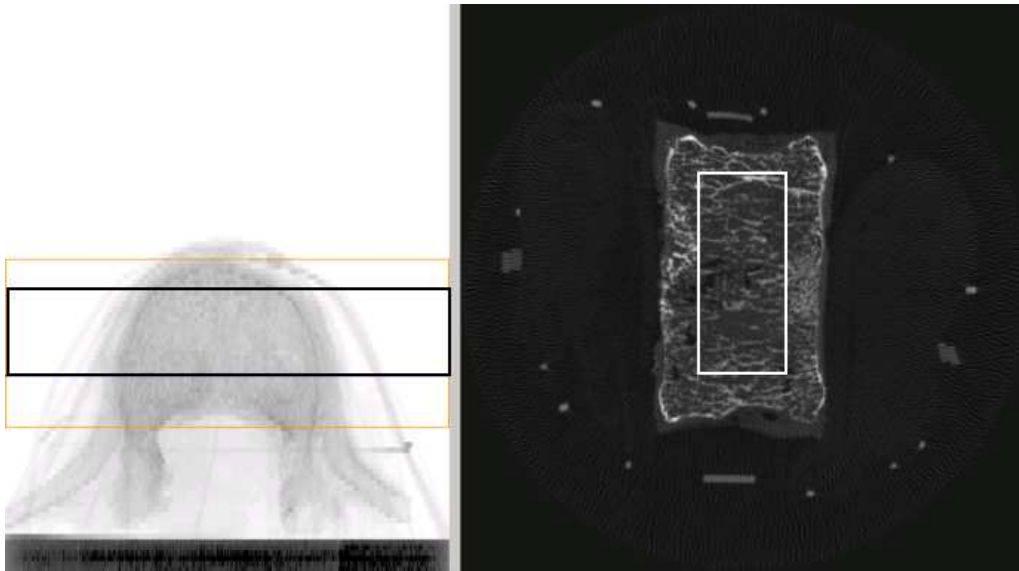
Figure 2.4: Left: Scout View of a vertebra measured in the FanBeam μ-Scope. The orange box marks the measurement range, the black box indicates where slices were evaluated. Right: Horizontal slice through the whole vertebra with a voxel size of $(156\mu m)^3$ $((156\mu m)^2$ in plane and a slice distance of $156\mu m$). The white box depicts the area delimiting the evaluation within the plane by excluding any cortical or abnormal parts of the vertebra. The rubber bands fixating the vertebra on its base plate in the micro-CT are visible around the vertebra.
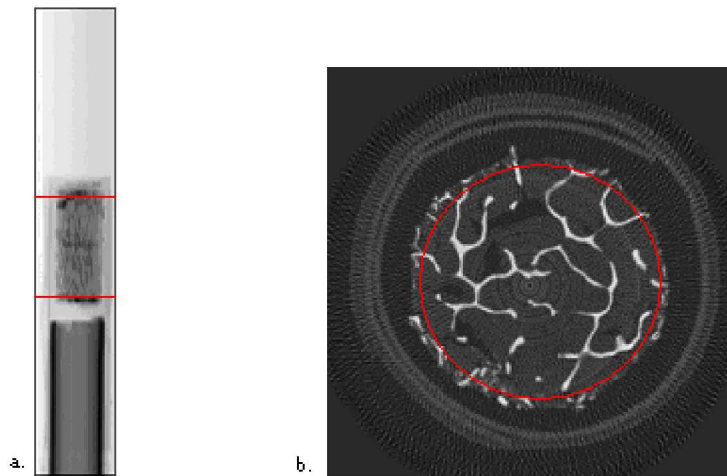
Figure 2.5: Left: Scout View of the biopsy placed on plastic tube. Right: Slice through the biopsy. Red markers: Limiting the cylinder which was evaluated.

combined statistically with the grey values of the measurement to judge the status of a voxel under investigation of being bone or not bone. Hence, in this subsection, the thresholding binarisation is presented only.

Although the coarser digital representation obtained with $156\mu m$ was assumed to show only the bigger part of the trabeculae available in a human trabecular network while being impacted by partial volume effects, the contrast was observed as sufficient to perform a simple thresholding by selection of a threshold of 120 (the grey value range first was transformed to a range of $0, \ldots, 255$). This threshold was chosen by comparing the binarised structures with the original measurements while changing the threshold and optimising the visual equality between them (see figures 2.4 to 2.6). For the measurement obtained with $25\mu m$ the same threshold were found to be a valid.

All selections of the volumes of interest as well as the binarisation were performed with the in-house developed software *Structural Insight* written by the author of this study during his employment at the Medical Physics Research Group at the Department of Diagnostic Radiology of the University Hospital Schleswig-Holstein.
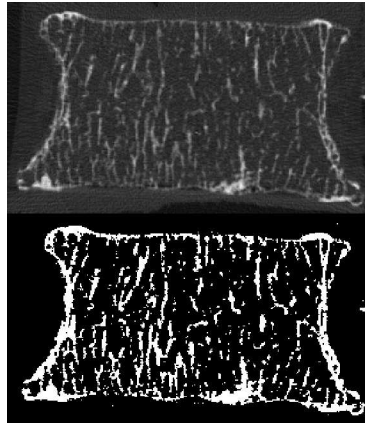
Figure 2.6: Top: Slice through a vertebra. Bottom: Binarisation.
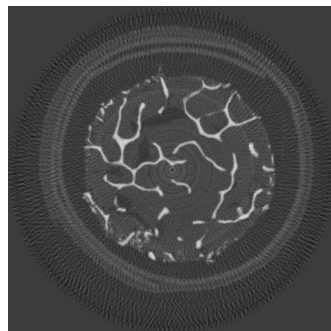
Figure 2.7: Top: Slice through the biopsy of a vertebra. Bottom: Binarisation.
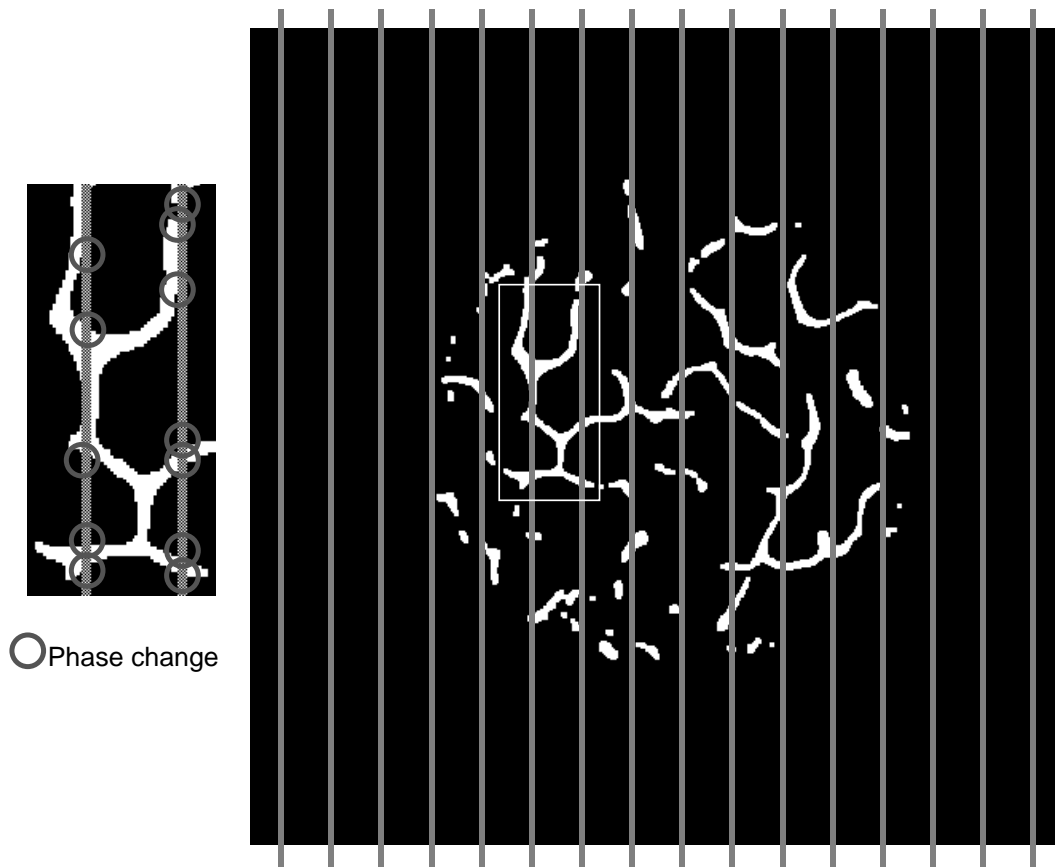
Figure 2.8: Test lines (grey) for which the phase changes (see circles in the left image) between marrow and bone as well as bone and marrow are counted are laid over the binarised structure (black/white). Afterwards, the parallel test lines are rotated (altogether a few hundred rotations are taken into account) and the phase changes are computed again. After repeating the rotation - evaluation sequence, the overall phase changes are divided by the overall length of all test lines. This gives a basic parameter which together with the bone volume fraction provides access to all standard measurements.

2.3 Standard structural variables for trabecular networks

Standard structural variables describe the Gestalt of the trabecular network. These are aspects of the thickness, the separation, the number of the bony connections in this network called trabeculae as well as the amount of bone found in the volume of interest.

Following, a list of these structural variables is given with their identifiers used in the scientific community:

1. The number of bone voxels divided by the number of voxels in the whole volume of interest (Bone Volume over Total Volume, BV/TV)

2. The mean number of trabeculae detected along different directions through the volume of interest (Trabecular Number, Tb.N)

3. The mean thickness of trabeculae (Trabecular Thickness, Tb.Th)

4. The mean separation of trabeculae (Trabecular Separation, Tb.Sp)

5. The mean surface of bone voxels over the volume of interest (Bone Surface over Total Volume, BS/TV)

To determine the above variables, the continuous dataset of grey values has to be binarised. Due to a sufficient contrast provided by the modality Micro-CT this is done by simple thresholding in this study. This procedure delivers the voxels classified as bone. Hence, the fraction bone volume over total volume (BV/TV) can be determined. Subsequently, the number of phase changes between bone and marrow and marrow and bone over a set of equally spaced but randomly orientated test lines (see figure 2.8) through the volume of interest are counted. The process of choosing a random rotation α and subsequently adding the number of phase changes pc_α is repeated $N = 256$ times, resulting in $\alpha_1, \ldots, \alpha_N$ angles. Finally, for each angle α_i the number of phase changes pc_{α_i} is accumulated as well as the overall length of the test lines l_{α_i} for the angle chosen:

$$pc = \sum_{i=1}^{N} pc_{\alpha_i} \tag{2.1}$$

$$l = \sum_{i=1}^{N} l_{\alpha_i} \tag{2.2}$$

From these values, the following structural variables are determined:

$$Tb.N = \frac{pc}{l} \tag{2.3}$$

$$Tb.Th = \frac{BV/TV}{Tb.N} \tag{2.4}$$

$$Tb.Sp = \frac{1 - BV/TV}{Tb.N} \tag{2.5}$$

$$BS/TV = \frac{2 * Tb.N}{BV/TV} \tag{2.6}$$

All angles α_i define a three-dimensional vector through the volume of interest, i.e. $\alpha_i \in \left(\frac{-\pi}{2}, \frac{\pi}{2}\right) \times (0, 2\pi)$.

From a statistical point of view, two independent variables out of the set BV/TV, $Tb.N$, $Tb.Sp$, $Tb.Th$, BS/TV are sufficient to investigate this approach, since all the others can be calculated from the two given ones. In this study, BV/TV and $Tb.N$ are chosen.

2.4 Markov techniques

When investigating a set of structures, each structure is observed with a certain probability. The higher the number of elements building a structure and the higher the number of possible combinations, the more difficult a calculation of the probability of a given structure can be.

The typical measurement procedures usually induce a grid, thus establishing a process with discrete positions of its elements. Examples are voxels or pixels of two or three-dimensional structural images. Hence, a structure is decomposable in terms of its elements or small groups of interacting elements, the so called cliques. Moreover, the probability may be determined based on the neighbour relationships of these element groups. If two elements are unlikely to be combined, a structure containing this combination may have a low probability to occur, too.

The decomposition of the probability into potentials based on cliques of interacting elements or other local relationships is a strategy common to all Markov techniques listed in this chapter.

The three Markov techniques introduced in this chapter are related to each other in terms of building a chain of derived techniques: a Markov point process will be defined in terms of a Markov random field, and a Markov graph can be viewed as marked Markov point process coding father-son-relationships.

2.4.1 What is the Markov property?

Informally, the Markov property specifies the lack of unlimited memory of a stochastic process. In case of a realisation of a one-dimensional process, which is a sequence $\{X_n\}_{n\geq 0}$, we define the Markov property as following:

Definition 2.4.1 (Markov Property). Let n be a site, X_n the value of the process at the site n and the set $\{n-1, n+1\}$ the neighbourhood of site n. If X_n is independent of $X_k, k \notin \{n-1, n+1\}$ the underlying stochastic process generating X_n fulfils the Markov property[1].

The approach of limited memory can be generalised to Markov fields, Markov point processes as well as Markov graphs, as shown in the subsequent sections.

2.4.2 Why Markov techniques?

When investigating which stochastic process models a (stochastic) structure best, several aspects have to be taken into account:

- How does the technique handle complex structures, i.e. structures composed of multiple realisations of basic structural elements?

- Is a regeneration of a structure similar to the original one possible?

- How much information is preserved by the mapping of a structure to a parameter set of the technique chosen?

The Markov techniques introduced and summarised in the next sections all share a common answer to the questions mentioned above, as explained in the following sections.

---

[1]When discussing the lack of memory of a stochastic process a formulation handling the *past* may be more appropriate: $P(X_n = x_n | X_0 = x_0, \ldots, X_{n-1} = x_{n-1}) = P(X_n = x_n | X_{n-1} = x_{n-1})$. However, the natural ordering of time has no natural spatial analogue, thus it may be more convenient to work with the symmetric formulation of definition 2.4.1.

Markov technique	Partitioning/Factorisation Method
Markov random fields	potential functions partitioning the energy function
Markov point processes	factorisation by interaction functions
Markov graph	conditional probabilities for parental interactions

Table 2.3: Markov techniques and their methods of partitioning the overall probability of a realisation / configuration.

2.4.2.1 Decomposition of complexity

Complex structures can be decomposed into small subsets of structural elements which are interacting. In detail, the probability for an overall structure to appear as a realisation of a stochastic process is factorised in terms of these subsets, the *cliques*. This factorisation decomposes the structural complexity into simple basic elements and groups of elements which interact with each other (see sections 2.4.3.1, 2.4.4.1 and 2.4.11). An overview of the partitioning concepts for the Markov techniques discussed in the next sections is given in table 2.3.

2.4.2.2 Information preservation

When dealing with the task of generating a structure from a factorisation obtained by an original structure, the parameters of the factorisation are the key to a simple estimation of the probability of a proposed realisation.

The first step to retrieve the values of parameters describing a stochastic model from a given structure often is accomplished by the application of analytic or stochastic approximations of the maximum likelihood estimates of the factorisation [34]. Once, a structure is mapped to the vector of values of the model's parameter set, the amount of information of the structure preserved in this parameter set can be used to extract similar structures. Thus, a representation of a structure by the parameter set of the model applied can be viewed as representation of a *family of similar structures*.

An iterative approach to assimilate a proposed realisation to a given structure by modifying it step by step and subsequently measuring the increase (or decrease) of its overall probability to occur based on the factorisation of the original structure is available by the *Metropolis-Hastings algorithm* [35, 36], which was originally introduced in statistical physics [32, 37]:

The Metropolis-Hastings algorithm generates a discrete time Markov process [36] $X_0, X_1, \ldots$, where the transitions usually let the process $(X_n)_{n \geq 0}$ converge to a given limit distribution $P(\cdot)$ but allow a temporarily decrease of the likelihood to avoid local minima:

1. A proposal X_{i+1}^{prop} for a new state is made by typically modifying, adding or deleting (depending on the kind of the process) one element of the current structure X_i.

2. The proposal is accepted or rejected based on the likelihood of the proposed state compared to the old one:
   If $P(X_{i+1}^{prop}) \geq P(X_i)$, then the proposal is accepted, since the increased likelihood indicates that the Markov process $(X_n)_{n \geq 0}$ converges to the limit distribution $P(\cdot)$. If the probability decreases, that is $P(X_{i+1}^{prop}) < P(X_i)$ than the proposal is accepted only with probability $\frac{P(X_{i+1}^{prop})}{P(X_i)} < 1$.

2.4.2.3   Regeneration of a realisation

The application of the two steps summarised in the above two sections defines the inherent power of the Markov approach: A structure can be Leander in terms of the parameters of an underlying stochastic model. These parameters are strongly related to the factorisation of the model (by the Hammersley-Clifford theorem, see section 2.4.4.1), which enables a non-complex access to the overall probability of complex structures. Examples of the application of the Metropolis-Hastings algorithm on a parameter set of a given structure learned can be viewed in [34] and, reproduced, in section 2.4.3.2.

A simple visualisation of the learning and reproduction techniques of Markov point processes is given in figure 2.9. The two point processes show similar characteristics: the varying trend of the number of points per area along the vertical direction and the constant number of points per area along the horizontal direction. The second lower point process is a Metropolis-Hastings based realisation of the first point process.

2.4.3   Markov Random Fields

The first technique taken from the set of Markov processes is the Markov random field, which was the first approach investigated in this work and serves as a generalisation of the Markov point processes introduced later on.

2.4.3.1   Introduction

In case the sites $s \in S$ of a random process are arranged as a grid, the corresponding random variable can be interpreted as Markov random field, based on a neighbourhood system:

Definition 2.4.2 (Neighbourhood system). A neighbourhood system on the set of sites S is a family $\{N_s\}_{s \in S}$ such that for all $s \in S$,
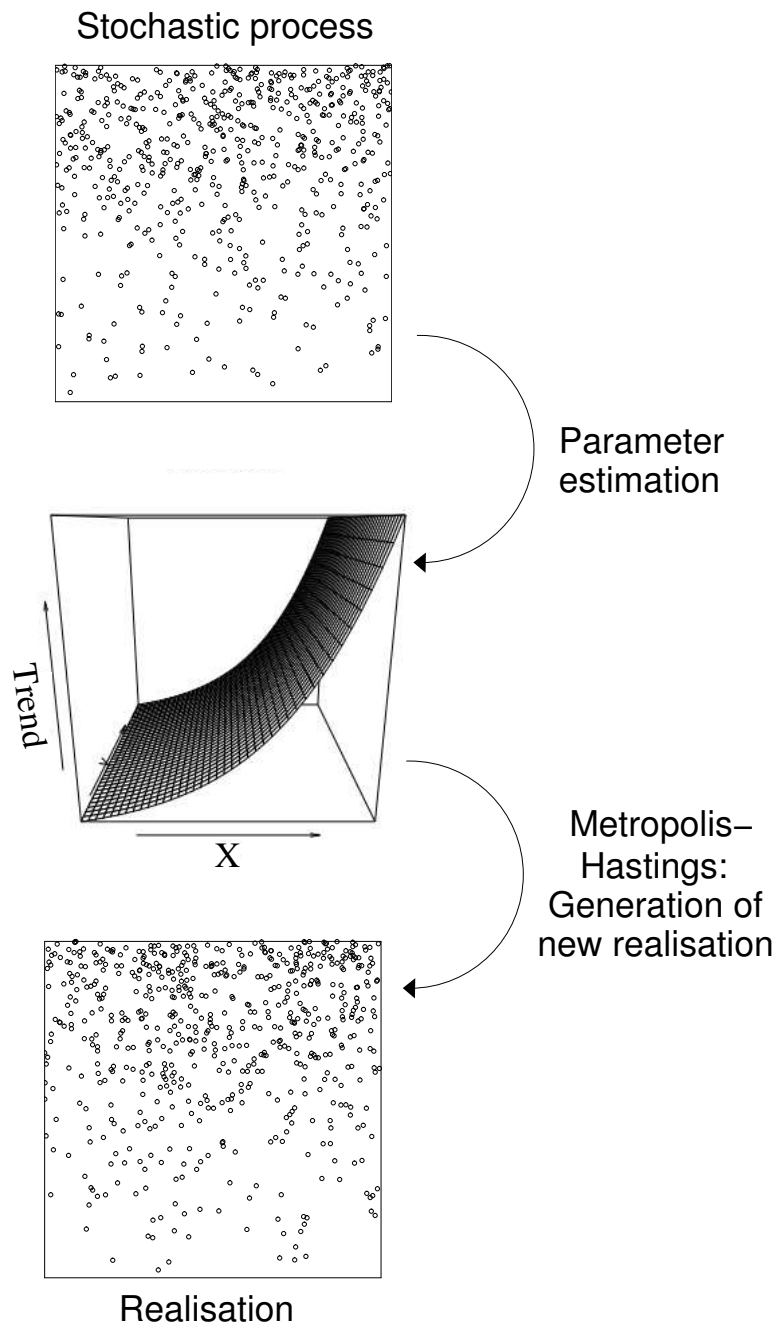
Figure 2.9: <u>Top:</u> a Poisson point process with a varying number of points per unit-area (intensity). <u>Mid:</u> trend of the intensity fitted to the Poisson process. <u>Bottom:</u> a Metropolis-Hastings generated point process showing a new realisation which is different but shows a similar pattern compared to the original process (top figure).

1. $s \notin N_s$

2. $t \in N_s \Rightarrow s \in N_t$

This definition states, that the interactions or neighbourhood relations of a Markov random field are bidirectional. The integration of the Markov property is done by the following definition:

Definition 2.4.3 (Markov random field). Let Δ be a set of possible values a configuration x can take at site $s \in S$. Given the configuration space $x \in \Delta^S$, a configuration is given by $x = (x(s), s \in S)$. For a neighbourhood system N and for all sites $s \in S$

$$P(X(s) = x(s)|X(S\backslash s) = x(S\backslash s)) = P(X(s) = x(s)|X(N_s) = x(N_s)) \qquad (2.7)$$

In other words, the dependence of a site $s \in S$ is restricted to and sufficiently described by the members of its neighbourhood N_s. The notation of the probability distribution of a Markov random field recruited from physics is given by

$$P(x) = \frac{1}{Z} e^{-\frac{1}{T}\varepsilon(x)} \qquad (2.8)$$

with Z called *partition function* [38] and $\varepsilon(x)$ named as energy of the configuration x. A possibility to partition the energy function is given by the introduction of *cliques* [39]. This decomposition of the neighbourhood allows to compute the probability of the realisation a Markov random field has (see figure 2.10):

Definition 2.4.4 (Clique). A singleton $s \in S$ is a clique. A subset $C \subset S$ with $|C| > 1$ is called a clique of the graph (S, N) if and only if any two distinct sites $s_i, s_j \in C, i \neq j$ are mutual neighbours.

To derive the energy function $\varepsilon(x)$ in terms of cliques, the following definition is given:

Definition 2.4.5 (Potential function). A set of potential functions $V_C, C \subset S$ is defined as

1. $V_C = 0$ if C is not a clique

2. for all $x, x' \in \Delta^S$ and all $C \subset S, (x(C) = x'(C)) \Rightarrow (V_C(x) = V_C(x'))$,

with $x(C)$ is the restriction of the configuration x to the subset of sites $C \subset S$.
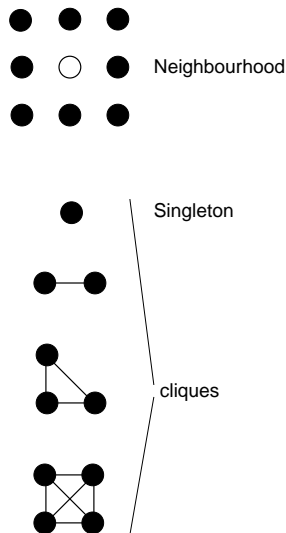
Figure 2.10: Cliques (up to a rotation) with respect to a given neighbourhood

.

This allows to determine the energy function of the Markov random field in terms of potential functions of the cliques with respect to the neighbourhood system [35]:

$$\varepsilon(x) = \sum_C V_C(x) \tag{2.9}$$

(A remaining problem is the estimation of the partition function Z.)

2.4.3.2   Topology and Markov random fields

Markov random fields are used to extract the typical interaction for a texture and subsequently generate a new but similar structure based on the interaction between the pixels. Pairwise interactions were used in figures 2.11 and 2.13 (taken from [34]) to model spatial dependence between pixels.

The nature of the textures in figures 2.11 and 2.13 seems to be reproduced adequately in the corresponding right textures 2.12 and 2.14. In contrast, figures 2.15 and 2.17 show textures with topological elements. Comparing these original textures with the reproduced ones (figures 2.16 and 2.18), the topological characteristics seem to be not catched in the pairwise interactions and thus did not show up in the regeneration of the textures.
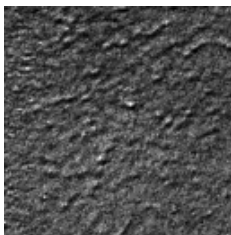
Figure 2.11:
Texture with
grainy char-
acter
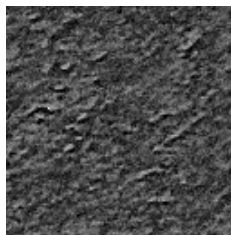
Figure 2.12:
Gibbs realisa-
tion of figure
2.11
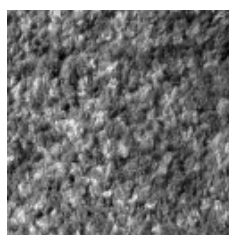
Figure 2.13:
Texture with
coarse grainy
character
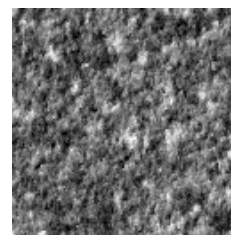
Figure 2.14:
Gibbs realisa-
tion of figure
2.13
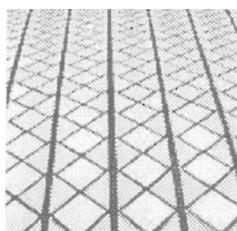
Figure 2.15:
Regular tex-
ture showing
topological
concepts.
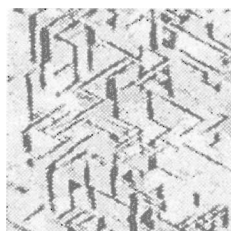
Figure 2.16:
Gibbs realisa-
tion of figure
2.15 with dif-
ferent topo-
logical con-
cepts
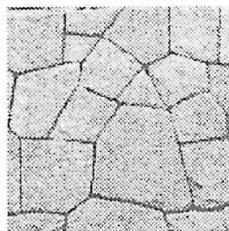
Figure 2.17:
Irregular tex-
ture showing
topological
concepts.

Figure 2.18:
Gibbs realisa-
tion of figure
2.17 with dif-
ferent topo-
logical con-
cepts

All figures 2.11-2.18 taken from [34]

Since this work is investigating structures for which topological elements are typical, there are (at least) two possibilities: the first is to choose a model which does capture the topological character of the texture to be learned, the second is a restriction of the textural elements to a subset the model is able to store, like junctions of lines or origins of lines and their direction.

The first approach is introduced in section 2.4.5 (especially in section 2.4.5.1.2), while the second strategy is presented in the following section.
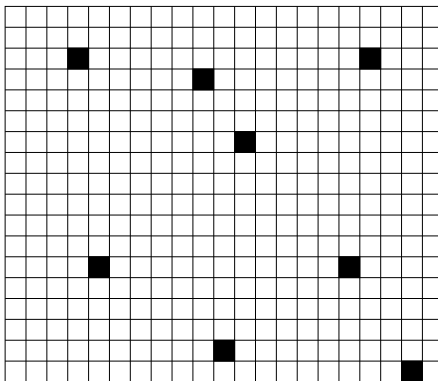
Figure 2.19: A Markov point process as (sparse) Markov random field.

2.4.4 Markov point processes

2.4.4.1 Introduction

A Markov point process can be derived from the definition of Markov random fields [35]. This is achieved by restricting (at first)[2] the set of possible values Δ at a site $s \in S$ to the set $\{0, 1\}$ (see figure 2.19). The neighbourhood system of a Markov point process is not any longer bound to the underlying grid, although discrete measurement spaces usually induce a grid on which the sites are arranged. The direct neighbourhood relations are replaced by distances in a metric space [36].

As in the case of Markov random fields, the overall probability distribution can be factorised: for a probability distribution on $\Delta^S = \{0, 1\}^S$ there exists a function $\phi : \{0, 1\}^S \rightarrow (0, 1]$ such that

$$P(x) = \prod_{\text{cliques } y \subset x} \phi(y) \tag{2.10}$$

and

$$(\phi(y) < 1) \Rightarrow ((s, t \in x \Rightarrow s \in N_t) \vee y = \emptyset) \tag{2.11}$$

which is a rephrasing of the *Hammersley-Clifford* theorem [36, 41]. An example of a pairwise interaction process with $\phi : S \times S \rightarrow (0, 1]$ (realised as $\gamma(\cdot, \cdot)$ modelling interaction of cliques with two elements) is

---

[2]When more information than the state $s \in \{0, 1\}$ has to be stored to model the underlying stochastic process appropriately, marked point processes allow to do this. By extension of the dimension of a point process they were shown to be equivalent to non-marked point processes [36, 40].

$$P(x) = \alpha \prod_{x_i \in x} \beta(x) \prod_{x_j, x_k \in x : x_j \ x_k} \gamma(x_j, x_k) \tag{2.12}$$

(with α being a normalisation constant and $\beta(x)$ is the intensity function). In order to model a point process consisting of discs of radius r not being allowed to overlap, the interaction function

$$\gamma(\{x_j, x_k\}) = \begin{cases} 1 \ if ||x_j - x_k|| > 2r \\ 0 \ otherwise \end{cases} \tag{2.13}$$

models this process. Another example would be given by setting $\gamma \equiv 1$ yielding a Poisson process.

The Hammersley-Clifford theorem can be used to design new Markov point processes: instead of defining a joint density $P(x)$ for all point patterns x, it is sufficient to define the interaction functions $\phi(\cdot)$. The combination of interaction functions in formula 2.10 in terms of multiplications can be interpreted as AND-relation: a single zero interaction will decrease the overall probability to zero.

2.4.4.2   Cluster Type Index and Ripley's-K functions

To facilitate the investigation and utilisation of structural characterisations assumed to be applicable to natural structures like trabecular networks, known point process measures are introduced and described in the following section. Their applicability is investigated in chapter 2.4.4.4.

A Palm distribution builds the basis for the first point process measure investigated in this work: the *nearest-neighbour distance distribution function*. This function represents the probability that the point process X places at least one point within distance r of a given point y:

Definition 2.4.6 (nearest-neighbour distance distribution function).

$$G(r) = P_y(\ d(y, X\{y\}) \leq r), \ \ r \geq 0 \tag{2.14}$$

with $d : \mathbb{R}^2 \to \mathbb{R}$ is the euclidian distance, and $r \in \mathbb{R}$ is the distance argument of the nearest-neighbour function.

Since the number of points of the realisation $N(X)$ is assumed to be non-zero, and the distance is estimated from a representative point y (which implies stationarity of the underlying stochastic process), the Palm distribution $P_y(\cdot)$ can be interpreted as conditional distribution and does not depend on the choice of y.

Replacing the palm distribution in 2.14 by the distribution of the Markov point process X, the *empty space function* is yielded:

Definition 2.4.7 (empty space function).

$$F(r) = P(\ d(y, X\{y\}) \leq r), \ \ r \geq 0 \tag{2.15}$$

Hence, by exchanging the Palm distribution $P_y(\cdot)$ by $P.(\cdot)$ (which is the normal probability $P(\cdot)$) the set of sites taken as basis for the estimation of the nearest neighbour is extended from the set of points $\{s \in \Delta^S | s \in X\}$ to the set of all sites $\{s \in \Delta^S\}$ of the point process. Thus, $F(\cdot)$ is the distribution function of the distance from an arbitrary point $y \in \Delta^S$ to the nearest point of the process. Again, the definition of F(r) does not depend on the choice of y.

These two structural measures, F and G, can be combined to a single measure indicating the tendency of a point process to build clusters or to build more regular patterns alternatively [36]:

Definition 2.4.8 (Cluster Type Index / J-function).

$$CTI(r) := J(r) = \frac{1 - G(r)}{1 - F(r)}, \ \ F(r) < 1 \tag{2.16}$$

with $r \in \mathbb{R}$ is the distance argument of the cluster type index.

While in the scientific community the identifier *J-Function* has been established, the name *Cluster Type Index* is used during this work to make clear, what purpose this function has.

A limitation of the nearest neighbour function G is that by definition it uses only the nearest distance to a neighbour available. Hence, it considers only the shortest scales of variation. An alternative when investigating the change of number of points with respect to an increase of the area under observation is *Ripley's K-function*, which is called *reduced second moment function* alternatively [42, 43, 44, 45, 46, 47]. This characterisation provides an estimate of spatial dependence over a wider range of scales compared to the G-function. The application of the K-function requires a point process which is isotropic.

Definition 2.4.9 (Ripley's K-function). $Ripley's K$-function of a stationary point process X is defined so that $\lambda K(r)$ equals the expected number of additional random points within a distance r of a typical random point of X. Here λ is the intensity of the process, i.e. the expected number of points of X per unit area.
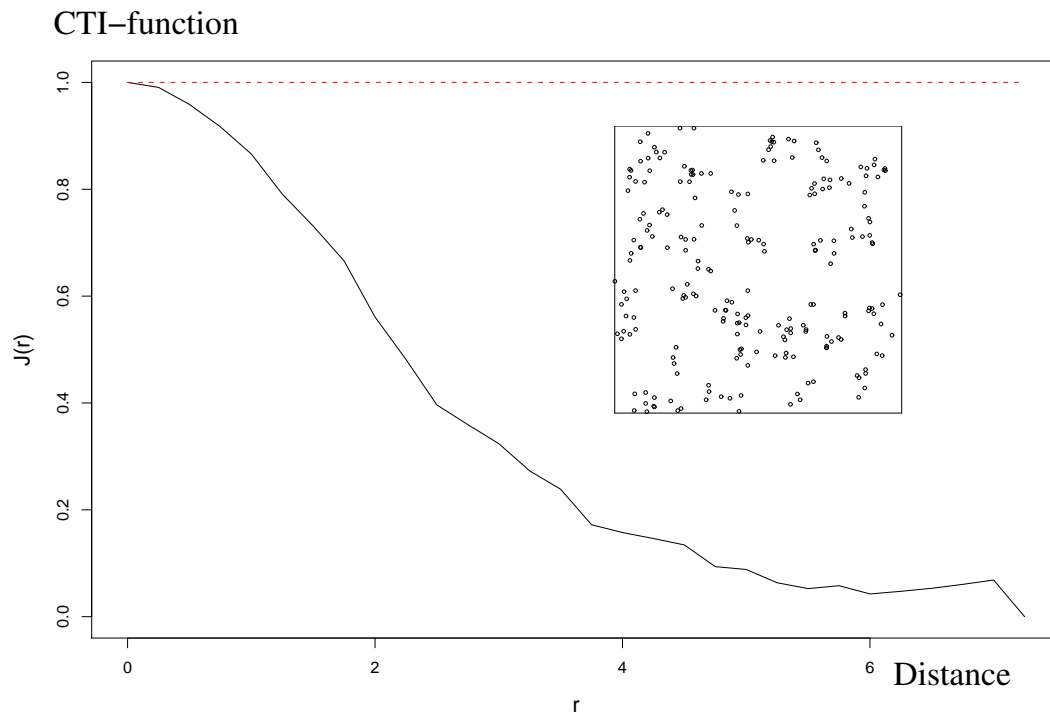
Figure 2.20: A Matern II cluster process (window size 100×100) and its CTI-function dropping below 1.0 and thus indicating clustering. The dotted line represents a reference Poisson process.
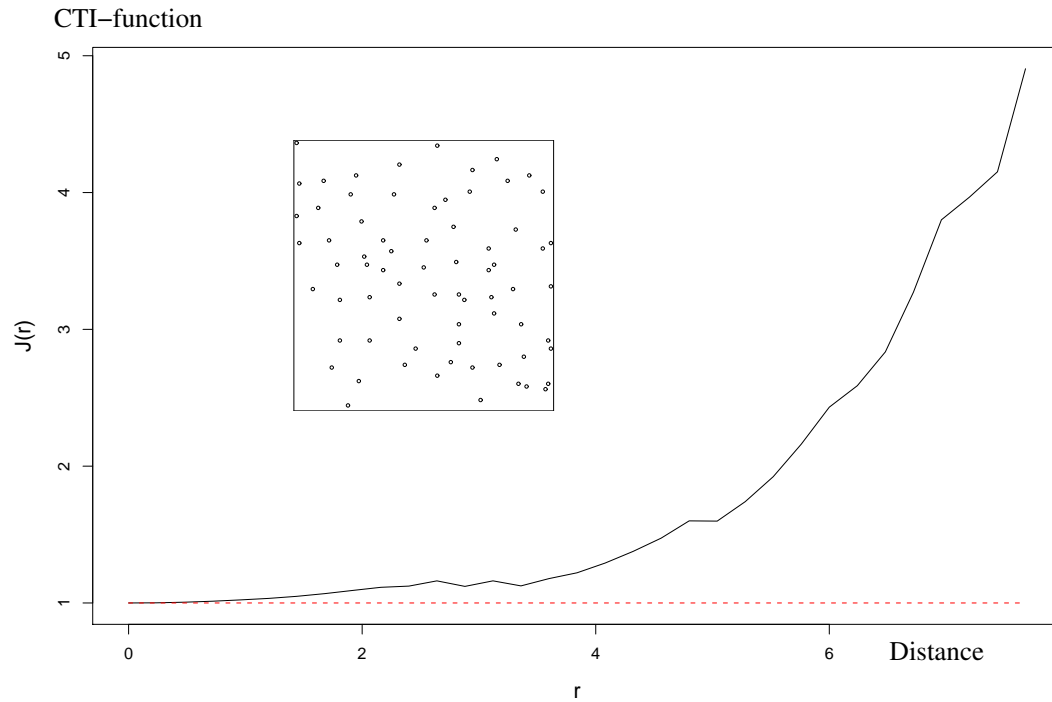
Figure 2.21: Swedish pine point process (window size 100×100) obtained from the Spatstat library and its CTI-function indicating a more regular pattern (inhibitance between the points/pines). The dotted line represents a reference Poisson process.

Function	Poisson point process reference value
F-function	$F(r) = 1 - \exp(-\lambda * \pi * r^2)$
G-function	$G(r) = 1 - \exp(-\lambda * \pi * r^2)$
CTI-function	$CTI(r) := J(r) = 1$
$Ripley's K$-function	$K(r) = \pi r^2$

Table 2.4: Structural variables of point processes with intensity λ and their reference values for Poisson point processes showing complete spatial randomness (CSR). Complete spatial randomness induces the equality of F and G: $F(r) = G(r) \ \forall r \in \mathbb{R}_{>0}$

An estimate of K derived from a spatial point pattern dataset is useful in exploratory data analysis and formal inference about the pattern [48, 49, 50]. In exploratory analyses, the estimate of K is a useful statistic summarising aspects of inter-point "dependence" and "clustering". For inferential purposes, the estimate of K is usually compared to the true value of K for a completely random (Poisson) point process, which is $K(r) = \pi * r^2$. Deviations between the empirical and theoretical K curves may suggest spatial clustering or spatial regularity.

The expected number of additional random points within a distance r of a random point equals to $\lambda K(r)$. Here lambda is the *intensity* of the process, i.e. the expected number of points per unit area. The K function is determined by the second order moment properties of X.

2.4.4.3   From trabecular networks to point processes

Trabecular networks are structures build of multiple bony connections (see figure 2.22, left). These connections, the *trabeculae*, can be classified to three discrete states: one-dimensional trabecular rods, two- dimensional trabecular plates and three-dimensional trabecular junctions. A network constructed only by one-dimensional trabeculae of three-dimensional junctions can be described easily with the tools of graph theory, namely an adjacency matrix. A network which shows two-dimensional, plate like structures is more difficult to describe. Under the hypothesis, that the number of elements connecting one or two-dimensional trabeculae may be of importance to the stability of the trabecular network, the investigation of these three-dimensional elements, the junctions, may be helpful for estimating the trabecular network's integrity. Without quantifying the relationship between the number of junctions between trabeculae and the stability of the network, it is obvious, that a set of unconnected trabeculae does not resist any force applied to it, while the same set of trabeculae connected by junctions shows increased stability. Junctions connecting trabeculae allow forces to interact, hence, the distribution of junctions may play an important role, too.
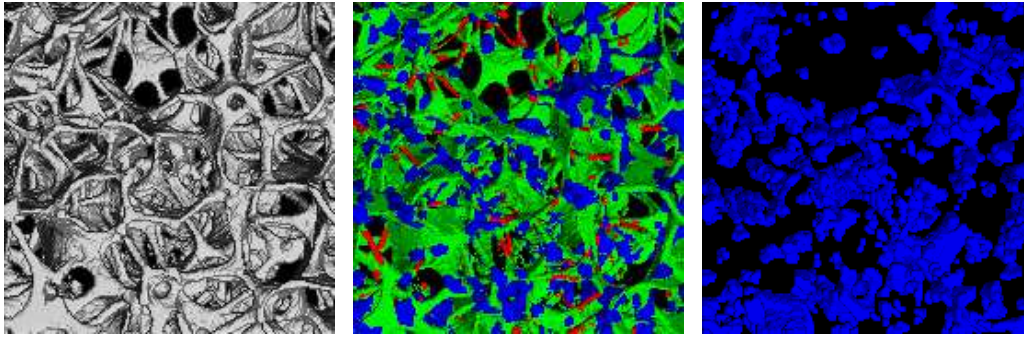
Figure 2.22: <u>Left:</u> Trabecular network as obtained as dataset from micro-CT. <u>Middle:</u>Classification of each voxel to its membership to a rod-like (red), plate-like (green) or junction-type (blue) trabeculae. <u>Right:</u> Restriction to junctions coded blue. All: Vertical projections through whole bone volume.

The hypothesis of this approach is based on the assumption that a relationship between the number and position of junctions and the integrity of the whole network exists: Structural measures which characterise the number and position of junctions with respect to each other are able to discriminate osteoporotic and healthy trabecular networks.

Having all junctions extracted from the trabecular network, a technique is needed to characterise the distribution of these connecting elements in order to find meaningful measures which can describe osteoporotic changes of trabecular networks.

Since the theory of point processes deals with multiple structures placed in a n-dimensional space, this framework can be utilised to describe distributions of junctions within the bone. Although the distribution of junctions is given in a three-dimensional space, we use two dimensional point process techniques in order to limit complexity of the problem and utilise fast, available estimation techniques for point processes [51].

2.4.4.4 Trabecular Junctions as Markov point process

The Micro-CT measurements used for this approach are described in section 2.2.2: the very high resolution dataset with a voxel size of $(25\mu m)^3$ was used in binarised representation.

For each volume data set of a vertebra a certain sequence of steps generated a model of the bone structure, a projection onto the subset of trabecular junctions (i.e. the voxel set classified as three-dimensional) and subsequently a set of point processes representing the centres of the trabecular junctions within horizontal planes (see figure 2.23):

1. Binarisation to extract bone voxels
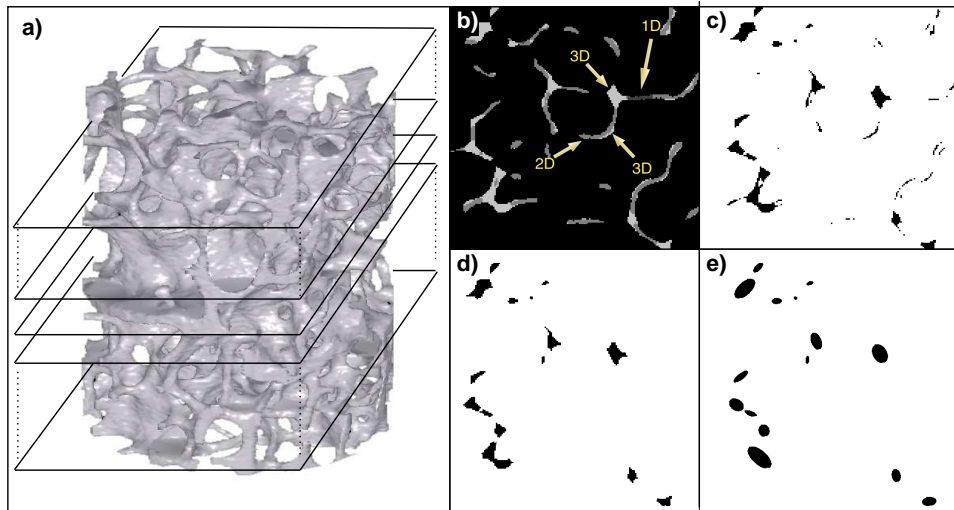
Figure 2.23: From a high resolution scan of a continuous network to a set of point process realisations and related measures: a) binarised volume, b) voxel set classified into one, two and three-dimensional types, c) projection to 3D elements, d) opening of the dataset to exclude small groups of voxels not belonging to a junction, e) fitted ellipsoids mark the locations of junctions and thus form a (marked) point process, from which measures like J and K-functions can be calculated. A stack of slice based realisations is retrieved by repeating b)-e) for different slices.

2. Calculation of the local dimension of each voxel

3. Restriction to voxel subset with assigned local dimension of three

4. Morphologically opening and closing the data set

5. Extracting two dimensional realisations of the point process given in 11 equidistantly spaced horizontal planes

6. Estimation of the point process measures F, G, CTI, and K

7. Calculation of the mean of CTI, and $Ripley'sK$ over the slices extracted for all realisations of a vertebra

The binarisation, the selection of 3D-typed voxels, the opening and closing of the data set as well as the extraction and subsequent superposition of realisations of the point process were performed using the software ImageJ (National Institutes of Health (NIH), Maryland, USA). The calculation of the local dimension of each voxel was done by in-house developed software tools, written by the author of this study, while the estimation of the characterising functions F, G, CTI and $Ripley'sK$ was achieved by using the *spatstat*-package of A. Baddeley [51] under the statistical software system R [52].

Since the binarisation and calculation of the local dimension are already described in section 2.1, the steps performed subsequently are discussed in the following subsections:

2.4.4.4.1 Restriction to voxels of a local dimension of three After classifying the voxel space into the types 0 (no bone), 1 (rod like, one-dimensional structure), 2 (plate like, two-dimensional structure), and 3 (junction type) a simple threshold of $t > 2$ allowed to extract the junctions of the three-dimensional network (see figure 2.23 b,c). The calculation of the local dimension is described in section 2.4.5.2.3.

2.4.4.4.2 Opening and closing A morphological opening and closing of the set of voxels of type 3 allowed to eliminate voxels which were found at the curved margins of trabeculae and thus were correctly classified as type 3 but did not belong to a junction. Since only margins of trabeculae showed such voxels, they were sorted out by performing an opening and closing of the dataset (see figure 2.23d).

2.4.4.4.3 Extraction of the Markov point process realisations A point process realisation from the binary slice pattern (see figure 2.23c) is obtained by fitting ellipses to each continuous pattern found in the slice extracted. The pattern of ellipses represents a marked point process. Finally, the centres of the ellipses are used as points.

A sequence of eleven point processes were extracted equidistantly from the stack of voxels restricted to three-dimensional junctions. Since the stack of voxels had a height of 10 mm, the distance between the eleven slices generating the eleven point processes were 1 mm. For the case that a biopsy was not measured exactly vertically adjusted, a potential slope of the axis of the biopsy will not have an impact on the result if the point measures J and K are computed from each point process realisation and subsequently averaged instead of super positioning the realisations and subsequently calculating the point process measures from the super positioned point process.

2.4.4.4.4   Estimation of CTI and $Ripley'sK$ The statistical software system R was used together with the package *spatstat* in order to map the realisations of point processes obtained by and exported from ImageJ to estimates of the distributions CTI, and $Ripley'sK$ by the $R/spatstat$-functions $Jest$ (J estimator)[3] and $Kest$ (K estimator) [51].

2.4.5   Markov graphs

While Markov random fields are based on predefined, local neighbourhoods, and sparse Markov random fields defined as Markov point processes use local neighbourhoods with a coarser scale, Markov graphs are able to specify neighbourhoods completely uncoupled from metrics: two nodes are neighbours if they are connected by an edge, independent of their distance with regard to any metrics.

Definition 2.4.10 (Markov graph, Part 1). A Markov graph consists of

- an undirected Graph $G = (V, E)$, where each vertex $v \in V$ represents a random variable in X and each edge $\{u, v\} \in E$ represents a dependency between the random variables u and v,

- a set of potential functions ϕ_k, one fore each clique k in G. Each potential function ϕ_k is a mapping from possible joint assignments to non-negative real numbers.

The joint distribution of the Markov graph is defined by:

$$P(X = x) = \frac{1}{Z} \prod_k \phi_k(x_k) \tag{2.17}$$

where x_k is the state of the random variables in the kth clique, and the normalization constant (or partition function) Z, where

---

[3]The Cluster Type Index CTI was defined as point process function J

$$Z = \sum_{x \in X} \prod_k \phi_k(x_k). \tag{2.18}$$

Every node v in a Markov graph is conditionally independent of any other node w, which is not connected by an edge to v, i.e. $\{v, w\} \notin E$.

Practically, the partition function Z is difficult to calculate. But there is a special case of Markov graphs, for which the calculation of the joint distribution simplyfies: Directed, acyclic graphs. In this study we were interested in neighbourhoods starting from a certain point in the voxel space and subsequently increasing the distance from this starting point. Looking at two points $x_i, x_j \in X$ neighboured in the voxel space X, the pair (x_i, x_j) were added to the Markov graph if it fulfils $dist(x_j, s) > dist(x_i, s)$ with s is the graph's root, otherwise the pair (x_j, x_i) were added. Hence, the Markov graph constructed consists of pairs of points in the voxel space which lead away from the graph's root s.

Definition 2.4.11 (Markov graph, Part 2). In the special case the Markov graph G is a directed acyclic graph (DAG), each clique represents a single directed conditional dependency. More precisely, the factorisation of the overall probability simplifies to conditional probabilities given by the node relationships:

$$P(x) = \prod_{v \in V} P(x_v | x_{pa(v)}) \tag{2.19}$$

for each node $v \in V$ and the set of parents $pa(v)$, which is the set of all nodes w which show a directed edge to v. $P(x_v | x_{pa(v)})$ is the probability of x_v, given that the parents of v and their values are known. The joint distribution thus requires as numerical input the conditional distribution of each node for any given configuration of its parents.

Hence, the overall probability of a realisation of a Markov graph can be factorised [53] similar to the Markov random fields and Markov point processes.

This approach allowed to define a topological object representing the typical behaviour of a structure with regard to their neighbourhood. In other words, Markov graphs were exploited to model transition probabilities from a typical point of the structure swarming in all directions. Having an anisotropic structure, these transition probabilities would reflect this anisotropy with regard to its direction. Moreover, the directed relationships implicate the graph being acyclic and directed, which simplifies the computation of its probability, as shown in the next section.

2.4.5.1   Information measures on graphs

For both approaches presented here, a *Directed Acyclic Graph* (DAG) is assumed. In consequence, some simplifications can be used, e.g. the reduction from observing cliques of nodes to observing simple father-son-relationships between nodes, coded as transition probabilities.

After coding structural characteristics of a given stochastic realisation as a Markov graph representing transition probabilities of the original structure, the question is how to make use of this graph. The most direct possibility of investigating this graph is to investigate the transition probabilities itself. For example, for two groups of structures which have to be discriminated, a subset of all transition probabilities may differ between these groups. The aim is to identify this subset to obtain a measure which successfully discriminates the two groups of structures.

A more comprehensive measure is that of investigating the degree of determinism inherent to the graph and thus to the structure. In other words, a structure which is mostly of random nature should show less determinism than a regular structure.

In this work the degree of determinism or randomness is investigated in terms of measuring *information*. Although a structure is, once measured and given as a dataset, static it is of interest to observe the step of extension when a structure is known partly and then enlarged. The extension of a known part to an unknown, expanded graph introduces a dynamic moment and thus allows to apply techniques taken from information theory which deal typically with sequences representing a timely dimension.

In the following sections, the mathematical background of both approaches will be presented:

2.4.5.1.1   Probabilities on nodes of a DAG   For a given binary texture, a possibility to characterise this structure is to store the structure into a (directed acyclic) graph by assigning a grey value to the nodes and voxel neighbourhoods to the edges while ensuring that the edges are always directed away from the origin[4]. The edges simply represent the rectangular grid of a voxel space (see two-dimensional example in figure 2.24).

For a given set of random positions $r_{k,l} \in S$ inside the binary structure S which are non-zero, that is $I(r_{k,l}) > 0$ with I is the grey value function, at each random origin $r_{k,l} \in S$ the surrounding substructure is added to the graph. Hence, each random position known to be non-zero builds the origin for which each node in the graph relative to this origin stores the probability to find a voxel which is non-zero with respect to the random origin:

---

[4]The directness of edges actually is needed for the second approach measuring entropy, not necessarily in the first approach investigating grey value probabilities, but is introduced in terms of consistency.
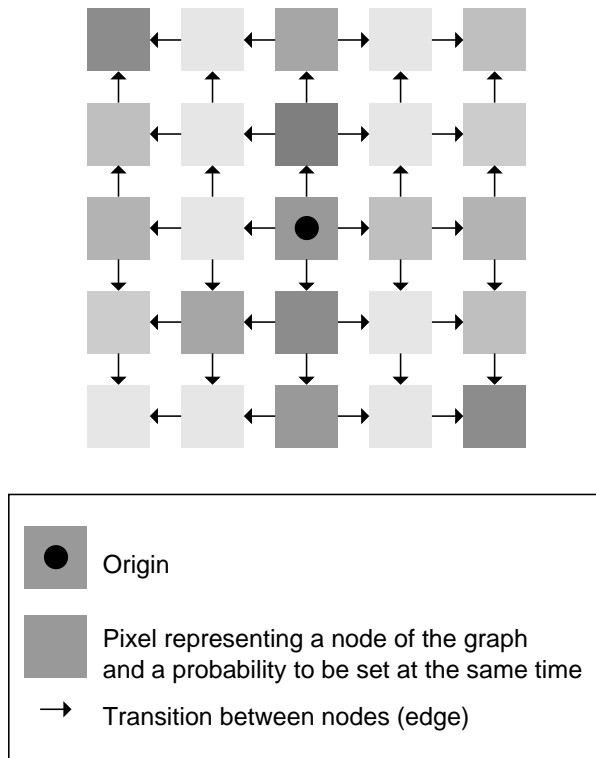
Figure 2.24: When several binary subimages are integrated with respect to different randomly chosen origins, the resulting directed acyclic graph represents grey value probabilities and directed neighbourhoods

For a given set of random origins $|\{r_{k,l} \in S | I(r_{k,l}) \neq 0\}| = n$ with cardinality n, the probability of finding a non-zero voxel at a relative position $r_{k,l} + x_{i,j}$ is defined as:

$$P(I(x_{i,j})|I(x_{0,0}) = 1) := \frac{1}{n} \sum_{r_{k,l} \in S, I(r_{k,l})=1,} I(x_{i,j} + r_{k,l}) \tag{2.20}$$

By definition, for anisotropic structures, e.g. textures which show mainly vertical substructures, the probability of nodes in the vertical direction should be higher than that of nodes in the horizontal direction. For isotropic structures the probabilities in these two directions should assimilate to each other.

The graph utilised here modelled a three dimensional grid of $11 \times 11 \times 11$. The size of a voxel was $(156 \mu m)^3$. It has been taken into account, that the number of voxels is growing with x^3 for a three dimensional volume. Hence, the corresponding neighbourhood had a volume of ca. $1.7 mm^3$. Connections existed to the direct six neighbours. The size of the neighbourhood chosen was a trade off between a volume to be maximised and the number of nodes to be limited in terms of avoiding complexity.

Each vertebral data set was binarised as described in section 2.2.3. For each vertebra a set of 50 random positions was identified for which the corresponding voxel was inside the binary structure $S\big|_{\{s \in S | I(s) \neq 0\}}$. In other words, the centres of the local volumes were set into the bone phase of the measurement, not the marrow phase. For each random origin, a neighbourhood graph starting at this origin was determined coding the voxel neighbourhoods inside the bone phase. All 50 resulting neighbourhood graphs were then integrated by overlaying them with respect to their origins. At each node at a certain position of the resulting graph a mean probability were obtained by dividing the number of nodes in the local graphs found at this position by the number of graphs investigated, which was 50 in this investigation.

To evaluate whether there existed nodes showing probabilities typical of the FX group or the Non-FX group, each node's probability was subject to investigation. This resulted in $11 \times 11 \times 11 = 1,331$ different variables potentially reflecting a difference between the two sample groups.

2.4.5.1.2 Conditional Entropy on edges of a DAG

Mathematical theories of communication were introduced to describe the procedure of transmitting data in the first quarter of the 20th century [54, 55, 56, 57]. The aim was the definition of a measure for the syntactic content of information. The concept of information describes the reduction of uncertainty due to a message $c \in A^n$ received, based on existing knowledge about the source of messages observed. A message is a series of letters $c = (c_1, \ldots, c_n)$ built from an alphabet A.

The basic idea is to ask whether a given structure $(c_1, ..., c_n)$, consisting of letters c_i of an alphabet A gives some hint for the extension $(c_{n+1}, c_{n+2}, ...)$ of this sequence, or if this extension is independent of the prefix $(c_1, ..., c_n)$.

2.4.5.1.3 Nondeterminism and order: two extremes in the space of predictability
A system which shows nondeterministic characteristics can be assigned to a state between the two extremes of a random or an ordered system. Now two simple examples of these two extremes are given: the first one consists of a purely random structure, where each subsequence is independent from its prefix, the one-dimensional Bernoulli sequence (see figure 2.25):

Example 2.4.1 (Bernoulli sequence).
Each letter c_i of the sequence $(c_1, ..., c_n)$ is drawn independently with regard to certain probability distributions $p(c_1), ..., p(c_n)$ and subsequently concatenated to each other. For example the sequence 010101110010100101 is an example for such a Bernoulli sequence. The probability for a letter c_{k+1} as an extension of the sequence $(c_1, \ldots, c_k)$ is given by the equation

$$p(c_{k+1}|(c_1, \ldots, c_k)) = p(c_{k+1}) \tag{2.21}$$

Hence, the knowledge of the prefix $(c_1, \ldots, c_k)$ does not reduce the uncertainty about the letter c_{k+1} to follow. The information gained is maximal at each step for this system.

The second example is the opposite of a random structure:

Example 2.4.2 (Deterministic sequence).
A completely ordered, periodic sequence of letters $(c_1, ..., c_n)$ with the condition $c_i = c_j, j = i + t$ for some fixed period length t is given. A trivial example with a period of $t = 3$ is *abcabcabc...* (see figure 2.25). Within this sequence, all future extensions of a prefix are determined, if at least three letters are known: from any subsequence $(c_i, c_{i+1}, c_{i+1}) \in A^3$ the letter c_{i+3} is known as letter c_i with probability

$$p(c_{i+3} = c_i|(c_i, c_{i+1}, c_{i+2})) = 1 \quad . \tag{2.22}$$

Thus, the knowledge of the prefix (c_i, c_{i+1}, c_{i+2}) does completely reduce any uncertainty about the suffix c_{i+3}. Since no uncertainty exists after a period was observed, the amount of information gained is zero for this system.

This conditional probability can be interpreted as the degree of predictability of an extension of a known structure. To extend this predictability to the conditional entropy as a measure of uncertainty of extension, the term entropy is introduced now within the context of symbolic sequences.

2.4.5.1.4 Entropy as a measure of information Based on a set of structures of different sizes, for example sequences of symbolic elements, a probability density can be defined. Furthermore, a measure of information of these substructures can be defined based on this probability density. In fact, the *block entropy*, which can be interpreted as *mean uncertainty* for a set of sequences (strings) $c \in A^n$ of length n of an alphabet A with λ elements is defined as a functional H of p [40]:

$$H_n = - \sum_{(c_1,...,c_n) \in A^n} p(c_1, ..., c_n) \log_\lambda p(c_1, ..., c_n) \tag{2.23}$$

To extend this approach to the problem of measuring the informational gain when extending a given sequence of length n by one element, we use the definition of conditional entropy [40]:

$$\begin{aligned} H_{n+1|n} &= \sum_{(c_1,...,c_n) \in A^n} p(c_1, ..., c_n) \times \\ &\times \; - \sum_{c_n \in A} p(c_{n+1}|c_1, ..., c_n) \log_\lambda p(c_{n+1}|c_1, ..., c_n) \end{aligned} \tag{2.24}$$

The gain of information obtained by the extension of a sequence by one element calculated using equation 2.24 can be used to determine the existence of relationships between subparts of a structure since the range of correlations determines the characteristic type of informational gain over several steps (see figure 2.25).

2.4.5.2 Application to trabecular networks

While the evaluation of node probabilities can be directly applied to binarised trabecular networks as described in section 2.4.5.1.1, the application of the concept of local conditional entropy required some preparatory steps: The continuous space of densities measured and discretised by the Micro-CT had to be transferred into a symbolic space reflecting the neighbourhood relationships of bone voxels.

As underlying model the biopsy dataset obtained with a voxel size of $25\mu m$ was used (see section 2.2.2.1).
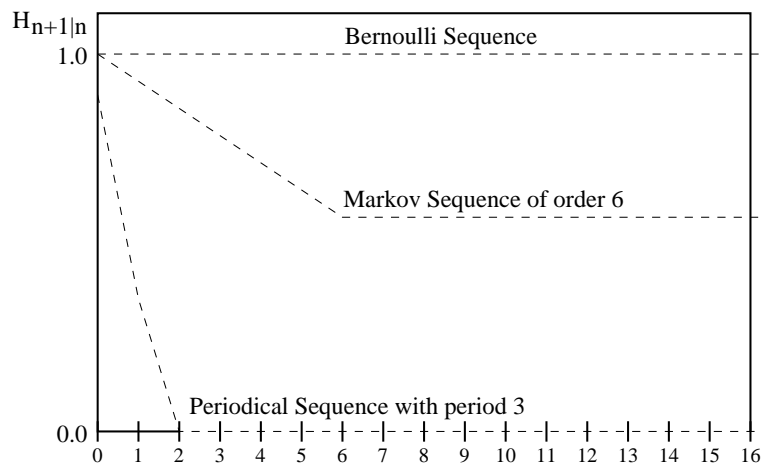
Figure 2.25: The conditional entropy depends on the range of correlations. A Bernoulli sequence shows no correlation between any two elements (with reference to equation 2.21), thus the gain of information (i.e. the uncertainty) when extending the sequence by one element is maximal each time. A Markov sequence with limited range of memory (here within a distance of 6) shows a decreased informational gain within its range of memory, but preserves a certain level of informational gain when extending the sequence behind the range of its memory. The periodical sequence does not gain any information when its period is known (after [40]).

2.4.5.2.1   Mapping the voxel space to a symbolic space   To assess measures
of complexity a symbolic representation of the trabecular network was created. This
was achieved by performing a discretisation of the continuous values of the trabecular
network using the values of the voxels and their neighbourhoods. The following four steps
were used to map the continuously valued voxel space to the discretely valued symbolic
representation:

1. Binarisation

2. Calculating the local dimension of a voxel

3. Exclusion of ambiguities when detecting relationships between voxels

4. Extraction of symbolic sequences out of the 3D-volume.

2.4.5.2.2   Binarisation   The first step towards a symbolic description of the trabec-
ular network was a classification of the voxel space into two types of voxels: *bone* and
marrow. Since the bone biopsies were measured with a high resolution of 25 μm, a high
contrast between bone and marrow was achieved as described in section 2.2.3. As a result,
the classification into bone and marrow voxels was possible by applying fixed threshold
to the continuously valued voxels.

2.4.5.2.3   Decomposition by local dimension   Secondly, a refinement of the clas-
sification of the bone and marrow voxels into three categories was performed. For each
voxel of the type bone the local dimension was calculated (see figure 2.26). This was
achieved by a technique which was used by Bruske [58]: For each voxel, the set of rela-
tive vectors to its neighbour voxel of the type bone within a distance of five voxels was
determined. Based on this set $A^T = (v_1, ..., v_n)$ a *Local Principal Component Analysis*
(LPCA) was performed by calculating the set of eigenvalues μ_i of the covariance matrix
$\sigma = \frac{1}{N} A^T A$. To assess the local dimension of a voxel, the number of eigenvalues which
fulfil the criterion of Fukunaga et. al. [59] was used. This criterion regards an eigenvalue
as significant if the equation

$$\frac{\mu_i}{max\mu_j} > a \tag{2.25}$$

is fulfilled. Experiments showed that a value of a=5 resulted in reasonable classifications
of the local dimension. This classification founded an estimation of the role a single
voxel plays in the framework of the trabecular network: a dimension of one is likely to

correspond to a voxel of a rod-like trabecula, a dimension of two may correspond to a plate-like type, and a dimension of three belongs to a voxel of a junction type. Of course, the set of voxels of a trabecular network cannot be partitioned into these strict cases since usually mixtures of these three types are found.

The preceding steps of binarisation and calculation of the local dimension transformed the continuously valued volume of the trabecular network into a discretely valued volume of the types:

- Marrow

- Bone with assigned local dimension of 1.

- Bone with assigned local dimension of 2.

- Bone with assigned local dimension of 3.

Thus, the voxels as well as the relationships between neighboured voxels of the measured volume were described on a symbolic level.

2.4.5.2.4   Removal of ambiguities   Thirdly, due to the cylindrical shape of the biopsy the set of distinguishable neighbourhood relations had to be determined. In our case, a rotation of the cylindrical biopsy around its main axis was not detectable. Additionally, the orientation of the biopsy upwards or downwards was not distinguishable (see figure 2.27). In consequence, the only relationships between neighboured voxels which could be taken into account were the vertical and the horizontal directions. Thus, all possible horizontal directions from a voxel to its neighbours were grouped into the *horizontal class h*. Similarly, the directions upwards and downwards built the *vertical class v* of neighbourhoods.

2.4.5.2.5   Symbolic sequences of a 3D-structure   The classification of the bone voxels into three classes of dimensions on the one side as well as the neighbour relationships of the type *horizontal* and *vertical* on the other side were sufficient to build sequences of voxel relationships on a symbolic level: considering a bone voxel v_1 with an assigned local dimension of 3 and its vertically neighboured bone voxel v_2 with an assigned local dimension of 2, we expressed this relationship as the symbolic code $v32$. More generally, all relationships between neighboured voxels were written by an symbolic code out of the set

$$A = \{v11, v12, v13, v21, \ldots, v33, h11, h12, h13, \ldots, h33\} \tag{2.26}$$
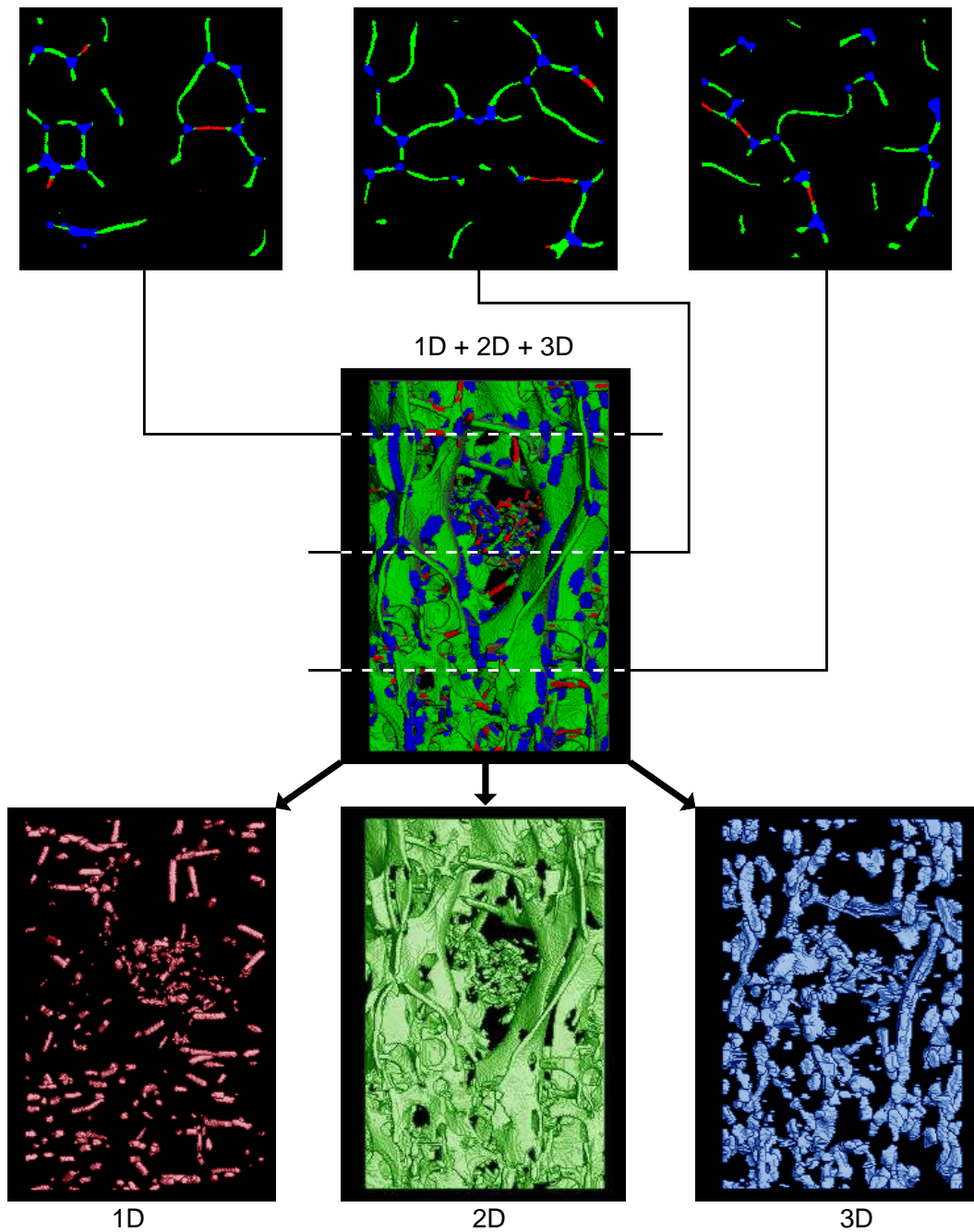
Figure 2.26: <u>Top:</u> slices of a voxel set classified with regards to each voxel's local dimension. <u>Middle:</u> resulting decomposition of the trabecular network into disjunct voxel sets of dimensions 1 (red), 2 (green) and 3 (blue). <u>Bottom:</u> rendering of the disjoint sets of dimensions. The assignment of a local dimension to each voxel is a main step towards a symbolic representation of neighbourhood relationships.
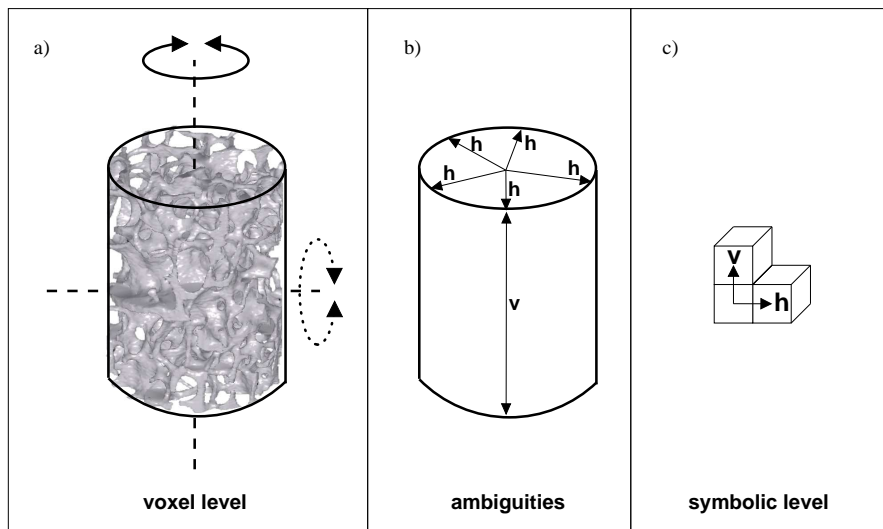
Figure 2.27: <u>Left:</u> due to the cylindrical shape of the biopsies a rotation along the main axis as well as the up and down side cannot be distinguished. <u>Middle:</u> as a consequence, all horizontal directions are grouped into the horizontal class h, and the directions upwards and downwards build the vertical class v. <u>Right:</u> thus, the resulting symbolic representations of distinguishable neighbourhood relations consist of the two symbols v and h.

Based on this alphabet A with its 18 symbolic descriptions of voxel transitions, a set of symbolic sequences of length n was defined as follows:

$$A^n = \{(c_1, \ldots, c_n) | c_i \in A, i \in \{1, \ldots, n\}\} \tag{2.27}$$

In order to obtain the alphabet A^n, for each biopsy a graph of transition probabilities was built (see figure 2.28). The sequences of transitions between the voxels were determined by recursively finding all possible symbolic sequences of transitions from a junction type voxel (a voxel with assigned dimension of 3) to neighboured bone voxels within a certain distance. Each node of the resulting tree coded a voxel of a certain type, and each edge of the tree coded the transition probability of the source voxel to a target voxel with a certain dimension and direction. This graph of conditional transition probabilities was suitable for calculating the locally bound conditional entropy of the underlying trabecular network as a measure of order. The function of the conditional entropy over a distance of two to eighteen voxels was calculated and compared with regard to the osteoporotic and non-osteoporotic vertebrae.

As specified in section 2.4.5.2.3 the local dimension assigned to each voxel of type bone represented the dimension of the local volume (all voxels within a distance of 5) around
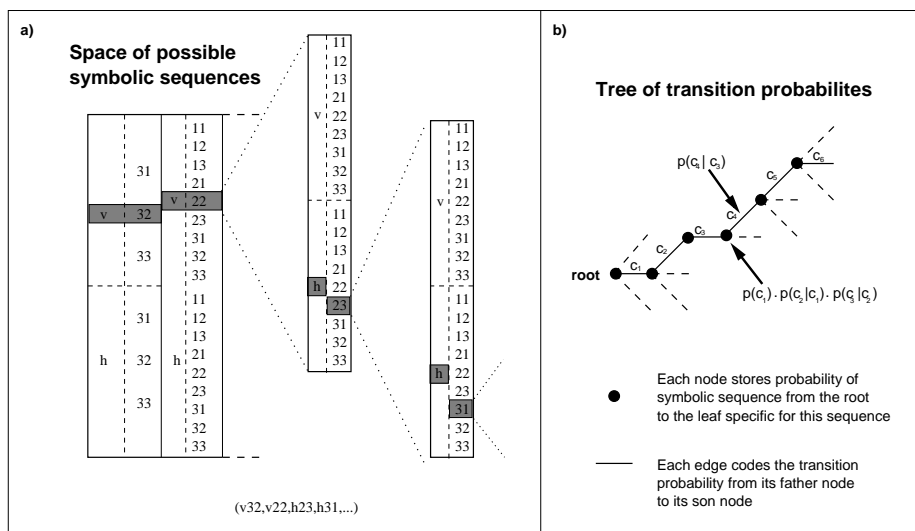
Figure 2.28: <u>Left:</u> sequence of neighboured voxel relationships taken from the space of transition probabilities between classified voxels. <u>Right:</u> tree of probabilities: Transition probabilities are stored in the edges, while probabilities of sequences (and all prefixes) are stored in the nodes.

each voxel. This classification enabled the extraction of transitions from voxels to their neighbours while collecting the direction (*horizontal* or *vertical*) as well as the local dimension of a voxel and its neighbour. Doing this, a sequence of transitions defines a sequence of symbolic descriptions of these transitions (see figure 2.28).

2.4.5.2.6   Tree of transition probabilities   Having performed all the preceding steps 2.4.5.2.1 to 2.4.5.2.5 a binarised trabecular network were transformable to a tree storing the symbolic transitions as well as their transition probabilities and the probabilities for each node (see figure 2.28). Hence, formula 2.24 allowed to map a sample network to a function of a discrete[5] distance to entropy.

2.4.6   Hidden Markov Models (HMM)

When observing noisy representations of a structure like a HRCT measurement, the question for each voxel is: is the grey value assigned to this voxel mainly influenced by the structure, or by the noise overlaying the measurement? Obviously, a Markov technique would incorporate local relationships between the voxel observed and its neighbours.

---

[5]The voxel size, i.e. the distance between the centres of neighboured voxels define the discrete steps at the symbolic level.

When investigating HRCT measurements the resolution is not appropriate to depict all structural details found in trabecular networks. It is expected to get a representation of the trabeculae which are the thickest. It was determined that the vertically orientated trabeculae may be those with the highest possibility to be reflected due to their thickness of circa 30% being over that of horizontal trabeculae [60]. In consequence, the task of detecting a vertical trabecula is equivalent to follow grey value peaks over a stack of horizontal orientated slices and at the same time estimate its state: bone or not bone (e.g. marrow, blood vessels). An observed transition probability between bone and bone, bone and marrow, marrow and marrow as well as marrow and bone will lead to the utilisation of HMM-techniques.

2.4.6.1 Introduction

A simple form of Markov models are Markov chains suitable for the statistical characterisation of sequences of symbol or states generated by stochastic processes. Principally, these are the basis for the formulation of the Markov property (definition 2.4.1). Hidden Markov models describe a double stochastic process: the first layer is defined by a finite automaton with edges between arbitrary states stemming from a finite state set. To each edge a transition probability is assigned. Actually, the probability for being in a certain state at time t is defined solely by the state visited at time $t-1$ (i.e. the Markov property holds). Since this state machine is assumed to be invisible, the model is called *Hidden Markov model*.

The Markov model produces for every time t an emission o from a limited set of possible emissions O. The probability density depends only on the current state s_t at time t, not on any preceding states or emissions. Thus, the conditional probability of emitting o at being in state s, $P(O_t = o_t|S_t = s_t)$ almost completes the definition. The last part missing for a complete definition is the specification of initial probabilities when a HMM is started. Thus, a HMM λ is defined [61] by the set:

- A finite set of states $S = \{s \mid 1 \leq s \leq N\}$

- A matrix A of transition probabilities
  $A = \{a_{ij} \mid a_{ij} = P(S_t = j \mid S_{t-1} = i)\}$

- A vector of initial probabilities $\pi = \{\pi \mid \pi = P(S_1 = i)\}$

- A matrix of emission probabilities $B = \{b_{jk} \mid b_{jk} = P(O_t = o_k \mid S_t = j)\}$

Hence, a set $\lambda = \{\pi, A, B\}$ specifies a HMM.

2.4.6.2   Three standard learning tasks of HMM

In order to utilise a HMM for the task of detecting single trabecular trajectories over a sequence of images orthogonal to the direction of the trabecula, first the image characteristics have to be transferred to the Hidden Markov model. This can be achieved by training a model with image characteristics, which is one out of three standard techniques available for HMMs:

Given a HMM λ and a sequence of observations $o = o_1, \ldots, o_T$,

- **The evaluation problem**
  What is the probability that the observation o was generated by λ, i.e. $P(o \mid \lambda)$

- **The decoding problem**
  What is the most likely state sequence s in the model λ that produced the observations o?

- **The learning problem**
  What model parameters $\{\pi, A, B\}$ do maximise $P(o \mid \lambda)$

For all of the three standard HMM problems standard techniques exist to solve them [61]. Hence, the application of a HMM to noisy HRCT data is done in two steps: first, by solving the learning problem, that is the adaption of a certain HRCT data set to the model parameters $\{\pi, A, B\}$. Second, the determination of the most likely state sequence s is determined for the learned model λ, which is over a trajectory of observations like grey value, area of the grey value peak and possibly lateral motion when following a grey value peak over a stack for each position the underlying state of which (bone or not bone) is estimated by evaluation of transition and emission probabilities.

2.4.6.3   Detection of Trabeculae by HMM - Proof of Concept

The application of Hidden Markov models to the task of tracking grey value peaks over a set of slices is performed as a proof of concept with the following steps:

2.4.6.3.1   Training a HMM by a HRCT measurement   A HRCT measurement obtained in vivo of the vertebra T12 was achieved with the parameters: $120kV$, $360mAs$, slice thickness of $0.4mm$, reconstruction kernel $B80s$ on a Sensation 16 clinical scanner (Siemens, Erlangen) using the helical mode. The reconstruction was performed with a field of view of 80mm, which, based on a matrix of 512×512 pixels to an anisotropic voxel size of $156\mu m \times 512\mu m \times 300\mu m$. A stack of 80 slices contained the complete vertebrae,

although the number of slices may differ slightly in other measurements depending on the angle the vertebra T12 has with respect to the CT coordinate system. A slice of a typical HRCT measurement is given in figure 2.2.
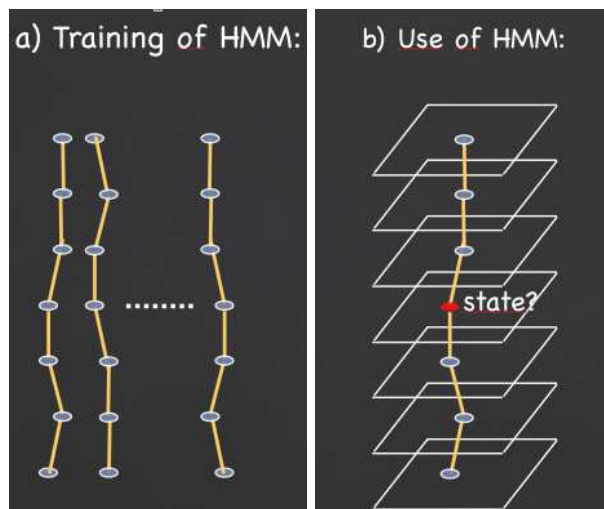
Figure 2.29: a) A tracked sequence of grey value peaks over a stack generates a sequence of observations. Multiple sequences can be used to train a HMM in order to b) subsequently ask for a given state and a tracked corresponding observation sequence, whether the underlying state is bone or marrow.

An in-house developed software was based on the software package *ImageJ* (provided by the Research Services Branch (RSB) of the National Institute of Mental Health (NIMH), part of the National Institutes of Health (NIH)). The Java-plugin written for ImageJ utilised additionally the HMM library of Jean-Marc François (Université Liège, Belgium).

The HRCT measurement was transformed by the ImageJ plugin into a series of grey value peaks with three associated values for each peak: the maximal grey values for each peak, the area defined by the surrounding minima of the peak and the lateral movement when tracked over the image stack.

This triple defined the observation, while the states used for the HMM simply were bone and not-bone. The sequences of observations were used to train the HMM by means of a Baum-Welch-Learner [61] which fixed the HMM parameters $\lambda = \{\pi, A, B\}$.

2.4.6.3.2 Bone or noise? Classification by HMM For the same set of observations o obtained from the HRCT image for which the HMM parameters were trained, the Viterbi algorithm [61] maximised the probability of a sequence s with regard to λ:

$$s^* \;=\; \operatorname*{argmax}_{s} P(s \mid o, \lambda). \tag{2.28}$$

For any state, within the sequence s, the classification problem was solved by this algorithm. Hence, for every grey value peak extracted from the HRCT image, the corresponding observation sequence was identified which included this peak and the probability maximisation delivered the most probable status of the position of the peak: bone or not-bone.

Chapter 3

Results

Results obtained during this study include a variety of statistical descriptions and evaluations of the study population and the structural variables evaluated in this study: first, a basic description of the study population is given in terms of basic measurements and standard structural variables (3.1) followed by the three Markovian structural variables introduced in this study (3.2). All variables are tested with regard to the normal distribution property to validate the applicability of parametric tests. Second, the discriminative power of each standard and Markovian variable is compared. Third, a nominal logistic fit allowed to build a combined model to estimate the degree of explanation of the variation of the fracture status for both the standard and Markovian approaches. Fourth, a risk estimation based on standardised odds ratios allowed to compare the risk an individual encounters when a variable measured in this study changes.

The local dimension was calculated as intermediate step to obtain the conditional entropy. The meaning of the composition of a trabecular network in terms of the dimensional type of its voxels was investigated, too (3.6).

The possibility of performing an ROC analysis in terms of comparing ROC curves with the test proposed by Metz [62] was not given since the sample size was only a third (FX group: 14) and a half (Non-FX group: 25) of the size specified by Metz as minimal (50 cases in each group) for being sufficient to draw meaningful conclusions [62].

3.1   Reference variables

The set of reference measures to which the approaches investigated in this study are compared consists of a measurement of bone mineral density as well as standard structural variables.

Since the bone mineral density was determined by means of whole vertebrae, this variable was not available for the biopsies taken from a subpart of the vertebral body. As a replacement, the bone volume to total volume fraction (BV/TV) of the volume of interest evaluated was measured by use of a micro-CT.

Variable names referring to measurements of the whole vertebrae are followed by the appendix $_{whole}$, while variables related to (parts of) the biopsies show other appendices (e.g. $_{mid}$ specifying the middle part of the biopsy), which corresponds to the evaluation volume of the Markovian variables.

In this section, the similarity of the basic distributions BMD_{whole}, BV/TV_{mid} and AGE to a normal distribution was evaluated using the Shapiro-Wilk test. Subsequently, the necessity to correct for possible significant differences between the fracture and non-fracture group are investigated.

3.1.1   BMD, BV/TV and AGE

3.1.1.1   Normal distribution property

Bone mineral density BMD_{whole}, BV/TV_{mid} and AGE were tested with respect to the normal probability distribution property by use of the Shapiro-Wilk test. The H_0 hypothesis that the distributions are normal was not rejected for any of the three variables, thus parametrical tests were used for BMD_{whole}, BV/TV_{mid} and AGE.

3.1.1.2   Descriptive statistics of BMD, BV/TV and AGE

As stated in section 3.1.1.1, the distributions of BMD, BV/TV_{mid} and AGE are classified as normally distributed. In table 3.1 the parameters of the normal distributions can be found:

n=39, (FX=14, Non-FX=25)	Mean		StdDev
$BMD_{whole}[mgHA/ml]$	60.7	$\pm$	24.56
$BV/TV_{mid}[\%]$	6.67	$\pm$	2.41
AGE	81.62	$\pm$	6.9

Table 3.1: Mean and standard deviation of the three basic study distributions BMD_{whole}, BV/TV_{mid} and AGE.

3.1.1.3 Fracture discrimination of BMD, BV/TV and AGE

In order to investigate the discrimination of a variable with respect to the fracture and non-fracture group, the necessity for a correction for possible differences of the bone mineral density (or its surrogate BV/TV for the biopsies) and AGE between the two groups was tested.

Figures 3.1, 3.2 and 3.3 visualise and table 3.2 depicts, that BMD_{whole} and AGE did not differ significantly for the two study groups, while BV/TV_{mid} was significant.
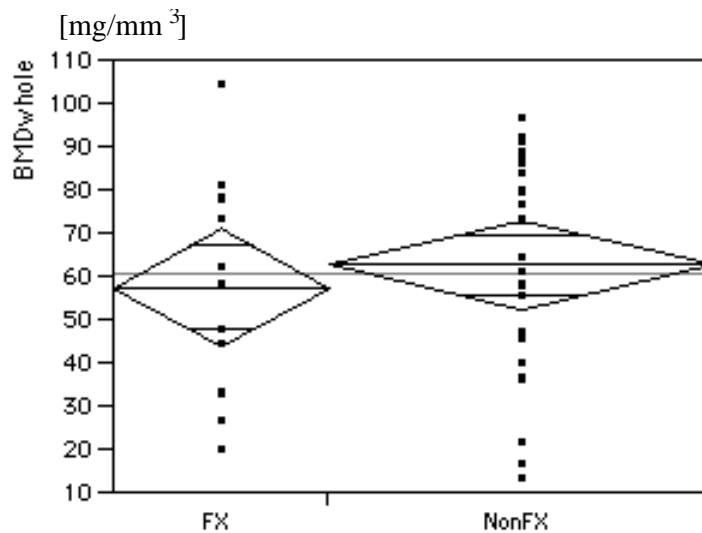
Figure 3.1: The group difference of BMD_{whole} was not significant.

	$BMD_{whole}[mgHA/ml]$	Difference
Non-FX	62.52 ± 24.98	n.s.
FX	57.46 ± 24.36	
	$BV/TV_{mid}[\%]$	
Non-FX	7.33 ± 2.2	$p < 0.02$
FX	5.49 ± 2.39	
	AGE	
Non-FX	80.68 ± 7.19	n.s.
FX	83.29 ± 6.24	

Table 3.2: Test for significant differences of BMD, BV/TV and AGE for correction.
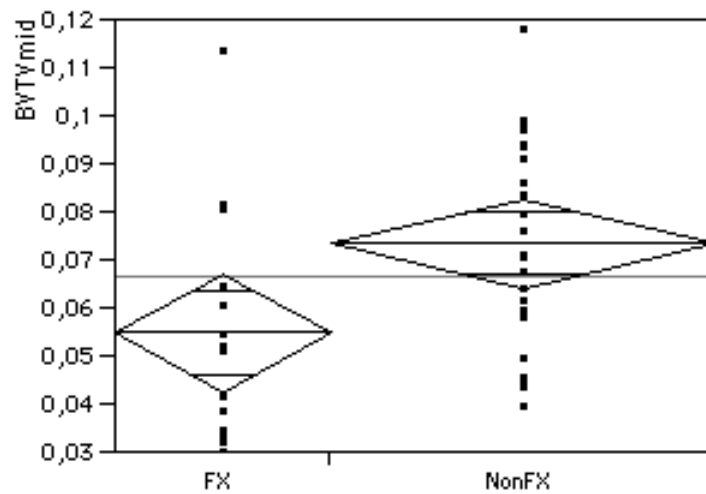
Figure 3.2: BV/TV_{mid} was significant ($p < 0.02$). The samples with the highest values for each group were investigated for criterions which may explain the high values for BV/TV but had been left in the study group since no abnormal conditions were found.
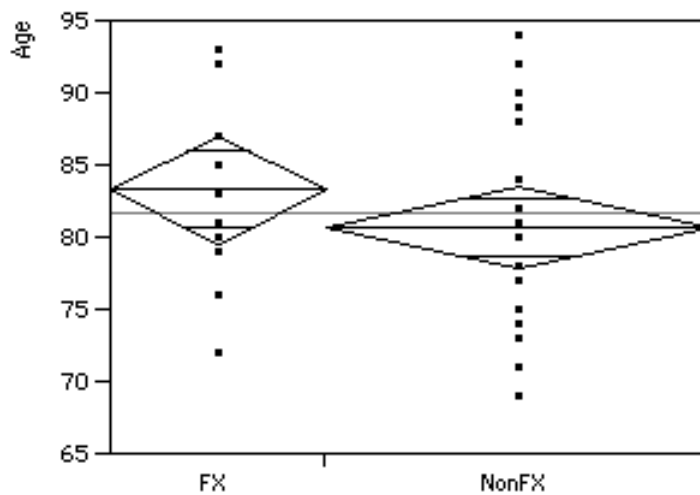
Figure 3.3: The variable AGE was not significant with respect to the groups.

3.1.2   Standard structural variables

Standard structural parameters to which Markovian structural parameters were compared to are bone volume to total volume fraction (BV/TV), trabecular number (TbN), trabec-

ular separation ($TbSp$), as well as trabecular thickness ($TbTh$). This set of variables can be computed based on two independent variables ([63]): BV/TV and one of the remaining ones, e.g. TbN. Hence, as standard structural variable set only the two independent variables BV/TV and TbN were chosen since any other would not carry any independent information. Since BV/TV already was investigated in 3.1, TbN was left only.

3.1.2.1 Normal distribution property

A Shapiro-Wilk test on TbN_{mid} did not reject the H_0 hypothesis of normal population of TbN_{mid}. Since the derived structural variables $TbTh_{mid}$ and $TbSp_{mid}$ are not investigated further due to their dependence on BV/TV_{mid} and TbN_{mid}, it was not necessary to test the normal distribution property of these two variables.

3.1.2.2 Descriptive statistics of TbN, TbTh and TbSp

The parameters of the normally distributed variables TbN_{mid}, $TbTh_{mid}$ and $TbSp_{mid}$ are given in table 3.3.

n=39, (FX=14, Non-FX=25)	Mean		StdDev
$TbN_{mid}[1/mm]$	0.79	$\pm$	0.22
$TbTh[mm]$	0.08	$\pm$	0.01
$TbSp[mm]$	1.29	$\pm$	0.43

Table 3.3: Trabecular number TbN_{mid} and the derived structural variable's distributions trabecular thickness ($TbTh_{mid}$) and trabecular separation ($TbSp_{mid}$).

3.1.2.3 Fracture discrimination of TbN

TbN_{mid} discriminated significantly between the fracture and non-fracture group (see table 3.4 and figure 3.4).

	$TbN_{mid}[1/mm]$			Difference
Non-FX	0.84	$\pm$	0.21	$p < 0.05$
FX	0.70	$\pm$	0.22	

Table 3.4: Test for significant differences of TbN_{mid}.
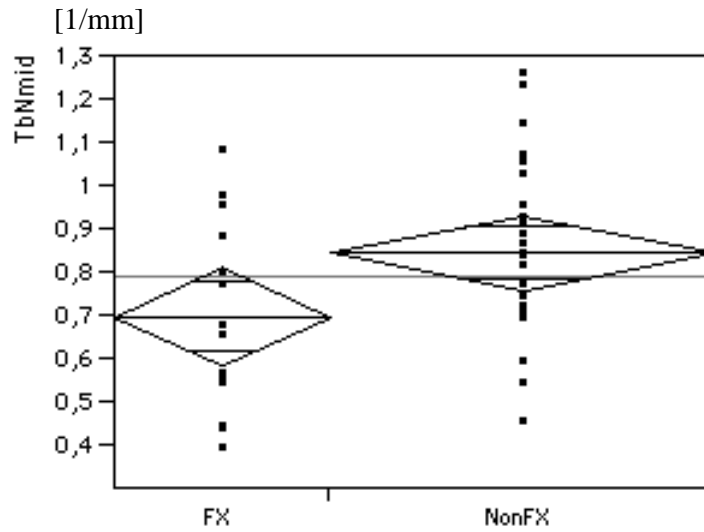
Figure 3.4: TbN_{mid} was (borderline) significantly discriminating the FX and Non-FX groups.

3.1.3   A combined model of the standard variables

BV/TV_{mid} alone explained 11.45% of the variation between the two study groups. The replacement by or the addition of any other standard structural variable did not improve the fracture discrimination. Thus, the reference value of r^2 of the standard structural variables BV/TV_{mid} the Markovian approaches were compared to was $r^2 = 11.45\%$.

r^2	BV/TV_{mid}	TbN	AGE
11.45%	*		
8.44%		(*)	
-			n.s.
-	n.s.	n.s.	
-	(*)		n.s.
-		t	n.s.

Table 3.5: Combined model of standard variables. (*: $p < 0.05$, (*): borderline-significant (as obtained by a nominal logistic fit (same parameter was significant in case of a t-test), n.s.: non significant).

3.2 The Markovian variables

In this chapter first the results of the Markov graph approach are given. Additionally, two measures based on the theory of point processes are presented: the cluster type index (CTI) and Ripley's K-function. Both Markovian variables were computed for the three-dimensional clusters of voxels which were interpreted as points of a point process. The two study groups of fractured and non-fractured vertebrae resulted in two curves for each measurement which are subsequently discussed. An additional measure based on the Markov theory is the conditional entropy. All three Markovian measures are functions of distance. Hence, for a given sample, the Markovian measurements result not in a single value as the standard structural variables do, but in a vector of values. A certain distance will be defined to map the resulting vector to a single value.

3.2.1 Node probabilities of a Markov graph

The investigation of probabilities of $11 \times 11 \times 11$ graph nodes computed on whole vertebrae resulted in 1331 consecutively numbered variables (No. 1, ..., No. 1,331). Each node referred to a voxel with a side length of $156\mu m$, thus a cube of $1.7mm^3$ was investigated. Using a multivariate model, three variables were identified out of the set of 1,331 variables which explained together 79.05% of the variablility of the two groups of vertebrae, although the single variables were not significant for this combination. The combined model of the two variables (No. 401, No. 98) was significant (see table 3.6) and explained 49.85%. Corrected for BV/TV_{mid}, the two node probabilities No. 401 and No. 98 remained significant, while BV/TV_{mid} was not. This remained true when TbN_{mid}, which was not significant in this combined model, was added to this model. Compared to the standard structural variables BV/TV_{mid} and TbN_{mid}, combined with AGE, these three factors explained together 12.05% of the variability.

Variable(s)			Discrimination
No. 401 (**)			$r^2 = 27.5\%$
No. 401 (**)	+ No. 98 (*)		$r^2 = 49.85\%$
No. 401 (n.s.)	+ No. 98 (n.s.)	+ No. 138 (n.s.)	$r^2 = 79.05\%$
No. 401 (*)	+ No. 98 (*)	+ BV/TV_{mid} (n.s.)	$r^2 = 55.94\%$
No. 401 (**)	+ No. 98 (**)	+ $TbN_{mid}(n.s.)$	$r^2 = 51.62\%$
No. 401 (**)	+ No. 98 (*)	+ AGE (n.s.)	$r^2 = 51.97\%$
BV/TV_{mid} (n.s.)	+ TbN_{mid} (n.s.)	+ AGE (n.s.)	$r^2 = 12.05\%$

Table 3.6: Discrimination of the node probabilities of the Markov graph calculated on the voxel space of the whole vertebrae.

3.2.2   Visual samples of entropy

A visual presentation of the three-dimensional high-resolution measurements is difficult, since the inner parts of the reconstruction are occluded by the outer areas, hence it is impossible to visualise a whole network without three-dimensional interaction. To allow for visual inspection 12 example biopsies were virtually cut into $1.4mm$ thick slices showing some aspects of the third dimension. Six samples were chosen showing the highest entropy (see figure 3.5) measured in the study data set, while the other six samples showed the lowest entropy (see figure 3.6).

The different topological situations found in the samples lead to the analysis of how entropy discriminated osteoporotic and healthy subjects when adjusted for the different dimensional types observed in the trabecular networks (see table 3.7). The $Entropy_{dist16}$ was found to carry independent information when significantly discriminating osteoporotic and healthy subjects after adjustment for any dimensional compartment.

$Entropy_{dist16}$	$dim1\%$	$dim2\%$	$dim3\%$
*	t		
*		n.s.	
*			n.s.

Table 3.7: The discrimination of osteoporotic and healthy subjects by $Entropy_{dist16}$ stayed significant (*) when adjusted for any of the three dimensional compartments, which themselves showed a trend (t) or were not significant (n.s.).

3.2.3   Cluster type index

The cluster type index (CTI) computed for the three-dimensional clusters of voxels is based on the point process measure J (see chapter 2.4.4.4 and is depicted in figure 3.7. All distances of the cluster type index evaluated within the range of $0 - 0.7mm$ showed either a significant difference or a trend between the samples of the fractured and non-fractured group. The three highest explanations of variation were found for distances of $0.3mm - 0.4mm$ (12 pixel/$0.3mm, r^2 = 20.9\%$, 14 pixel/$0.35mm, r^2 = 24.9\%$ and 16 pixel/$0.4mm, r^2 = 19.2\%$).

The outcome of the CTI_{dist16} parameter was compared to the reference process, which is a Poisson process with constant value of 1 for any distance. A value lower than one corresponds to a clustered pattern, a value above one represents an inhibited and thus regular pattern. The reference Poisson process, which is constantly one, can be regarded as neutral process showing no clustering nor inhibition pattern.
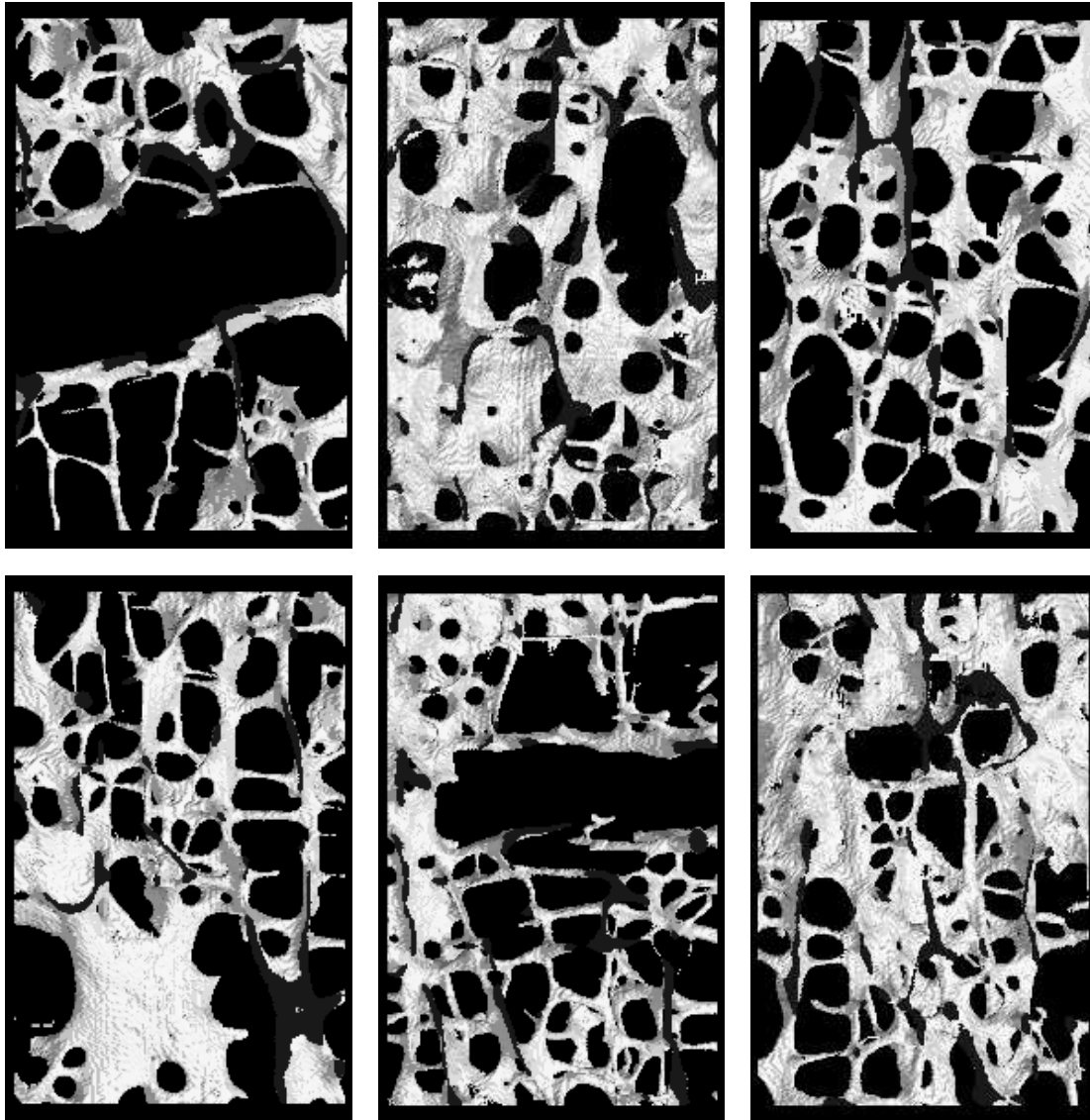
Figure 3.5: Six samples of thickness 1.4 mm showing the highest entropy of the sample set.

The non-fractured samples resulted in values of CTI_{Dist16} above 1 and above the values computed from the fractured samples. The results of the fractured samples first show a drift over 1 (maximum of means: 1.02 at distance $0.15mm$), crosses the value 1 around distance $0.35mm$ and sinks below 1 (minimum of means: 0.98 at $0.55mm$ distance).

The deviation of the non-fractured samples from the reference value 1.0 is 1.4% higher than the deviation of the fractured group at distance $0.15mm$. At a distance $0.55mm$ the deviation from the value of 1.0 is 444.3% higher for the non-fractured samples than for
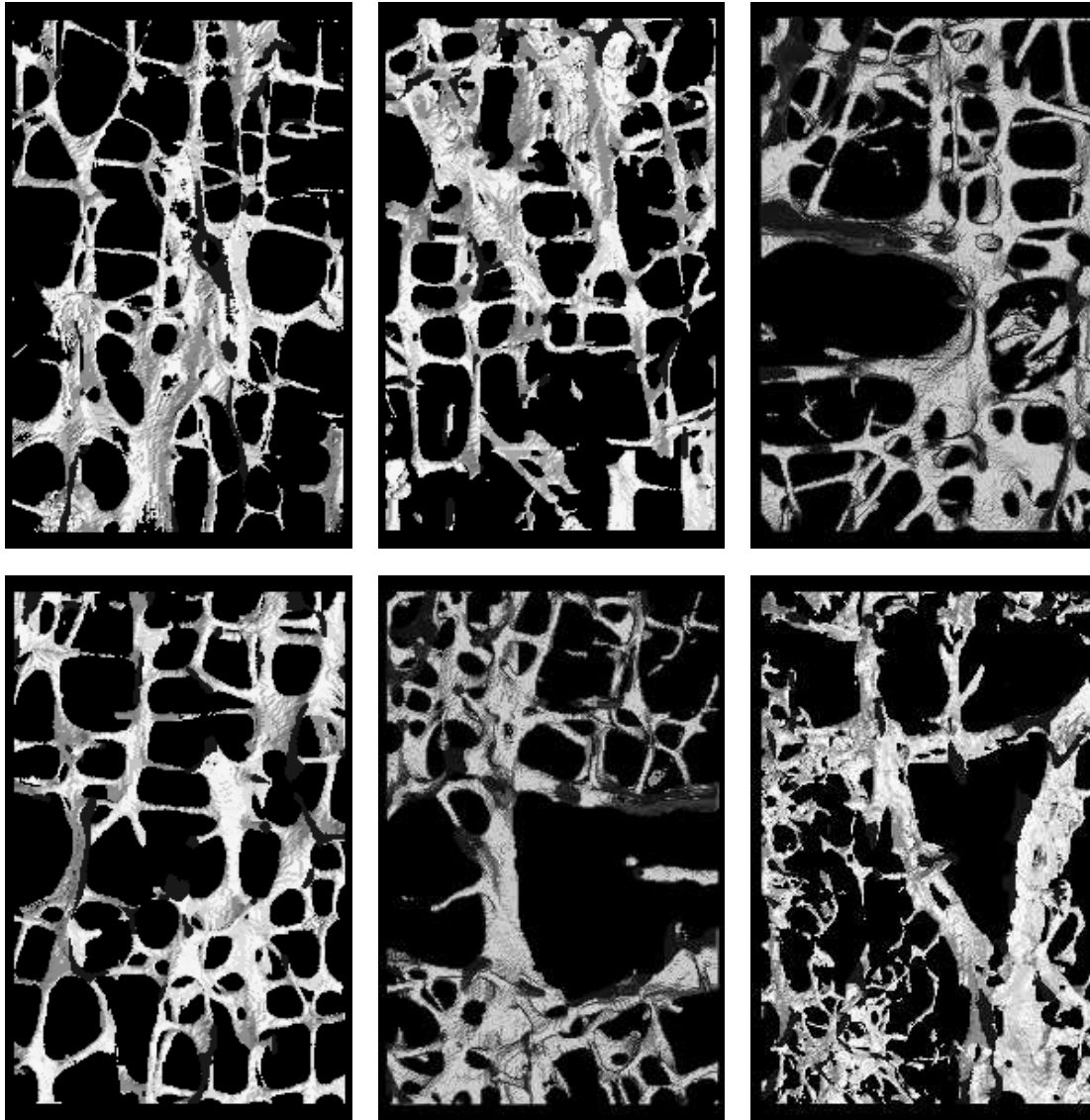
Figure 3.6: Six samples of thickness 1.4 mm showing the lowest entropy of the sample set.

the fractured ones and thus reflects a regular or inhibited pattern for the non-fractured group.

Although the results of the fractured samples were above 1 for distances below $0.35mm$ and below 1 for distances beyond $0.35mm$, the deviation was below 0.2 for the means for all distances. Thus, the underlying pattern type is comparable to the Poisson process and thus shows no clustering nor inhibition but a random pattern.
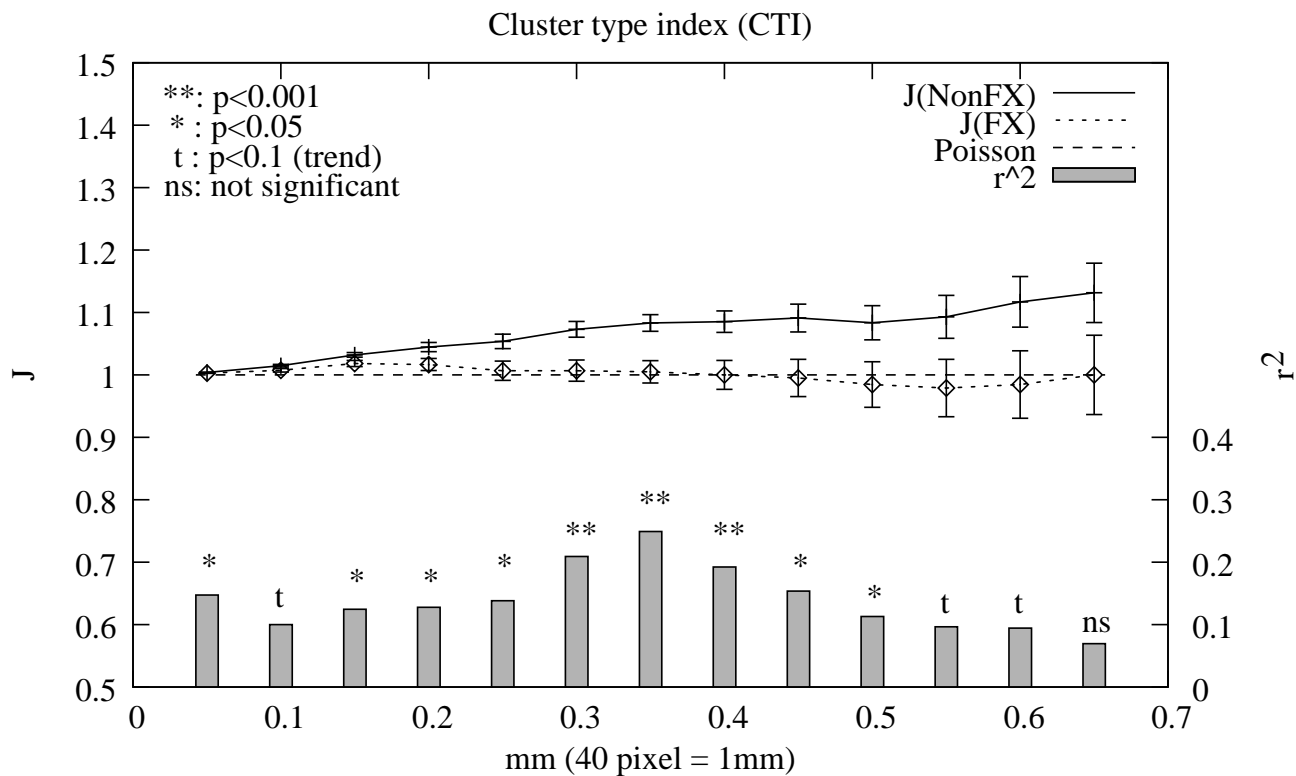
Figure 3.7: Cluster type index as a function of distance (intervals shown are standard errors).

3.2.4   Ripley's K-function
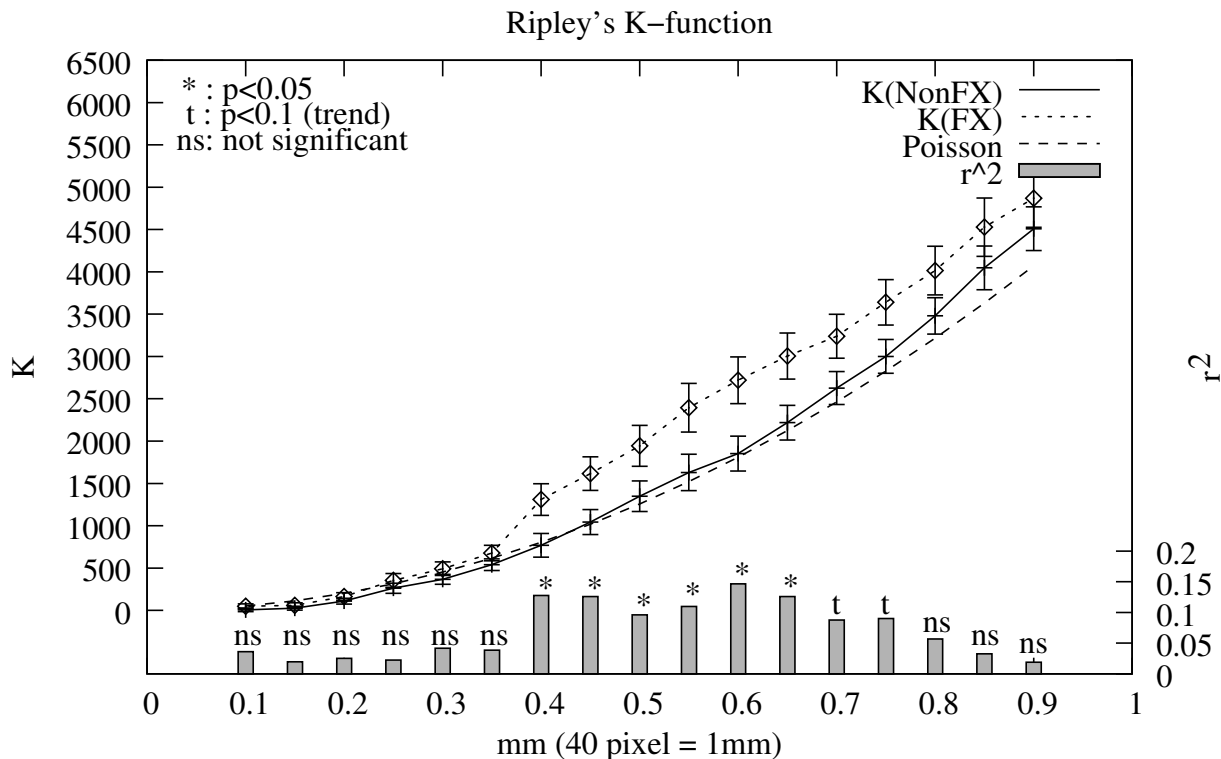
Figure 3.8: Ripley's K-function as an estimate of the expected number of points within a certain distance (intervals shown are standard errors).

The curves of the Ripley's K-function with respect to the two study groups FX and Non-FX as well as a Poisson reference curve are given in figure 3.8. Significant differences between values for K_{FX} and K_{Non-FX} were observed for distances between 16 and 26 pixels ($400\mu m - 650\mu m$).

The highest explanation for variations of the K-values was found at a distance of 17 ($400\mu m$) with a r^2 of 0.15. Within the interval $400\mu m - 700\mu m$ of significant distances of K_{FX} and K_{Non-FX} r^2-values between 0.09 and 0.15 were found.

The K-function showed two qualitatively different behaviours in terms of the difference $K_{FX} - K_{Non-FX}$: Within the interval of $0 - 14$ pixel ($0 - 375\mu m$) the difference $K_{FX} - K_{Non-FX}$ was significantly lower ($p < 0.001, r^2 = 92.4\%$) than for values within the interval of $17 - 35$ pixel ($425 - 875\mu m$).

The results of $Ripley's\ K_{dist16}$ for significant distances between $400\mu m - 650\mu m$ indicate a higher expectation value for the existence of three-dimensional voxel clusters in fractured

samples than for non-fractured ones for a given distance of the aforementioned range.

For distances below $0.4mm$ no significantly higher expectation value for the number of three-dimensional clusters was observed.

3.2.5 Conditional entropy
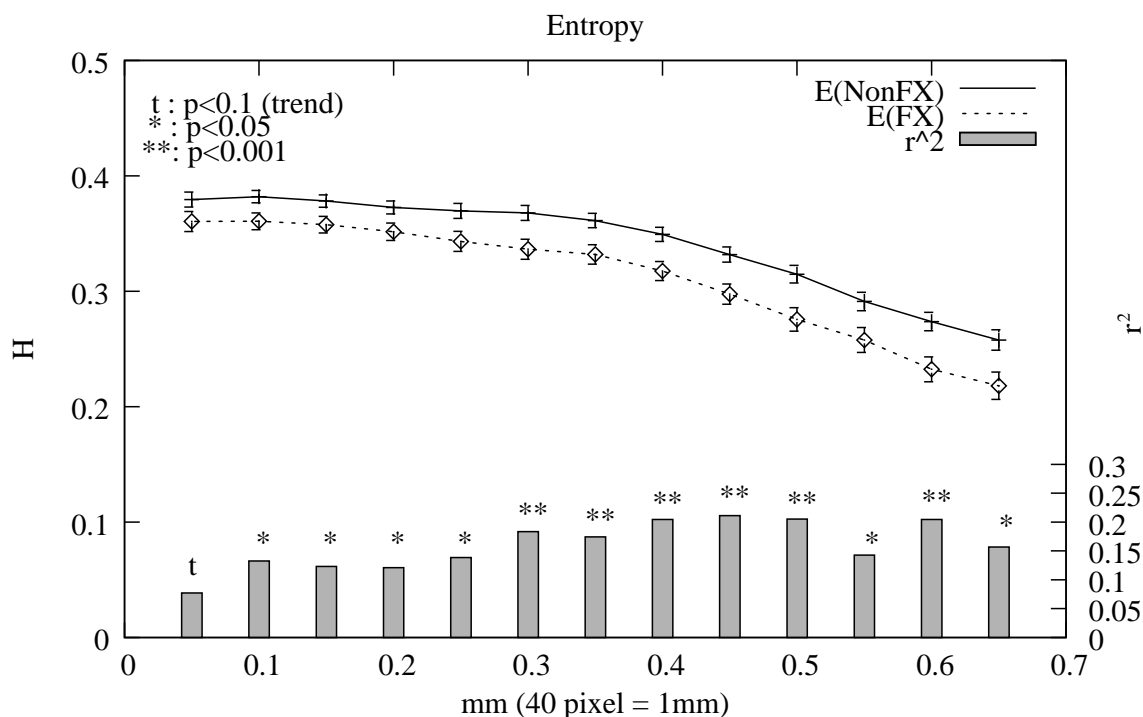
Figure 3.9: The conditional entropy as a function of distance (intervals shown are standard errors).

All distances starting with $0.1mm$ evaluated with the conditional entropy showed significant distances. The highest values for r^2 were found within the interval of $0.3 - 0.6mm$ (figure 3.9). For distances of 16 to 20 pixels r^2 was higher than 20%.

The continuous sequence of significantly higher values were observed for non-fractured samples. Since a higher amount of entropy is equivalent to a higher amount of uncertainty for the process of expanding structures, the prediction of the trabecular network of non-fractured samples was more difficult than the prediction for fractured trabecular networks.

In other words, the variety of trabecular networks within the fracture group is lower than the variety within the non-fracture group.

3.2.6   A mapping of Markovian vectors to a single measurement

The three Markovian variables map a sample to a function of distance (see figures 3.7, 3.8 and 3.9), i.e.

$$CTI, Ripley's\ K, Entropy: \quad FX \cup Non\text{-}FX \mapsto (\mathbb{R} \mapsto \mathbb{R})$$

Based on the results of sections 3.2.3, 3.2.4 and 3.2.5 the question was investigated if the developing of values shares some common characteristics between the three Markovian variables. The aim was to establish a fixed distance for all three variables to enable a restriction of the vector of measurement results to one value.

Considering the intervals showing the highest explanation of variation for the three Markovian variables, a restriction of the Markovian functions CTI, $Ripley's\ K$ and $Entropy$ for a given sample was established by choosing the fixed distance d=$0.4mm$ (16 pixels).

As a result, the mapping given by the Markovian variables from a sample $s \in FX \cup Non\text{-}FX$ simplifies to:

$$CTI_{dist16}, Ripley's\ K_{dist16}, Entropy_{dist16}: \quad FX \cup Non\text{-}FX \mapsto \mathbb{R}$$

See figures 3.10, 3.11, and 3.12 for the resulting Markovian variables fixed for a distance of 16.

3.2.7   Normal distribution property

The Shapiro-Wilk test on both the cluster type index as well as the entropy variable did not reject the H_0 hypothesis of normal population in any of these cases.

The same test performed on $Ripley's\ K_{dist16}$ did reject the H_0 hypothesis of normal population with a high level of significance of $p < 0.0001$. An investigation of the distribution resulted in the identification of a single subject showing a value for $Ripley's\ K_{dist16}$ of 4791. Although the result of $Ripley's\ K_{dist16}$ for this subject was more than twice as the highest value of the other subjects, a visual inspection of the dataset did not explain this outlier. No consistent extremal results for the other variables of this subject were observed. However, the distribution of $Ripley's\ K_{dist16}$-function is normally distributed. This was confirmed by a new Shapiro-Wilk test on $Ripley's\ K_{dist16}$-function without this single subject which this time did not reject the H_0 hypothesis of a normal population ($p < 0.38$).
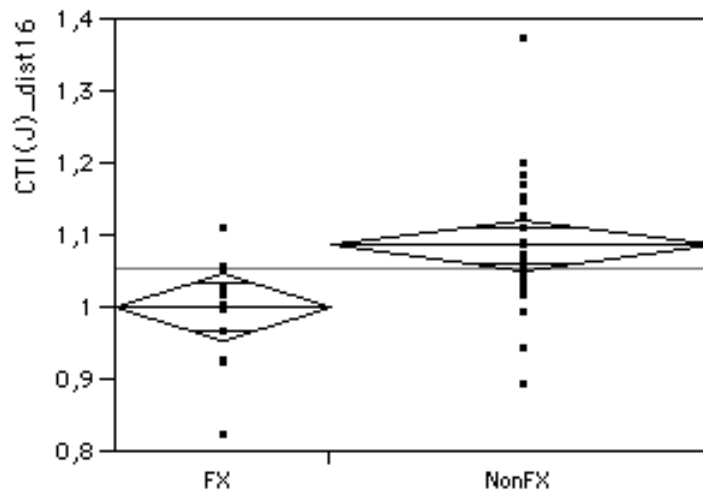
Figure 3.10: The CTI_{dist16}-function discriminated significantly ($p < 0.01$).
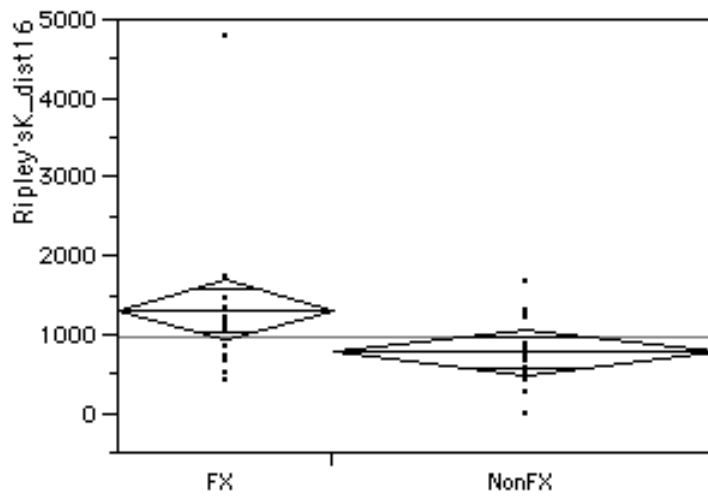
Figure 3.11: The $Ripley's\ K_{dist16}$-function discriminated significantly ($p < 0.05$).

Beyond the absolute value for the subject discussed, no reason was found which would result in an exclusion. Thus, the value was not excluded. A hypothetical exclusion would not have changed the level of significance for the discrimination for this parameter (with value discussed: $p < 0.0459$, without $p < 0.0474$).
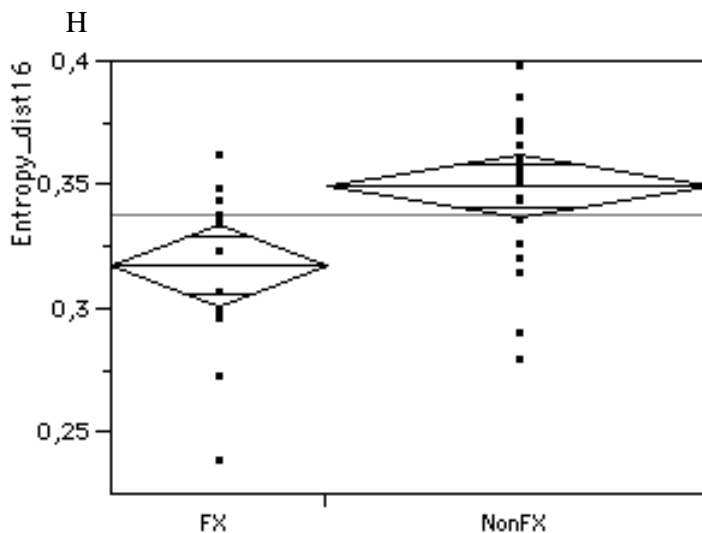
Figure 3.12: The $Entropy_{dist16}$-function discriminated significantly ($p < 0.01$).

3.3 Standard and Markov variables combined

After having investigated the standard as well as Markov variables each on its own, some questions arose when considering a combined model: Is there redundancy between any of the variables? Or is there an independent contribution to either explanation of the group differences between osteoporotic and healthy subjects or the explanation of failure load? The degree of redundancy was investigated in terms of correlations between the variables, while any independent contribution to the tasks of discrimination and explanation was determined by a nominal logistic fit, presented in the next sections.

3.3.1 Investigating redundancy

To investigate the question if there exist close relationships between variables which would allow to use one structural concept as a surrogate for another concept, the correlations between the measures of this study were determined (see table 3.8 and figure 3.13).

Beside the only strong correlation between BV/TV_{mid} and TbN_{mid}, the remaining correlations were moderate or weak. Especially between the standard and Markovian variables all correlations which were found to be significant lay in a range of ($|0.33| < r < |0.53|$). The correlations between the Markovian variables were found to be weak, too (range ($|0.28| < r < |0.5|$)[1]).

---

[1]Instead of r^2 here r was used to simplify the grading of the correlation into strong/moderate/weak.

r	BV/TV_{mid}	TbN_{mid}	AGE	$Entropy_{dist16}$	CTI_{dist16}
BV/TV_{mid}	–				
TbN_{mid}	0.92 (***)	–			
AGE	−0.40 (*)	−0.43 (**)	–		
$Entropy_{dist16}$	0.24 (n.s.)	0.24 (n.s.)	−0.38 (*)	–	
CTI_{dist16}	0.53 (***)	0.49 (**)	−0.4 (*)	0.28 (t)	–
$Ripley's\ K_{dist16}$	−0.4 (*)	−0.33 (*)	0.42 (**)	−0.5 (**)	−0.4 (*)

Table 3.8: Pairwise correlations listing the square of the Pearson product-moment correlations (cross correlations) to reveal possible redundancy of the variable set. Note the use of r instead of r^2 here.

3.3.2 A combined model of standard and Markovian variables

In order to determine if the explanation of variation between the fracture and non-fracture group can be increased by adding the Markovian variables $Entropy_{dist16}$, CTI_{dist16} and $Ripley'sK_{dist16}$ to a combined model of the standard variables BV/TV_{mid}, TbN_{mid}, a nominal logistic fit was calculated out of these variables. The models calculated are given in table 3.9.

While the reference variable BV/TV_{mid} alone explained 11.45% of the variation between the two study groups, TbN_{mid} alone explained 8.44%. When combined, these two variables did not stay significant.

The Markov-based variables alone explained between 12.95% ($Ripley'sK_{mid}$, borderline-significant), 16.65% ($Entropy_{dist16}$) and 18.34% (CTI_{dist16}). The most successful combination found was a combined model between CTI_{dist16} and $Entropy_{dist16}$ explaining together 33.67%. Any reference parameter added to the model was not significant any more. BV/TV_{mid} combined with $Entropy_{dist16}$ only built a model with both parameters being significant, but explaining only 25.38% of the variatioin.

Hence, for fracture discrimination the best combination consisted only of Markov variables and was the AGE-adjusted combined model CTI_{dist16} and $Entropy_{dist16}$.

3.3.3 Explanation of failure load

For the vertebral segment T9,T10,T11 neighboured to the T12 study samples investigated in this study the failure load from a different study were known. Hence, the correlation between the main variables of this study and the T9-T11 failure load were determined. AGE itself correlated significantly ($p < 0.05$) with the failure load and explained 10.7%. In table 3.10 the correlation as well as combined models are listed. The variation of the
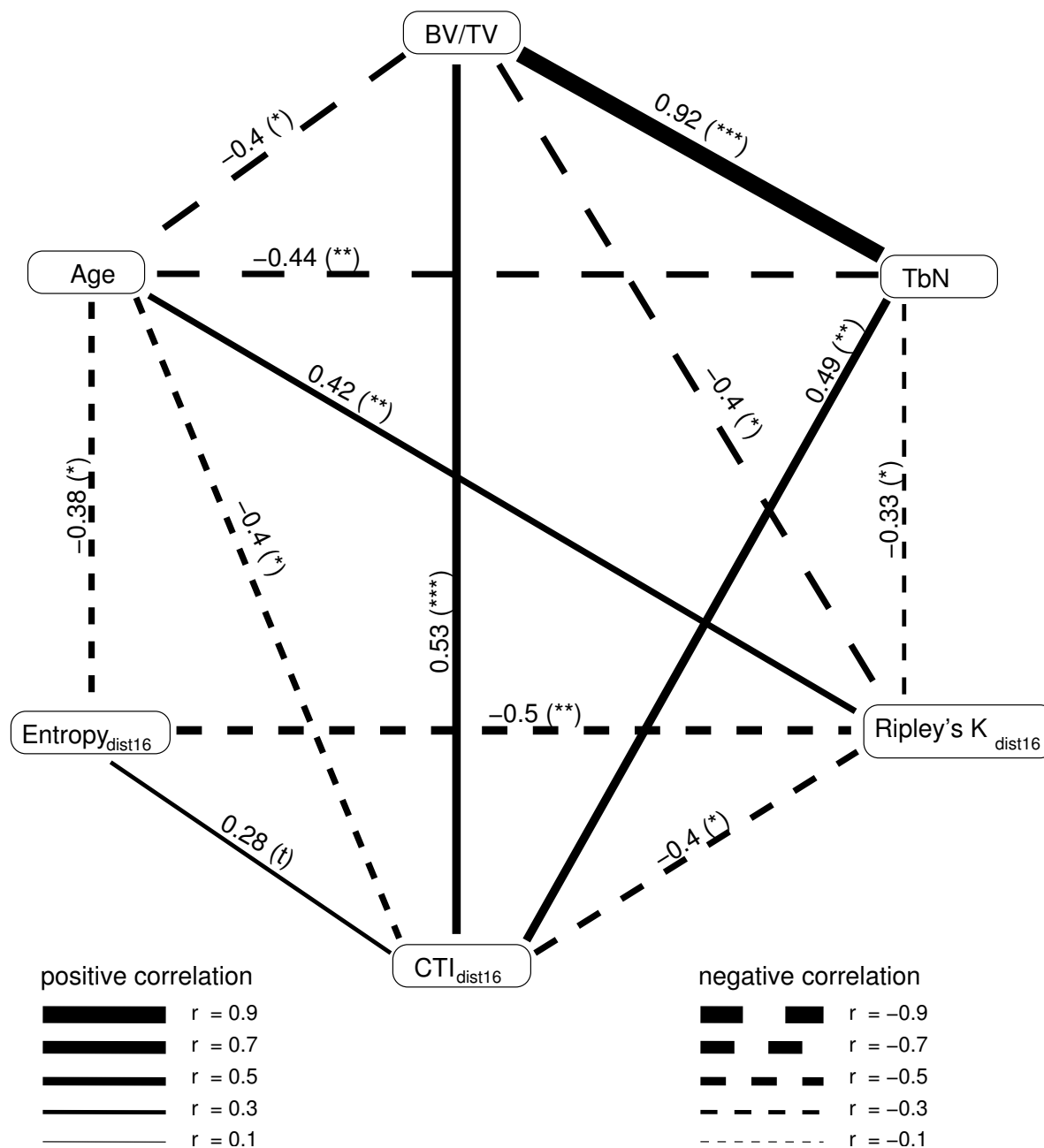
Figure 3.13: Graph visualising the pairwise correlation coefficients (r) of table 3.8 (missing connections represent non-significant correlations).

failure load of T9-T11 was explained best by BV/TV_{mid} with 35% (36% after adjusting for age). When combining with entropy, the model ($AGE+BV/TV_{mid}+Entropy_{dist16}$)

r^2	BV/TV_{mid}	TbN	CTI_{dist16}	$Ripley'sK_{dist16}$	$Entropy_{dist16}$
11.45%	*				
8.44%		*			
-	n.s.	n.s.			
18.32%			*		
12.94%				*	
16.55%					*
adjusted for AGE					
11.53%	(*)				
8.64%		t			
18.34%			*		
12.94%				(*)	
16.65%					*
adjusted for AGE + combinations					
-			*	n.s.	*
33.67%			*		*****
-	n.s.		*		*
-		n.s.	*		*
-		t			*
25.38%	(*)				*
-	n.s.		*		

Table 3.9: Estimation of the gain of explanation of the variation by adding Markovian variables to the standard set of structural variables (r^2: combined model of contributors listed in the same line, *: $p < 0.05$, (*): borderline-significant, t: trend, n.s.: non significant). All nominal logistic fit models.

explained 43.1%, which is a gain of 8.1%.

3.4   Risk estimation by standardised odds ratios

An estimate of the magnitude of change of risk was calculated on the basis of odds ratios for the structural variables. The odds ratios as well as the 95% confidence intervals are listed in table 3.11. The uncorrected odds ratios which can be found in the upper part of the table lists three significant odd variables: BV/TV_{mid}, $Entropy_{dist16}$ as well as CTI_{dist16}. After correcting the two significant Markovian variables for BV/TV_{mid} the $Entropy_{dist16}$ remained significant, while the CTI_{dist16} lost its significance.

r^2	BV/TV_{mid}	TbN_{mid}	$dim1\%$	$Entropy_{dist16}$	CTI_{dist16}	$Ripley'sK_{dist16}$
35.0%	***					
33.0%		***				
35.9%			***			
17.2%				**		
10.4%					*	
12.0%						*
adjusted for AGE						
36.0%	***					
34.2%		***				
37.2%			***			
20.6%				**		
					t	
						t
adjusted for AGE + combinations						
	n.s.	n.s.				
(40.4%)	t		t			
(41.5%)			**	t		
43.1%	***			*		

Table 3.10: Correlation of the failure load of the segment T9,T10,T11 with main variables of this study. The highest explanation of variation of the failure load T9-T11 was given by the combined model of $(AGE+BV/TV_{mid}+Entropy_{dist16})$. (The correlations of BV/TV_{mid} with TbN_{mid} $(r^2 = 84.9\%)$ and BV/TV_{mid} with $dim1\%$ $(r^2 = 60.9\%)$ both were strong and highly significant).

3.5 Testing for subgroups

As long as the results obtained in this study are not validated by another independent investigation, the general validity and the independency of the results from the study groups chosen are not proven. One possibility to estimate the variance of the possible results inherent in the sample group is to use further tests on subgroups of the study population. Two kinds of subgroup investigations are used in this study: the first approach used in section 3.5.1 divides each of the two study groups S_{FX} and S_{Non-FX} into two subgroups S_{FX}^1, S_{FX}^2 and $S_{Non-FX}^1, S_{Non-FX}^2$ with $S_{FX}^1 \oplus S_{FX}^2 = S_{FX}$, $S_{Non-FX}^1 \oplus S_{Non-FX}^2 = S_{Non-FX}$. This division is repeated in a fashion to produce several subgroups with maximal variability or, in other words, a minimised overlap of samples between the subgroups. The second approach (section 3.5.2) determines the smallest possible subgroups while maximising the number of subgroups by using sets containing only one element. The fracture

Odds Ratios	StdErr	Stddev	beta	sOR	(-2SE)	(+ 2SE)	csOR
BMD_{whole}	0.014	24.558	-0.009	0.810	0.411	1.596	1.235
BV/TV_{mid}	17.336	0.024	-37.967	**0.401**	**0.174**	**0.924**	**2.495**
TbN_{mid}	1.782	0.222	-3.430	0.467	0.212	1.030	2.141
$Entropy_{dist16}$	12.958	0.034	-32.620	**0.329**	**0.136**	**0.796**	**3.040**
CTI_{dist16}	6.113	0.095	-14.881	**0.244**	**0.077**	**0.778**	**4.095**
$Ripley's\ K_{dist16}$	0.001	736.373	0.002	4.407	0.997	19.481	4.407
significant variables adjusted for AGE:							
$BVTV_{mid}$	17.336	0.024	-36.563	**0.415**	**0.180**	**0.956**	**2.412**
$Entropy_{dist16}$	12.958	0.034	-32.018	**0.336**	**0.139**	**0.812**	**2.979**
CTI_{dist16}	6.113	0.095	-14.741	**0.247**	**0.078**	**0.788**	**4.042**
significant variables adjusted for AGE and $BVTV_{mid}$							
$Entropy_{dist16}$	15.169	0.034	-33.258	0.322	**0.114**	**0.905**	**3.107**
CTI_{dist16}	6.426	0.095	-12.528	0.305	0.090	1.031	3.277

Table 3.11: Standardised odds ratios per standard deviation change. Significant odds ratios are printed bold. The upper part shows uncorrected odds ratios, the lower part shows odds ratios of significant variables from the upper part corrected for BV/TV_{mid} (TbN_{mid} was not significant for odds ratios). Beta: beta-parameter of Nominal Logistic fit, sOR: standardised odds ratio, 2SE: two standard deviations from sOR (sOR $\pm$ 2 $\times$ SE), csOR: beta$<0 \rightarrow$ csOR $= 1/$sOR, otherwise csOR $=$ sOR (Numbers shown are rounded, calculations were performed with full precision provided by the nominal logistic fit model).

discrimination of such one-element sets is directly estimated by calculating the difference of the structural variables between an element taken from the FX group and an element taken from the Non-FX group.

3.5.1   Sets of two subgroups

The first investigation of subgroups used tuples of subsets taken from both study groups, the fracture group S_{FX} and the non fracture group S_{Non-FX}. Since the fracture group consists of only 14 samples and the non fracture group holds 25 samples, a first generation of subgroup tuples contained 7 samples from the FX- and 12/13 samples from the Non-FX subgroups chosen randomly. To obtain a high variability between the subgroups, the second tuple of subsets composed from the first two subsets was obtained by interchanging half of the elements of the subgroups. This ensured a minimal overlap between the first tuple of subgroups and the second one built from the first tuple. This procedure was repeated according to figure 3.14 and generated eight tuples of subgroups. While the whole study group was named *group 1*, the eight subgroups are entitled *subgroup 2, ..., subgroup 9*.

Generation	Splitting scheme		Group number
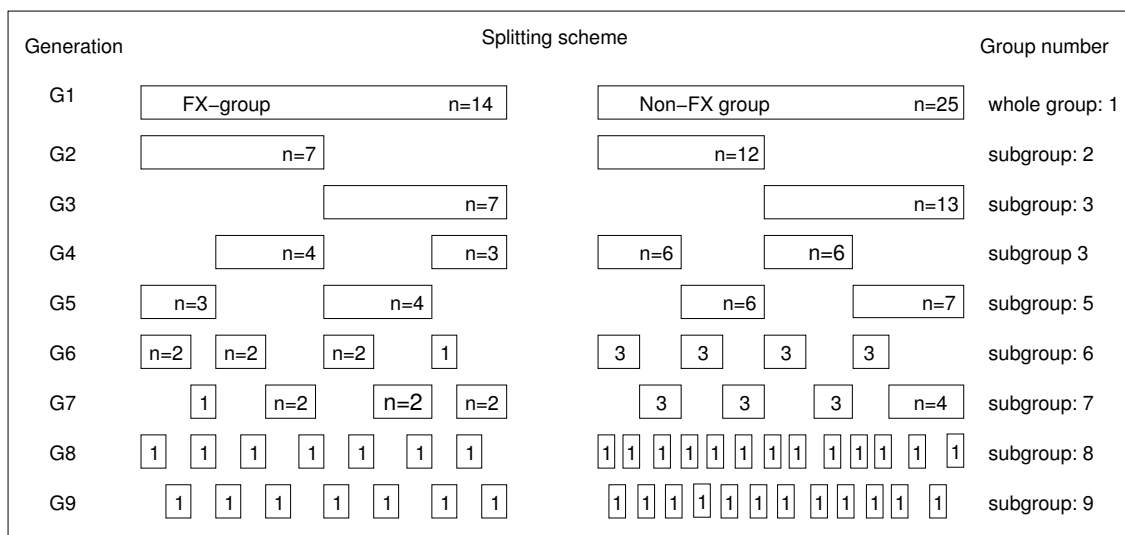
Figure 3.14: Splitting scheme to obtain 8 tuples of subgroups from the two study groups.

3.5.1.1   Nominal logistic fit

First, the nominal logistic fit was recalculated for the node probabilities of the Markov graph based on the eight subgroups built according to scheme 3.14. Table 3.12 lists the values for r^2 which were computed for the subgroups:

Group	Variables		r^2
1 (all)	No. 401 (**) + No. 98 (*)		49.85%
Subgroup			
2	No. 401 (*) + No. 98 (t)		39.54%
3	unstable estimation		
4	No. 401 (*) + No. 98 (*)		49.76%
5	No. 401 (t) + No. 98 (t)		50.59%
6	No. 401 (*) + No. 98 (t)		45.43%
7	No. 401 (t) + No. 98 (t)		56.42%
8	No. 401 (*) + No. 98 (t)		41.28%
9	No. 401 (t) + No. 98 (t)		63.23%

Table 3.12: Multivariate model of subset of best variables of node probabilities of Markov graphs, computed for subgroups.

3.5.1.2 t-test

To get a visual impression of the distributions of the structural parameters of both the standard and the Markovian type, the two-tailed analysis of variances is depicted in figure 3.15 for the standard variables and in figure 3.16 for the Markovian variables.

3.5.2 Differences of any two values

The smallest possible subgroup contains only one element. Hence, the set of differences between any two members of the two study groups S^{FX} and S^{Non-FX} is investigated. For a structural variable V (i.e. BV/TV, TbN, etc) a histogram over all possible tuples $S_{Diff}\{V(s_i^{FX} - s_j^{Non-FX})|s_i^{FX} \in S^{FX}, s_j^{Non-FX}, i,j \in \mathbb{N}\}$ was built. The cardinality $|S_{Diff}|$ was $14 \times 25 = 350$.

The histogram of a totally random variable would result in a Gaussian distribution showing a median of 0. The zero-value percentiles are listed in table 3.13.

Variable	Zero-value-percentile
BV/TV_{mid}	80.4%
TbN_{mid}	77.4%
AGE	66.7%
$Entropy_{dist16}$	87%
CTI_{dist16}	89.3%
$Ripley's~K_{dist16}$	87.2%

Table 3.13: Zero-value-percentiles: The number of positive differences between any two variables out of the fracture (14 cases) and non-fracture group (25 cases). A totally random variable results in approximately 175 out of 350 (14x25) positive differences (50%).

3.6 Dimensional network composition

As described in section 2.4.5.2.3, the calculation of the local dimension included the determination of each voxels affiliation to trabeculae of dimension one (rods), two (plates) and three (junctions). Knowing the dimension assigned to each voxel, the dimensional composition of each trabecular network was obtained, given by the triple (percentage of one dimensional voxel, percentage of two dimensional voxels, percentage of three dimensional voxels).

The dimensional composition of the trabecular networks of the study population was on average: 4.46% of dimension 1 ($\pm$2.17%), 49.99% of dimension 2 ($\pm$10.56%) and 45.56% of dimension 3 ($\pm$11.85%). The study group dependent composition is listed in table 3.14.

	dim 1[%]	dim 2[%]	dim 3[%]
Non-FX	3,84	49,44	46,72
FX	5,57	50,97	43,46
Diff	1,73	1,53	-3,26

Table 3.14: Dimensional composition of bone voxels.

3.6.1   Fracture discrimination

The fraction of voxels determined as one-dimensional discriminated significantly between the fractured and non-fractured samples ($p < 0.01, r^2 = 15.1\%$), independent of BV/TV. The portion of two and three-dimensional voxels, given in percent, did not discriminate significantly.

3.6.2   Correlation to structural variables

This part of the study investigated the correlations between both the standard and Markovian structural variables and the local dimensions of one, two and three. A moderate correlation was found between BV/TV_{mid} and a local dimension of one. All other correlations for dimension one listed in table 3.15 were weak, although significant. Dimension two showed a weak correlation to BV/TV_{mid}, too and a trend to $Ripley's K_{dist16}$. The same was true for dimension three, which showed additionally a trend to TbN_{mid}.

$r^2[\%]$	$dim1\%$	$dim2\%$	$dim3\%$
BV/TV_{mid}	60.9 (***)	14.4 (*)	23.1 (***)
TbN_{mid}	51.0 (***)	n.s.	6.7 (t)
AGE	13.3 (*)	n.s.	n.s.
$Entropy_{dist16}$	10.9 (*)	n.s.	n.s.
CTI_{dist16}	11.9 (*)	n.s.	n.s.
$Ripley's K_{dist16}$	15.0 (*)	6.9 (t)	9.3 (t)

Table 3.15: Correlation of the proportion of each dimension found in the networks with the structural variables.

3.7 Results in an overview

In table 3.16 a summarise of results is given including discrimination between the two study groups, the odds ratio as well as the correlation of the variables with failure load. An adjustment for AGE and BV/TV_{mid} was performed and listed for the variables remaining significant.

3.8 HMM-based detection of trabeculae - Proof of concept

A first classification of bone induced and noise induced peaks can be viewed in the figures: 3.17 (HRCT image), 3.19 (location of noise peaks), 3.18 (location of bone peaks).

As a phantom with known structure was not available to determine the ground truth, evidences for the correctness of the classification were collected. First, the specificity and sensitivity were evaluated as given in table 3.17 to 99.0% and 34.9%, respectively.

Within four different independent in vitro HRCT scans of the same vertebra and four subsequent applications of the HMM approach, the coefficient of variance of the number of structures classified as bone was calculated as 13.8%.

			$BVTV_{mid}$		Discrimination FX/Non-FX			Failure load	
Variable	Interpretation	Dim.	Corr. (r^2)	Sign.	sOR(Conf.Int.)	r^2	Sign.	Corr. (r^2)	Sign.
BMD_{whole}	bone mineral density	(3D)	36.8%	***	n.s.	n.s.	-	26.1%	***
AGE	age of donors	(1D)	-16.0%	*	n.s.	n.s.	-	10.7%	*
$BVTV_{mid}$	bone volume over total volume	(3D)	-	-	2.50 (1.08, 5.74)	11.5%	*	35.0%	***
TbN_{mid}	trabecular number	(3D)	84.8%	***	n.s.	8.44%	*	33.0%	***
$Entropy_{dist16}$	predictability of pattern extensions	(3D)	-	n.s.	3.04 (1.26, 7.36)	16.6%	*	17.2%	**
$Entropy_{dist16}$	adjusted for $AGE+BVTV_{mid}$ ($BVTV_{mid}$ remained sign.)				3.32 (1.18, 9.33)	25.4%	*	43.1%	*
CTI_{dist16}	clustered versus regular pattern	(2D)	28.5%	***	4.10 (1.29, 13.04)	18.3%	*	10.4%	*
CTI_{dist16}	adjusted for $AGE+BVTV_{mid}$ ($BVTV_{mid}$ was not sign.)				n.s.	-	*	-	n.s.
$Ripley'sK_{dist16}$	expected gain of points of pattern extensions	(2D)	16.0%	*	n.s.	12.9%	*	12.0%	*
$Entropy_{dist16}$ $+ CTI_{dist16}$	adjusted for AGE, both variables discriminated significantly (*)				-	33.7%	*	-	-

Table 3.16: Summarising table listing the most important results of this study in one table. (non significant: n.s., $p < 0.05 : *$, $p < 0.01 : **$, $p < 0.001 : ***$)

	Inside	Outside
Bone	279	8
Other	521	759

Table 3.17: Estimating specificity (99.0%) and sensitivity (34.9%) of the classification (normalised for the area outside and inside the vertebrae (2:1). χ^2-Test: $p < 0.0001$.

Sample	A	B	C	D
Number of structures	39	107	103	151
BMD	46	70	101	183

Table 3.18: A comparison of the number of structures detected and the bone mineral density known for the subjects (in vitro).
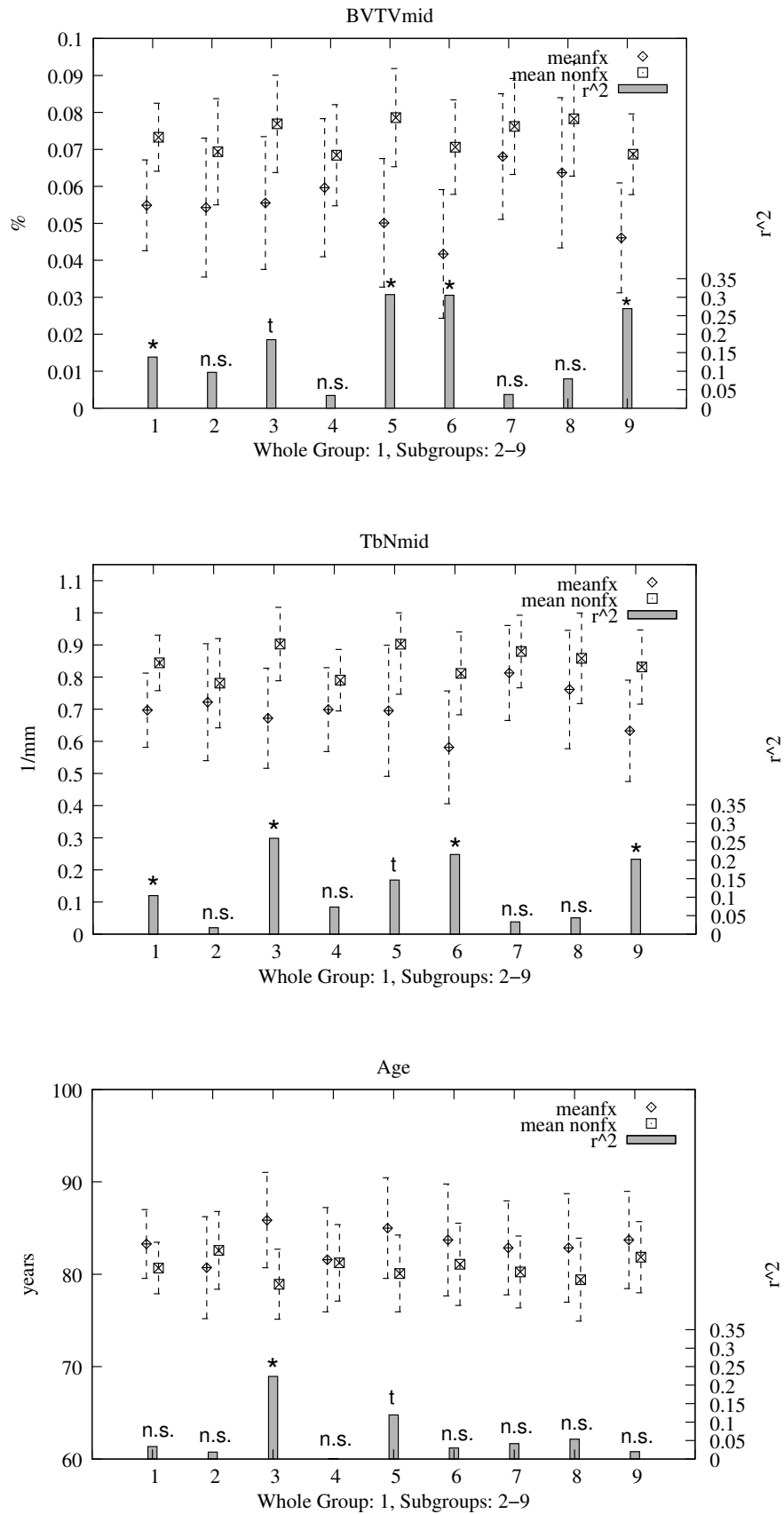
Figure 3.15: Repeated fracture discrimination of each standard variable: original complete group: 1, subgroups 2-9.
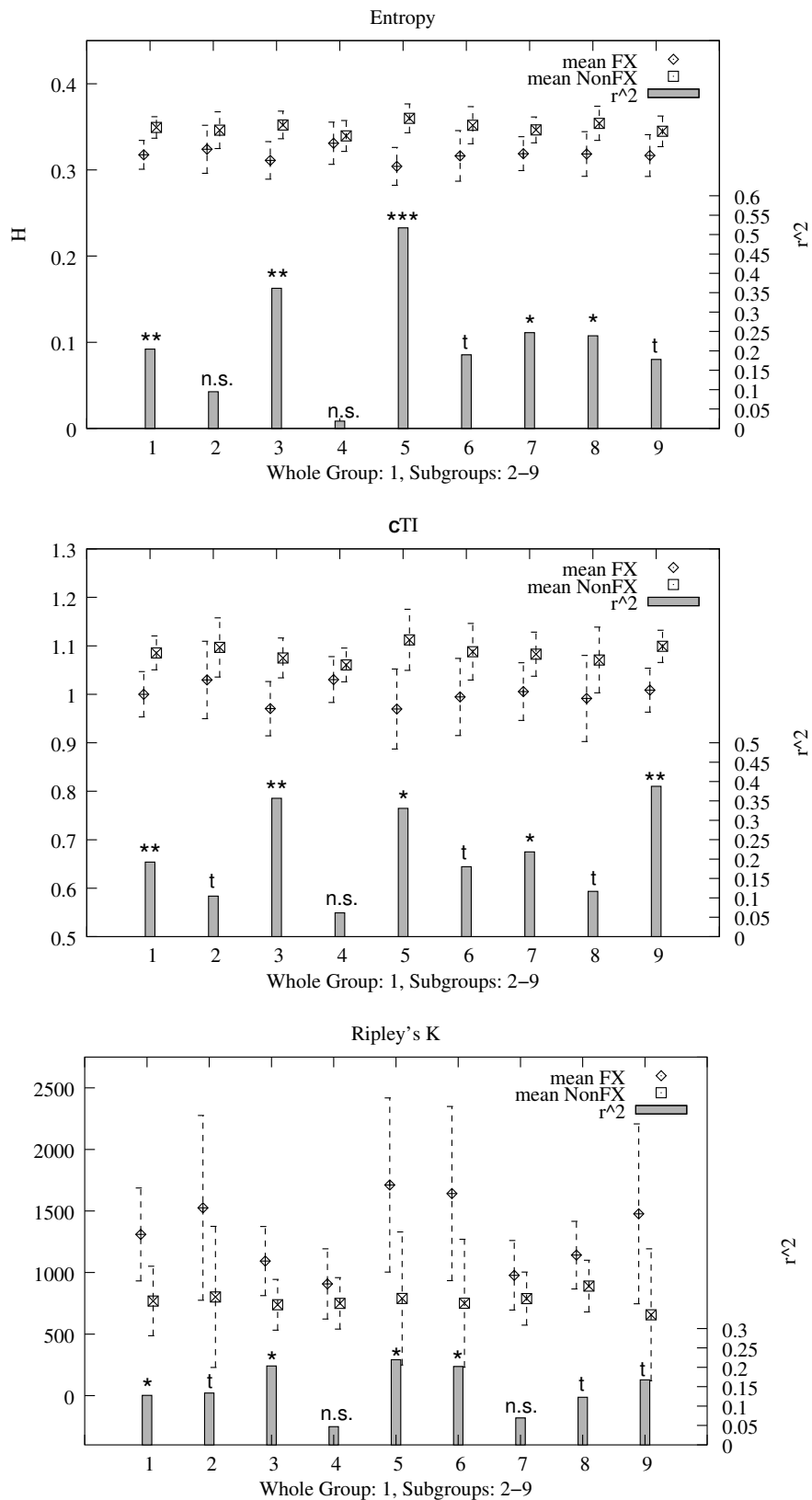
Figure 3.16: Repeated fracture discrimination of each Markovian variable: original complete group: 1, subgroups 2-9.

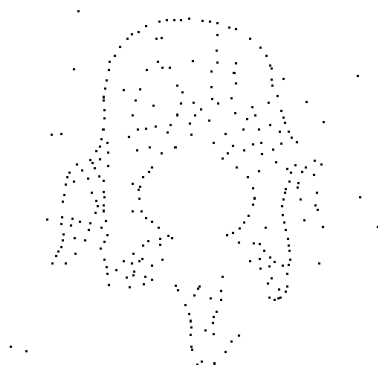Figure 3.17: Noisy slice of a HRCT-measurement in vivo.

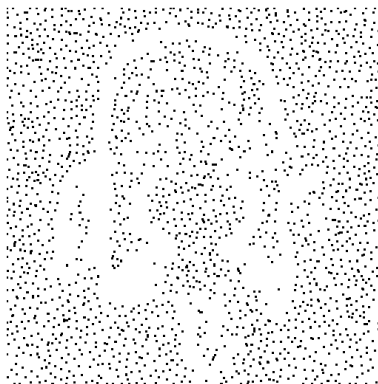Figure 3.18: Locations of grey value peaks classified as bone by use of the HMM.

Figure 3.19: Locations of grey value peaks classified as noise by use of the HMM.

Chapter 4

Discussion

Whether the hypothesis of this study, to incorporate Markov methods in order to improve both discrimination of osteoporotic from healthy networks and explanation of failure load of neighboured vertebrae was confirmed is discussed in the following sections and compared to other studies known to have performed similar research.

4.1 Relevance and method of structural analysis

Today, the bone mineral density is used clinically as a predictor of the osteoporotic status. While the risk of suffering a fracture was shown to be related to the bone mineral density [64], in another study four out of five patients with an osteoporotic fracture showed a non-osteoporotic bone mineral density [65]. This may support the hypothesis, that the bone structure, i.e. the order of bone mass inside a volume has an impact to the occurrence of osteoporotic fractures. In consequence, in addition to the measure of bone mass in terms of bone mineral density or bone volume to total volume fractions as an approximation when assuming constant mineralisation a measure of the structural design may carry independent information which should be measured to optimise a discrimination between osteoporotic and healthy trabecular networks.

For the assessment of bone structure, former studies showed that best results were obtained using high-resolution tomographic techniques [10]. Additionally, the combination of both techniques, the determination of bone mineral density and structural variables yielded the best results in the diagnosis of osteoporosis [10]. Hence, existing knowledge of bone mineral density of the vertebrae was accompanied with high-resolution measurements performed on a Micro-CT. Representations generated were capturing the whole trabecular network of a female human vertebra T12 or cylindrical parts of the centre of those vertebrae.

4.2   Catching complexity: the study hypothesis

The basic question leading to the hypothesis of this study is: is the complexity found in trabecular networks composed by a high number of trabeculae connected multiple times handled appropriately when applying standard structural variables averaging over the whole structure of these complex networks? Is it possible to investigate the local spatial characteristics of such trabecular networks by a measure assimilating information over the whole structure while not focusing on local substructures? Instead of determining an average measure of the whole structure, local properties should be measured and combined in parallel to obtain a comprehensive statement about the status of the network: osteoporotic or non-osteoporotic. The breakdown of complexity by using simple structural entities like trabeculae or parts of them and at the same time the investigation of their spatial relationship is achievable by use of Markov techniques. The Markov theory implements the focus on local properties by the lack of memory: an object depends only on a limited number of neighboured objects. Using this technique, a complex structure can be decomposed into cliques of structural entities with the latter ones not being independent of each other. It was shown, that all local neighbourships representing dependencies beyond the very next neighbour can be reduced to a neighbourship of the very next neighbours only by increasing the underlying dimension of the objects of interest [40]. The set of Markov measures maps local spatial properties of all cliques to a certain value evaluated and combined in parallel and thus preserves the ability to comprehensively describe a whole complex structure by means of local interactions.

The evidence of the importance of structural information beyond standard measures of bone density and global structural properties as well as the necessity of handling the complex nature of trabecular networks appropriately led to the hypothesis of this study (see 1.3): Markov models can be applied to the problem of assessing structural properties of trabecular networks while improving the discrimination of standard structural variables between the osteoporotic and non-osteoporotic networks independently of bone mineral density measured over the whole vertebra as well as improve the explanation of the failure load of neighboured vertebrae.

That the hypothesis was confirmed in this study for the sample set used is discussed in detail in the next sections.

4.3   Fracture discrimination

The investigation of fracture discrimination was performed for reference values like AGE, the bone mineral density BMD of the whole vertebrae, the standard reference variables $Tb.N_{mid}$ and BV/TV_{mid}, the Markov graph node probabilities as well as the Markovian

point process variables Cluster Type Index CTI and $Ripley's\ K$ function as well as for the conditional entropy as discussed in the following sections.

4.3.1 Basic conditions: age and bone mineral density

The strict definition of criteria allowing a vertebra to enter the study had the consequence of a limited sample size of 25 samples assigned to the Non-FX group (healthy subjects) and 14 samples as members of the osteoporotic FX group. Although the resulting sample size is limited due to the strict criteria chosen the clear distinction of the two study groups may be of benefit when investigating the discriminative power of measures proposed in this study. Without aiming it, the selection of samples led to two study groups not showing a significant difference in terms of bone mineral density for the whole vertebra. Additionally, the age of the donors was not significant different, too. It was 80.7 years for the Non-FX group and 2.6 years higher for the FX group. However, adjustments for age were performed. Since bone mineral density was not available for the biopsies taken from the vertebrae, the measure closest to bone mineral density was the bone volume to total volume fraction, which is similar to BMD when neglecting the different mineralisation of bone voxels.

4.3.2 Standard structural variables

The initial set of standard structural variables used as reference to which the Markovian variables investigated in this study were compared to was: bone mineral density BMD or as replacement bone volume to total volume fraction BV/TV and the trabecular number $Tb.N$ as independent set of variables from which other standard measures can be derived: trabecular thickness $Tb.Th$, trabecular separation $Tb.Sp$ and bone surface over total volume BS/TV. Principally, the representative $Tb.N$ could have been exchanged by any of the variables $Tb.Th$, $Tb.Sp$, or BS/TV without loosing any information. Within this study, $Tb.N$ was selected as reference in combination with BV/TV for biopsy-based evaluations since the bone mineral density value was calculated for the whole vertebral body, while BV/TV was obtained for the volume of the biopsy and thus its evaluation is comparable to that of $Tb.N$.

To be able to apply parametrical statistical tests it was ensured that the standard reference variables were normally distributed.

While BMD for whole vertebrae was not significantly different for the two study groups, BV/TV measured from the vertebral biopsies was significantly different: the mean BV/TV of vertebrae classified as osteoporotic was at a 75% level of that of the healthy ones. This may indicate that the centred middle vertical volume of a vertebra is more sensitive to the

osteoporotic status than the integral bone mineral density value. Consistently, in another study the inhomogeneity of vertebra was confirmed in terms of mild horizontal differences between anterior, posterior, and external areas and as vertical inhomogeneity, too [66].

As BV/TV the second structural parameter $Tb.N$ was borderline significant discriminating the study groups. Hence, for all Markovian variables, statistical tests estimating the discriminative power are performed with taking BV/TV and $Tb.N$ into account to draw conclusions of the contribution of the Markovian variables independent of the standard approaches.

The standard variables BV/TV and $Tb.N$ together did not remain significant when combined within a nominal logistic fit. This indicates, that for the study group investigated the information of both variables is not independent enough to gain explanation of variance of the two fracture groups by combining these variables. Since BV/TV_{mid} alone explained 11.45% and TbN_{mid} alone explained only 8.44%, the former value served as a reference for the innovative Markov approaches investigated.

4.3.3   Markovian variables

As done for the standard reference variables, the normal distribution property was investigated for the Markovian variables first to allow for the application of parametrical tests. For the Markovian variable $Ripley's\ K$ one outlier was identified, which called the normal distribution property into question, a second test without this value confirmed the normal distribution property. The discriminative power of $Ripley's\ K$ were not influenced since with and without the value investigated the same level of significance and a similar explanation of the variance were found ($p < 0.03$, $r^2 = 12.7\%$ and $p < 0.04$, $r^2 = 11.5\%$, respectively). As no reasons for exclusion were found this subject was left in the study group. For both the Cluster Type Index as well as the conditional entropy the normal distribution property was confirmed with the Shapiro-Wilk Test.

4.3.3.1   Node probabilities of a trabecular network

A first approach of exploiting neighbourhood relationships typical of Markov techniques was the interpretation of voxel networks as a graph carrying probability at each node for the corresponding voxel being a bone voxel in contrast to a marrow voxel. While an isotropy of the trabecular network would result in equal probabilities stored in the graph nodes, any anisotropy may be captured by this simple approach in terms of different probabilities in certain nodes along different directions.

The discrimination of the three best node probabilities was not only highly significant. Additionally, the degree of explanation of the variation between the two groups reached

for a combined model calculated by a nominal logistic fit 79%. Compared to the reference value of below 12% for the standard structural variables, this is a gain of 67%.

It has to be taken into account, that the chance for specifying variables which provide such a high discriminative power is related to the high number of variables given by the volume of $11 \times 11 \times 11$ voxels. This results in 1,331 variables, hence the result has to be relativised by the chance of selecting three best variables out of $1{,}331 \times 1{,}330 \times 1{,}229$ possibilities.

4.3.3.2 Simplifying Markovian functionals to variables

All the three remaining Markovian variables are functionals in terms of mapping point processes or graphs to a one dimensional function of distance. A result in terms of a function opens multiple pathways to possible evaluations, hence a restriction of the resulting function to one common distance was assumed to be helpful in terms of evaluation and usability. Based on the degree of explanation of the variations in the two study groups in terms of the r^2 value, it was observed that at a distance of 16 voxels (corresponding to a distance of $0.4mm$) for all three variables a maximum or a position close to the maximum of the r^2 value existed. Although a selection of a certain distance in an interval may increase the chance of selecting a variable which by chance discriminates the two groups well, the fact that all three variables share the phenomenon of showing a certain quality (i.e. a maximum) of the r^2 at the same distance led to the choice of restricting all three Markovian variables to this fixed distance.

On the other hand, a simultaneous search for the same distance over the interval measured by all three variables decreases the possibility to select a distance for which by chance all three variables work well in a statistical sense. The simultaneous search can be viewed as logical (*AND*-) conjunction.

4.3.3.3 Cluster type index

Borrowed from the theory of point processes an estimate of the *J*-function introduced in section 2.4.4.2 and derived from a spatial point pattern dataset can be used in an exploratory data analysis and formal inference about the pattern. The estimate of $J(r)$ can be compared with the constant function 1 which is the value of a Poisson process evaluated with the *J*-function. A Poisson process is by definition free of any spatial clustering or inhibition induced pattern interpreted as homogeneous. In other words, it divides the clustered from the regular spaced point processes by being itself neutral, that is non-clustered but on the same time non-regular, i.e. building a random process [36]. Hence, it can be used as a delimiter between these two pattern types: any deviations

$J(r) < 1$ or $J(r) > 1$ suggest spatial clustering or spatial homogeneity, respectively. The purpose of the J-function originally defined within the theory of point processes is to measure if and how clustered a set of points is. To emphasise this purpose for this study, it was called Cluster Type Index (CTI) instead.

When restricting the trabecular network to the set of junctions, some information gets lost by neglecting the connections of one-dimensional rods and two-dimensional plates. From the topological decomposition by separating voxel sets according to their local dimension, the set of three-dimensional junctions was obtained. The reason for restricting a network to its set of junctions (i.e. nodes) is given by the idea, that junctions define the set of possible networks given by all graphs which have a connection or do not have any connection between two nodes. Hence, junctions limit the set of possible edges between the nodes. In consequence, the potential functional aspects of a network can be interpreted as mainly defined by its nodes, rather than by its edges, building the theoretical hull of networks implementable based on the given set of nodes.

Due to this important role of junctions an investigation of the junction pattern may be beneficial when collecting structural information independent of the standard measures as hypothesised (see section 1.3).

From the evaluation of the functional CTI, which maps a structure to a function of the J-value dependent of a distance a range around 0.3-0.4 mm was observed as discriminating best in terms of the r^2-parameter. Although significant or at least showing a trend over the whole range of 0.05 - 0.6mm, the best explanation of variation was found around 0.35mm with an r^2 of 25%.

Independent of the question whether this information of variance between the study groups is independent of the standard measures, the explanation was found to be about twice as high as the structural reference value. In addition to the explanation of variation, the CTI-measure allowed to characterise the kind of clustering

The CTI-values for non-osteoporotic members of the study groups was above 1.0, which is the reference value for a Poisson process. The observable distance of the non-osteoporotic samples over the value of 1.0 indicates that healthy trabecular networks are based on more regular point patterns compared to random processes, at least in the vertical projection for which these were evaluated in this study. The osteoporotic samples were evaluated as more similar to the Poisson process, i.e. these samples resulted in values around the reference value of 1. A possible interpretation for this result can be a random damage and loss of the junctions of osteoporotic networks. Any regular pattern which looses iteratively random points looses its homogeneity at the same time, narrowing to a random pattern eventually.

4.3.3.4   Ripley's K-function

Again a measure from the theory of point processes, the $Ripley's$ K-function introduced in section 2.4.4.2 is an estimate of the expected number of additional random points within a distance r of a typical random point of a point pattern X. More specifically, this expectation value of additional points of K is obtained when multiplying K by its intensity, which is the expected number of points of X per unit area. Again, the Poisson process is a reference process which does not favour local point gains as found in clustered processes as well as longer distance point gains as found in regular processes. For a random process as the Poisson process, all distances are found to result in a gain of πr^2 points, according to the increase of the circular area investigated.

For both the Non-FX and FX group, a Poisson-like K-value was observed up to a distance of $0.35mm$. Since the Cluster Type Index CTI showed a more regular pattern with its highest r^2 for a distance of $0.35mm$, lower distances are to a higher extend subject to random patterns, while at higher distances of $0.35mm$ it is more likely to find a junction if they are regularly spaced at $0.35mm$ and hence, the expectation value increases. This is not true for osteoporotic junction patterns, since, according to the interpretation of the CTI outcomes, these follow the random principle of Poisson processes in consistence with the $Ripley's$ K results. Hence, the results for the CTI and $Ripley's$ K-functions seem to be consistent with each other.

Since the mean trabecular separation $Tb.Sp$, which can be calculated from BV/TV and $Tb.N$ is for osteoporotic samples at $1.5mm$ (standard error $0.11mm$) and for healthy subjects at $1.17mm$ (standard error $0.08mm$), the junction patterns are assumed to be more dense than the trabecular separation.

4.3.3.5   Conditional entropy

The third Markovian measure is based on the concept of conditional entropy, i.e. the amount of information which is gained from the extension of a known volume of interest over a structure [40].

The formalisation of entropy is based on structures represented by symbolic spaces, thus a transformation of the Micro-CT based representation of the structure to a symbolic one was performed. This step is crucial since the set of symbols the continuous represented trabecular network is mapped to should describe the architecture in a comprehensive fashion. A symbol out of such a description can either describe a static or a dynamic property. Descriptors of material properties like marrow voxels or bone voxels are of static type. Symbols describing relationships between neighboured voxels code dynamic properties. Out of the set of possible descriptions of trabecular networks a comprehensive

mixture of symbolic representation has to be chosen which both codes static and dynamic properties when a non-conditional entropy is to be calculated. This type of entropy was found in the literature within a few studies which described measures of complexity in the context of trabecular networks [67, 68, 69]. There, complexity was measured in terms of simple entropy, needing symbolic input of both static and dynamic type.

In this study, conditional entropy was used to allow to model the dynamic process not inside the set of symbols, but inside the algorithm to compute the conditional entropy: where simple entropy measures are build on static and dynamic symbols to capture the dynamics of the underlying process, the conditional entropy used in this study encodes any dynamics within the extension step from a current structure to an encapsulating structure. Hence, the set of symbols discretising the structure of investigation was chosen to be all of static type, which was a simplification of the encoding without loosing the facility to capture dynamics. The set of symbolic descriptors was build from the local dimension combined with the direction where neighbouring bone voxels were found. This mixture was expected to be the largest non-redundant set of descriptors coding a biopsy which rotation and orientation is not known.

Moreover, the symbolic representation of the trabecular network was based on a directed acyclic graph, allowing a fast computation of the conditional entropy in a recursive fashion.

The hypothesis (see section 1.3) included the assumption that the complexity and hence the amount of new knowledge gained from a broadening of the current view of a trabecular network would be different for osteoporotic and healthy subjects.

It was found that for non-osteoporotic trabecular networks the conditional entropy was higher than for osteoporotic ones over the whole range of distances evaluated. Thus, as a restriction to a certain distance the measure $Entropy_{dist16}$ was successfully discriminating, too. From the Markov theory, the amount of information gained when extending the the graph symbolising the trabecular network was higher indicating a more complex network for healthy subjects. In other words, under osteoporosis, networks may loose some complexity.

When investigating the examples of high and low entropy in figures 3.5 and 3.6, the more plate like structure of the samples with high entropy was observed. To test, whether entropy is a redundant measure of the plate / rod like structure of the trabecular network, the correlation coefficient (r^2) between entropy and the local dimensions was found to be 10.9% for dimension of one and non significant for the correlations with dimensions two or three (see table 3.15). Additionally, a combined model of $Entropy_{dist16}$ and $dim2\%$ resulted in a non significant $dim2\%$ while the entropy was significantly discriminating the two study groups. Hence, a redundancy of entropy with regard to the plate or rod like structure was not confirmed, and the variable $Entropy_{dist16}$ contributed independently to the discrimination of the two study groups.

Additionally, entropy contributed to the discrimination independently from BV/TV_{mid} proven in a combined model (see table 3.9): while entropy contributed significantly to the discrimination, BV/TV_{mid} was borderline significant.

After negating any redundancy of entropy from the dimensional composition and from the relative bone mass, the orientation of trabeculae may have an impact on the entropy measured: Kinney et al. observed that in human vertebrae there was 3.4 times more mass oriented vertically than horizontally. Moreover, the vertical trabeculae were 30% thicker, on average, than the horizontal trabeculae [60]. If bone mass is orientated more vertically than horizontally, this observation is consistent with the known effect of osteoporosis to corrupt horizontally trabeculae more often than vertically ones. The higher probability of finding vertically located voxel neighbours than horizontal bone voxels would lower the entropy according to formula 2.24.

However, the proportion of horizontal and vertical neighbours was not kept in this study and remains subject to further investigation. As entropy as a measure of complexity is expected to be influenced in a complex manner by many factors, the question, which reasons led to a different entropy between osteoporotic and healthy vertebrae should be investigated more intensively. The finding of this study, that conditional entropy has discriminative power should be confirmed in independent studies as well as compared to the non-conditional entropy used in the former studies investigating complexity of trabecular networks [67, 68, 69].

4.3.3.6 Combined models

To prove whether an adding of Markovian variables to standard reference variables improves fracture discrimination combined models were built after calculating the fracture discrimination of each single variable: The three variables $Entropy_{dist16}$, CTI_{dist16} and $Ripley's\ K_{dist16}$ explained 16.6%, 18.3% and 12.9%, respectively, both before and after adjusting for age.

A model build out of the three Markovian variables was not significant for $Ripley's\ K_{dist16}$, but a combination of $Entropy_{dist16}$ and CTI_{dist16} was significant for each variable and explained 33.7%, which is a gain of 22.2% compared to the best explanation of standard structural variables given by BV/TV_{mid}. Any addition of BV/TV_{mid} or TbN_{mid} to the model of $Entropy_{dist16}$ and CTI_{dist16} left the standard variable as non-significant.

4.3.3.7 Risk estimation

To estimate the risk belonging to the osteoporotic or the healthy study group for an individual sample undergoing a change of a variable's value, the standardised odds ratios of the variables under investigation were computed and compared.

After adjustment for AGE, a standardised change of a standard deviation led to significant odds ratios from 2.4 for BV/TV_{mid}, 3.0 for $Entropy_{dist16}$ and 4.0 for CTI_{dist16}. Hence, the Markov variables led to a higher odds ratio than the standard variable BV/TV_{mid} and TbN_{mid}, the latter one not being significant. A further adjustment of BV/TV_{mid} additionally to AGE led to a significant odds ratio of 3.1 for entropy only, all other standard and Markov variables did not remain significant.

Thus, entropy proofed to be the variable capable of representing an odds ratio independent of information of other variables and still providing an odds ratio as high as over 3.1.

4.3.3.8   Testing for subgroups

As this study does not contain an independent validation of the results obtained based on an independent set of samples, a test of subgroups was performed which may give an indication whether the results are random or systematic ones.

Since a bootstrapping method was not available, a limited set of subgroups were built with the condition that the difference in terms of members between the subgroups were maximised. To obtain the widest variety possible for a given number of subsets, the two sample groups were divided in a fashion that each new division combined as many as possible elements from different groups of the subgroup generation built before (refer to splitting scheme 3.14).

The Markov graph based node probabilities for the two best variables showed for all groups a r^2 of 49.9%. The subgroups resulted for the same calculation in a r^2 between 39.5% and 63.2%. This may lead to the interpretation that the subgroups support the original test.

The t-tests for the subgroups depicted in figures 3.15 and 3.16 may confirm the findings for the two study groups: Inside the group of standard structural variables for BV/TV_{mid} and TbN_{mid} the trend, i.e. the relative positions of the mean values between the osteoporotic and healthy samples were reproduced by the study groups. This was true for AGE except to the second pair of subgroups. The Markovian variables confirmed the trend of the study groups in each pair of subgroups, too. Without having quantified it, the number of non-significant pairs of subgroups was found to be related to the significance of the study groups.

The non-parametric test of building all possible pairs of values between the osteoporotic and healthy study group shows a deviation from the behaviour of a random variable: The zero-value percentile, which would be 50% for a random variable was found to be within 66.7% for AGE, and 77.4% and 80.4% for TbN_{mid} and BV/TV_{mid}, respectively. The Markovian variables were found to be above these values within the range of 87%

to 89.3%. This deviations, by their absolute values and by their order, may confirm the outcomes for the standard variables and the Markovian variables.

4.4 Explanation of failure load

An assessment of the integrity of bone was given by measures of the failure load of the vertebral segment T9-T11. Although these are vertebrae neighboured to the vertebra T12 used in this study, the neighbourship should allow to draw some conclusions of the failure load of T9-T11 to T12. The highest explanation of the failure load was achieved by a non-structural variable, the fraction of one-dimensional voxels reached a r^2 of 35.9%. Since no combination with a structural variable resulted into a model with all contributors being significant, the best combined model was found by a combination of the reference variable BV/TV_{mid} and the $Entropy_{dist16}$ (see 4.4.3).

4.4.1 Reference variables

The best standard structural variable in terms of explanation of failure load of T9-T11 were BV/TV_{mid} with a $r^2 = 35\%$, thus in this study bone volume was a main determinant of structural integrity. The number of trabeculae explained with 33% a comparable amount of the failure load. This is consistent with the high correlation TbN_{mid} showed to BV/TV_{mid} and with the fact, that a combined model of BV/TV_{mid} and TbN_{mid} resulted in both variables being non-significant, thus BV/TV_{mid} and TbN_{mid} might be interpreted as partly redundant.

4.4.2 Markovian variables

The best Markovian variable $Entropy_{dist16}$ alone explained 17.2% of the failure load, which is roughly half of the amount of explanation the reference variable BV/TV_{mid} reached. The Cluster Type Index CTI_{dist16} and $Ripley's\ K_{dist16}$ function showed lower r^2 values with 10.4% and 12%, respectively. After adjusting for AGE, only the entropy remained significant ($p < 0.05$) while the Cluster Type Index and $Ripley's\ K$ function showed a trend. Compared to the standard reference variables BV/TV_{mid} and TbN_{mid} which were highly significant correlating, the single Markovian variables did not explain as much as the reference variables did. However, the amount of information independent of the standard measures carried by the Markovian variables was measured in terms of combined models as discussed in the next section.

4.4.3   Combined models

Although the explanation of the failure load was below one half of the standard reference variables, the best gain of explanation by combining any other structural variable to BV/TV_{mid} was achieved by selecting the Markovian variable $Entropy_{dist16}$ reaching 43.1% and thus adding 8.1% to the explanation of BV/TV_{mid}. Hence, one fifth of the explanation of failure load was contributed by the conditional entropy measure independently of any other variable.

4.5   Local dimension

A side-effect of the topological decomposition was the determination of the dimensional composition of trabecular networks. Approximately less than 5% percent were detected as voxels assigned to rod-like trabeculae, while 50% of the voxels were classified as two-dimensional. Additionally, 45% of all voxels built junctions, i.e. were classified as three-dimensional. The amount of three-dimensional voxels were not expected as only 5% below the two-dimensional voxels, but may be explained by the fact that three-dimensional voxels may be found not only at typical junctions but also at parts of the trabecular network showing a certain degree of local curvature. However, every curvature classified as three-dimensional may be interpreted as junction. The correlations for the dimensions two and three were not found significantly correlated to any other variable than BV/TV_{mid}, although trends were found. Only dimension one were observed as significantly correlating weak to all structural variables. The variation of BV/TV_{mid} were explained by 61% which was not expected when considering the low fraction of one-dimensional voxels of the bone volume. Taking into account, that a rod-like trabeculae is found in a trabecular network even when plate-like trabeculae are vanished by perforation, a certain amount of rod-like trabeculae may be necessary to provide structural integrity. This interpretation is supported by 51% explanation of variance of TbN_{mid} by voxels of dimension one.

Additionally, the importance of the fraction of one dimensional voxels is found when a combined model of $Entropy_{dist16}$ and AGE was calculated in order to explain the failure load of the neighboured vertebrae T9-T11: the one dimensional fraction was highly significant while the entropy showed only a trend. However, the best explanation of the failure load was given by the combination of $Entropy_{dist16}$ and BV/TV_{mid} with 43.1% compared to 35% explained by BV/TV_{mid} alone.

4.6   Testing redundancy

The gain of explanation by Markovian variables together with the observation that at the same time standard variables were left non-significant indicate that these innovative measures of structural properties may not be redundant, i.e. do not measure equivalent structural characteristics. Another evidence for the orthogonality of these measures to the standard measures was driven by the evaluation of correlations between the Markovian variables and between the Markovian and standard structural variables. The highest correlation was found as expected between BV/TV and $Tb.N$ ($r = 0.92, p < 0.001$). All correlations between standard measures and Markov based measures were weak, i.e. had a correlation coefficient of below $r = 0.53$. Hence, neither moderate nor strong relationships between the innovative and established measures voted for information measures of the Markov approaches being dependent of the standard structural variables.

4.7   Hidden Markov Model for noise detection

The first results obtained for the HMM application for the discrimination of noise from structure induced grey value peaks should be interpreted as a proof of concept. No phantom was available which would have provided a ground truth the classification results could have been checked against. Nevertheless, some indications showed that an application of HMM to the task of noise reduction as a preceding step to a structural characterisation may be of benefit:

The specificity was estimated as very high (99.0%). This estimation was possible as for the peaks outside of the vertebra the ground truth was known: outside a vertebra all peaks belong to the class not-bone. In contrast, the ground truth for peaks inside the vertebra was not known, which resulted in a low sensitivity of 34.9%. The different areas inside and outside of the vertebra were taken into account by normalising the numbers of peaks according to the ratio of 2 : 1.

Four measurements of excised vertebrae T12 with a surrounding layer of peas, simulating soft tissue producing noise similar to that found in in vivo measurements were performed in vitro. The results indicated a relationship between the number of peaks detected as bone versus bone mineral density, which was not given before the classification.

Clearly, further investigation has to be done to prove whether the classification of grey value peaks typical of HRCT measurements is appropriate to be used as a preceding step for a structural classification of trabecular networks measured in vivo. The very first results presented here may be promising.

4.8   Related studies

The number of studies investigating structural properties of cancellous bone are as numerous as the number of possible structural variables is. The orthogonality of information of different structural variables still is not clarified. This study investigated certain aspects of trabecular networks: the complexity and evidence of local interactions of trabeculae. The number of studies found which performed comparable research seems to be limited: A few studies investigated the complexity of trabecular networks, too [67, 68, 69]. In [67, 68], the complexity was based on two-dimensional symbolic encodings of static and transitional grey-value configurations obtained from HRCT with voxel sizes of $182\mu m$. The complexity of the bone structure was found to be related exponentially to its density. Normal bone had a complex ordered structure, while the architecture during the initial stage of bone loss was characterised by lower complexity and a maximal level of disorder. Increased bone loss led again to ordered structures with minimal complexity. In this study, the BMD was not significantly different between the two study groups, but the measure of entropy and thus the complexity was. Although BV/TV was different, a correlation between BV/TV and the entropy was not significant. Hence, this study starting with an osteoporotic study group and a healthy study group which differ mainly by the fact, that a fracture was identified at the spine of the vertebra from the osteoporotic group, the successfully discriminating entropy supports the interpretation, that complexity might be independent from the bone volume fraction or the bone mineral density taken from whole vertebrae. The question, whether the measures of complexity applied in [67, 68] discriminate between osteoporotic and healthy subjects was not investigated there.

In [69] 3D-measures of complexity were calculated for Micro-CT measurements with a voxel size of $20\mu m$. Static and dynamic symbolic encodings were chosen, too, although the transitional component were represented by the surface voxels, only. Hence, the aspect of dynamics was represented to a lower extend compared to both the works in [67, 68] and this study. The loss of complexity was related to a loss of bone density as indicated in [67, 68] and was confirmed by two independent measures, the Normalised Entropy of geometrical locations and the Spatial Structure Complexity Index. Correlations between measures of complexity, computed as modifications of the formula of entropy, and structural variables were performed in terms of the use of the "gold standard" 2D-histomorphometry. The high correlations found between complexity and structural variables were interpreted in a way that 3D measures of complexity combine and assess different kinds of information and quantify the bone architecture in a holistic way. Another interpretation, based on the comparison with outcomes of this study could be, that the measures of complexity applied in [69] as well as in [67, 68] are redundant in terms of existing structural variables. A measure carrying independent information is likely to correlate moderate or weakly with existing structural variables. A reason might be the restricted symbolic encoding of some structural aspects like grey valleys or surface voxels while using non-conditional entropy.

The entropy measure used in this study investigates the dynamical aspects of all symbolic encodings incorporated by utilising conditional entropy which quantifies the dynamics of every symbol detected in the symbolic representation of the structure. However, the different outcomes of this study and the studies [67, 68, 69] should be investigated further to identify the need of conditional or non-conditional measures.

Only if measures of complexity or entropy are proven to carry information independent of established structural variables and thus discriminate between healthy and osteoporotic subjects, they may be of benefit when osteoporosis is to be diagnosed clinically in the long term.

Another approach related to standard structural variables while at the same time stating an innovative character was found in four studies utilising Minkowski functionals, which are investigated together with the isotropic scaling index method or the anisotropic scaling vector method [70, 71, 72, 73].

In [72] the scaling vector method was introduced as an anisotropic extension of the scaling index method in order to assess anisotropic information from the trabecular network. After combining the grey values into a common space with the spatial information a four-dimensional space resulted. However, the anisotropy investigated was related to the grey values only, hence two out of three angles describing rotational axis were set to zero in order to assess rotations around the grey value axis only. To describe anisotropy, six parameters had to be chosen in advance: a scaling parameter L, the rotation angle Θ which was set to the main direction of the trabeculae, and Eigenvalues λ_i representing weighting factors. Various scale parameters and eigenvalues have been tested in order to optimise the results.

The results indicated, that the scaling vector method correlated best ($r = -0.92$) with the maximum compressive strength, while the correlation of the morphological variables ($0.6 < r < 0.52$) and BMD ($r = 0.72$) with the biomechanical measure was lower.

To put the results into perspective, it should be considered that the number of slices per specimen was differing, hence properties of femora represented by more slices than the mean number might be found over-weighted within the results, while properties of femora with fewer slices evaluated might not have the weight in the results the should have. By choosing different number of slices, an avoidable factor of uncertainty with regard to the results was incorporated. The choice of a certain rotation angle Θ applied to all voxels investigated might not be appropriate since trajectories inside femora are curved, not linear. Hence, the local rotation angle reflecting the main direction of trabeculae changes depending on the spatial position inside the femur. With regard to the rest of the parameters, that is the scaling parameter and the Eigenvalues, instead of choosing a fixed parameter set bounded to reasons based on the properties of the trabecular network, this five-dimensional parameter space was screened for values optimising the results without

investigating the meaning of the parameter values used. Since the optimisation step finally resulted in a subset of voxels used for the scaling vector method, it is questionable whether a subset of voxels optimised with regard to certain criteria for the competing morphometric parameters BMD, BV/TV and $Tb.N$ would increase the amount of explanation expressed by r^2 of the failure load, too. Additionally, the regions of interest used for the evaluation of the scaling vector method was described as containing the region of interest used for the calculation of the morphometric parameters. These ROIs should be identical to ensure best possible comparability. Finally, the reference to a variable introduced to investigate anisotropy should not be a set of measures not assessing any anisotropy. The reference should be taken out of the set of existing measures of anisotropy as, for example, the method of Mean Intercept Length (MIL) based on the calculation of an ellipsoid fitted to the trabecular structure measures anisotropy in terms of computed eigenvalues. This variable was found to be sensitive with regard to osteoporotic changes of trabecular bone measured with the same modality MRI [74] and is known as stereological parameter for at least 25 years now [75].

The study [70] compared three Minkowski functionals (area, circumference, Euler characteristic) with a method measuring local dimension, called scaling index method, applied to two-dimensional images. For these measures already published equivalent measures can be found: Area is represented by BV/TV, the circumference is related to the rod or plate like shape measured by the Structure Model Index [76] or the surface voxels measured by the morphological variable bone surface over total volume (BS/TV), and the Euler characteristic is computed by a variable known as connectivity density (CD), normalised with regard to the volume or area investigated.

The scaling index method results in a continuous measure of local dimension, that is a result of approximately 0 for point-like structures, 1 for one-dimensional structures, 2 for plate-like structures, and 3 for homogeneous areas.

When comparing original MRI measurements with patterns synthesised by simulated annealing techniques based on constraints ensuring to preserve only the properties of the Minkowski functionals obtained from the original MRI measurement, the outcome was, that local dimension measured with the scaling index method was not preserved.

This result is to be expected, since the constraints defining the synthesised patterns did not contain any information about the local dimension. The conclusion drawn in that study was to incorporate dimensional information, in agreement to our study, where dimensional information was a part of the input to conditional entropy.

In [73] the application of the three Minkowski functionals describing variables equivalent to BV/TV, BS/TV, the mean curvature and the connectivity density were compared to structural variables and the bone mineral density in terms of correlation to the maximum compressive strength. It was found, that the Minkowski functionals itself explained in a

combined model 57%, variables derived from the Minkowski functionals explained 56% for femoral specimens, and 89% for vertebrae. An optimisation of all Minkoswki functionals explained 62% (femora) and 89% (vertebrae). All morphological standard structural variables were evaluated only as single variables and not as a combined model as it was done for the Minkowski functionals. The results of the single standard structural variables remained below 54%. The bone mineral density was found to explain 68% when considering all specimens, 72% for femora, and 43% for vertebrae of the maximum compressive strength.

What was left to be answered is, what explanation can be reached when combining the different standard structural variables. Second, as the Minkowski functionals seem to be similar to standard morphological variables, a combined model of the Minkowski functionals and the standard structural variables would prove whether the Minkowski functionals can be interpreted as redundant to existing standard approaches. Third, it was not investigated whether the Minkowski functionals are contributing significantly and independently from bone mineral density to the explanation of the maximum compressive strength. This can be investigated by using the same statistical model used for the combination of the Minkowski functionals and thus should be investigated.

In [71] the scaling index method was used in comparison to bone mineral density by evaluating the area under the curve of an ROC analysis specifying the amount of correctly identified patients with or without osteoporosis. The scaling index method in this study incorporated an optimisation step with regard to the starting points and width of the windows used to calculate the scalar quantities of the scaling index compared to the BMD. The scaling index method was found to result in a mean area under curve of the ROC analysis of 0.927, while the BMD was resulting in a mean value of 0.732 determined by a bootstrapping method. However, when incorporating an optimisation step without justifying the parameters selected and resulting in a best result, the bootstrapping method should be enlarged by the whole range of parameters instead of only using an optimised set. An extended study should either incorporate not only optimised values for the scaling index method, but all possible values for this parameter, or justify the selection of the optimised parameters. This is necessary since the scaling index method defines a subset of voxels incorporated into this measure, and a selection of a subset itself might be such that a bigger area under curve is obtained by chance, only.

4.9 Limitations

As in every study some limitations can be specified for this study, too. These are discussed in the subsequent sections:

4.9.1   Data acquisition

The sample size was determined by a strict selection of vertebra to obtain two well designed study groups of osteoporotic and non-osteoporotic vertebrae with a clear status, restricted to females to exclude possible gender-specific differences. On the one hand, this design may have contributed to the results of this study although the sample size of 14 vertebrae of the FX group and 25 vertebrae of the Non-FX group is clearly limited. On the other hand there exist statistical tests like the ROC analysis, which need a larger sample size to provide meaningful conclusions. For this reason, an ROC analysis was not possible within this study. Nevertheless, standard statistical tests like t-tests, nominal logistic fits to build combined models and correlations were possible and successfully performed.

The restriction to female donors allowed to exclude possible gender specific variations from the analysis. However, with life expectancy increasing for both men and women, the National Osteoporosis Foundation (NOF) predicts that by 2020, approximately 40 million women and 20.5 million men will have low bone mass or osteoporosis. Hence, osteoporosis in men is worth investigating, too. For this purpose a second group of male vertebrae would have to be classified as done for female vertebrae in this study.

4.9.2   Data analysis

Although the standard structural variables are well established, the variety of possible standard measures as discussed in section 1.2 is larger than captured by the standard variables utilised in this study. A more comprehensive combination of structural variables with investigated and minimised redundancy would be a more powerful reference for the Markovian variables than the provided set. Further comparisons should be performed.

Usually, the scientific results of a study have to be confirmed on an independent sample set similar to the study set. Since the overall size of the study groups in this study are limited, a split into a test and a validation group was not possible. Although a subgroup-testing was performed (see 3.5), an independent validation is not substitutable by this technique. Nevertheless, the validation should be performed not only by an independent sample set. An independent investigator would complete the validation.

4.9.3   Conceptual limitations

Although using a structural model which is well established in the scientific community ([63]), the parallel plate model on which the calculation of the standard structural variables is based may be limited in terms of the general configurations trabecular networks can have. The variety of network types is given by mostly plate-like trabecular networks

or mostly rod-like trabecular networks or, of course, mixtures of them. Thus, the error made when using a parallel plate model for the calculation of standard structural parameters depends on the percentage of rod-like trabeculae. For the study groups investigated roughly 4% one-dimensional voxels and 51% two-dimensional voxels were identified. Thus, more than ten times more plate like trabeculae than rod like trabeculae were found (the rest was detected as three-dimensional, junction-type trabeculae). Hence, the error when using a parallel plate like model for trabecular networks being mixtures of rods and plates may be not invalidating the study.

The point patterns used are two-dimensional since for the estimation of the J-function based CTI and the K-function fast estimation algorithms existed within the framework of the S-$Plus$ substitute R [51]. The third dimension was partly captured by repeated 2D evaluations (2.5-dimensional) over the length of the 3D stack. However, the information content of a real 3D measurement was not included by this technique. A development of fast three-dimensional estimation techniques would allow to evaluate the real point pattern of junctions. However, the 2.5-dimensional techniques of this study discriminated successfully.

The graph based entropy estimation did not take the rotation and direction of the biopsy into account, which was not observable after extraction of the biopsies. The reduction of dimensionality was therefore comparable to the point process approach: directions of voxel based neighbourhoods were discriminated for vertical and horizontal neighbours. Additionally, the local dimension of each voxel was taken into account, which included three-dimensional information again.

So far it is unknown if and to what extend the results obtained within this study for vertebrae T12 are transferable to other vertebrae, or even to other bone sites like femora. Principally, the techniques based on trabecular junctions and thus formally as point processes or based on symbolic codes of trabecular networks in terms of graphs are applicable to any trabecular network. However, the results may differ due to other characteristics like other trajectories found in femora in contrast to main vertical and horizontal directions in vertebrae. It may be of interest to extend this study in terms of using other bone sites.

4.10 Summary

This study investigated the value of Markov measures for quantified structural characterisations of trabecular networks. The starting point of this study was the abstract hypothesis, that the complexity of trabecular networks is not catched sufficiently by existing structural measures. A basic hypothesis of this study was the applicability of

Markov methods to the task of structural characterisation with the aim of better explaining the differences between osteoporotic and healthy human vertebrae and, additionally, improving the explanation of the failure load.

Hence, the first step was the identification of methods out of the variety of available Markov methods suitable to quantify the characteristics of trabecular networks and to model osteoporotic changes. Additionally, graph-based representations of the trabecular networks were used to implement measures of node probabilities and conditional entropy. A parallel approach was the dimensional decomposition of the networks with the aim to restrict a network to its three-dimensional parts representing point patterns. This allowed to apply measures of Markov point processes.

After the definition of Markov methods and their adaption to usable structural measures, the second, more specific hypothesis was tested, whose confirmation is at the same time confirming the basic hypothesis of applicability of Markov methods: the improvement of fracture discrimination and correlation to failure load was investigated.

It was shown, that the incorporation of local characteristics led to significant, independent measures allowing for successful discrimination beyond the standard structural variables. The Markov variables $Entropy_{dist16}$ and CTI_{dist16} together improved the fracture discrimination of the standard variables by 22% and the correlation to the failure load of adjacent vertebrae was improved by $Entropy_{dist16}$ alone by 8%. These results were obtained after adjustment for AGE and BV/TV, if the latter one was significant.

This confirmed, that complexity and local interactions were not fetched by standard structural variables as BV/TV and TbN as modelled and exploited by the innovative Markov methods applied. These results on the one side confirm the benefit of structural characterisations by entropy and cluster analysis, on the other side encourage further investigations of questions still open:

- Can the promising results of this study be confirmed with independent data sets, optionally on different levels of resolution?

- Can the Markov measures used in this study improved in terms of incorporating the third dimension for point process measures or improving the handling of the orientation of biopsies in order to increase the symbolic space supplied to the entropy?

- Are there other Markov measures suitable to be applied to the task of structural characterisation?

Although several limitations were identified, the results obtained may be promising and lead to further research of the application of comprehensive Markov techniques to the

field of structural characterisation of cancellous bone and perhaps of other biological and non-biological networks.

In summary, the Markovianity of trabecular networks were confirmed and successfully used to improve structural characterisations of these complex networks.

Chapter 5

Future perspectives

The basic research of evaluating the applicability of Markov techniques to the field of structural characterisation of trabecular networks was performed on one of the best methods currently available to reconstruct representative parts of the networks investigated: Micro-CT.

Since this investigation was based on a set of excised vertebrae, this study of evaluating the application of Markov techniques to Micro-CT measurements clearly is an in vitro basic research project. Principally, the utilisation of biopsies obtained from clinical routine would be possible, too, although the availability clearly is limited.The question discussed in this chapter is the applicability of Markov techniques to in vivo measurements obtained by High Resolution Computer Tomography (HRCT).

5.1   Markov techniques applied to HRCT

HRCT images typically show a low signal to noise ratio (see figure 2.2) in section 2.2.1. When investigating the pattern induced mainly by noise, i.e. outside of vertebra in the soft tissue (see surface plot at figure 2.2), a typical mountain / valley arrangement is observed. Since the number of grey value peak is lower than the number of pixels, typically with a factor of around 10, the intrinsic resolution of the measurement may be lower than the nominal resolution specified by the measurement parameters.

One question to be discussed is: are the Markov techniques applied in this study still useful to model trabecular networks when measured with HRCT? And are there perhaps other problems which potentially can be solved by Markov techniques?

5.1.1   Do Markov techniques still work with HRCT?

The application of HRCT to the digitisation of trabecular networks results in a non-complete acquisition of the osseus network. First measurements done (see 2.2 in section 2.2.1) at the Medical Physics Research Group (University Hospital Schleswig-Holstein, Campus Kiel) as well as theoretical considerations implicate, that only the bigger part of a trabecular network may be visualised with HRCT.

However, there is some evidence that the techniques introduced to the field of structural characterisation of cancellous bone and discussed in this study may still capture structural aspects when applied to HRCT.

5.1.1.1   Markov graphs on HRCT Measurements

The approach to model voxel probabilities in section 2.4.5 actually was performed on a voxel size of $(160\mu m)^3$ to capture larger scale characteristics of vertical and horizontal trabeculae. Although the nominal resolution already fits the HRCT approach, the amount of noise of HRCT generated datasets is higher than that of Micro-CT measurements.

When noise is modelled as a random variable added to all probabilities stored in the Markov graph with a certain but fixed variance and mean of zero, the limit of a theoretically infinite number of additions of noise to the node probabilities does not change the probabilities, i.e. the noise added infinite times to the probabilities vanishes. Hence, depending on the number of voxels visited to estimate the node probability the effect of noise may be neglectable.

In consequence, although a higher number of locations may have to be visited to determine a certain node probability to be bone, this approach may still work with the modality HRCT.

5.1.1.2   Point process based measures applied to HRCT

The J and Ripley's K-function were applied to the trabecular network as measured by Micro-CT and subsequently restricted to the three-dimensional parts of it: the junctions (chapter 2.4.4.4). To answer the question whether this approach may still work with HRCT measurements, it has to be investigated if typical trabecular junctions appear within a HRCT measurement.

According to table 5.1.1.2 the median of the diameter of junctions obtained by Micro-CT is one third of a millimetre. This corresponds to a two pixel diameter (NonFX) and almost two pixels (1.8 pixel for FX) equivalent for HRCT measurements with a pixelsize of $(150\mu m)^2$, respectively.

Voxelsizes (1:6)	Micro-CT: $25\mu m$		HRCT: $150\mu m$	
Percentile	Area [pixel]	est. diameter [pixel] (μ-CT)	est. diameter [mm]	est. diameter [pixel](HRCT)
FX				
90%	137	43.61	1.09	7.27
median	34	10.82	0.27	1.8
10%	9	2.86	0.07	0.48
NonFX				
90%	120	38.20	0.95	6.37
median	38	12.10	0.30	2.02
10%	9	2.86	0.07	0.48

Table 5.1: Areas of trabecular junctions within a 2D-slice. The estimated diameter was calculated based on the assumption that the area was circular (i.e. diameter $= \frac{\text{area}}{\pi}$). The estimation of the diameter of the same junction measured by HRCT is given in the last column.

A structure with a width of one pixel usually generates partial volume effects due to the zero probability that the structure is exactly overlaid by the pixel grid without overlapping, assuming a continuous space. In contrast, a structure with a width of two pixels guarantees that the underlying structure is visualised at least within one pixel without partial volume effect.

Hence, at least 50% of the junctions detected by Micro-CT are visualised without (in case of NonFX junctions approximately without) partial volume effects in HRCT when using a pixelsize of $(150\mu m)^2$. 90% of all junctions fill approximately 50% of a HRCT pixel.

Although HRCT measurements cannot depict all details measured by Micro-CT due to technical conditions, the use of HRCT as in vivo technique to investigate trabecular junctions and the corresponding point process measures may be promising based on the estimation given above.

5.1.1.3 Conditional entropy applied to HRCT

In section 2.4.5.2.3 the approach of estimating each voxel's local dimension based on the formation of its neighboured voxels is given. The neighbourhood was defined as the set of all voxels within a diameter of voxels. Thus, the local neighbourhood was defined in a distance of $11 \times 0.25\mu m = 2.75mm$. Changing to a modality using voxels of $150\mu m$ side length needs either less voxels or defines a new scale. The smallest possible neighbourhood of one voxel around the one to be estimated would mean a diameter of $0.45mm$. But such a small neighbourhood may not allow to estimate the local dimension in a stable

way. Additionally, due to discretisation the angles allowed are restricted to a set of 45 steps. Thus, an increased neighbourhood with a diameter of seven or again eleven voxels establishes the same robustness of dimension estimation while changing the scale of the structures under investigation. A diameter of seven voxels takes local structures with a size of circa one millimetre into account, a neighbourhood of eleven voxels defines a diameter of $1.65mm$.

Since vertebra typically show trabeculae which run from the top to the bottom of the vertebra (beside other orientations and links between these vertical trabeculae), it can be assumed that trabeculae with dimensions near the height of a vertebra (circa 20mm and above) exist. Thus, a neighbourhood of a few millimetres may be reasonable to model local dimensional aspects of the trabecular network.

Moreover, as with HRCT a whole vertebra can be measured, a change of scale may suitably reflect the larger volume of interest. Additionally, since HRCT takes a coarser level of detail into account than Micro-CT, an investigation of the larger structures captured by HRCT may be indicated and reasonable.

5.1.2   Further application of Markov techniques

5.1.2.1   Noise as a Markov point process

The randomness typically inherent to a noise process overlaid to a deterministic structure which is investigated can be exploited in order to separate the superimposed random process from the underlying deterministic one. The deterministic structures of trabecular networks can be assumed to be locally linear, since it is composed in terms of rods and plates. The three-dimensional junctions build an exception from this assumption. In contrast, the noise induced peaks lack linear concepts. An example of noise detected in an in vivo HRCT measurement is given in figure 5.2 as a three-dimensional rendering of the soft tissue after the application of a certain threshold defining locally limited peaks.

When measuring three-dimensional spaces in terms of a set of slices, each noise induced grey value peak is a three-dimensional object, which can be viewed as a (possibly marked) point process. Hence, grey value structures are decomposed in terms of locally bound grey value peaks (see figure 2.2). The linearity of trabecular structures contrasts the absence of spatial interaction of noise induced peaks. Thus, the task of separating the noise process from the underlying structure is to specify these peaks which show no spatial relationship.

The Markov point process measures, the J and Ripley's K-function introduced in chapter 2.4.4 can be used for the task described above since for them the theoretical value for a Poisson process is known. Therefore, a relative distance of a point pattern X can be estimated with regard to the Poisson point process which is known to be free of spatial
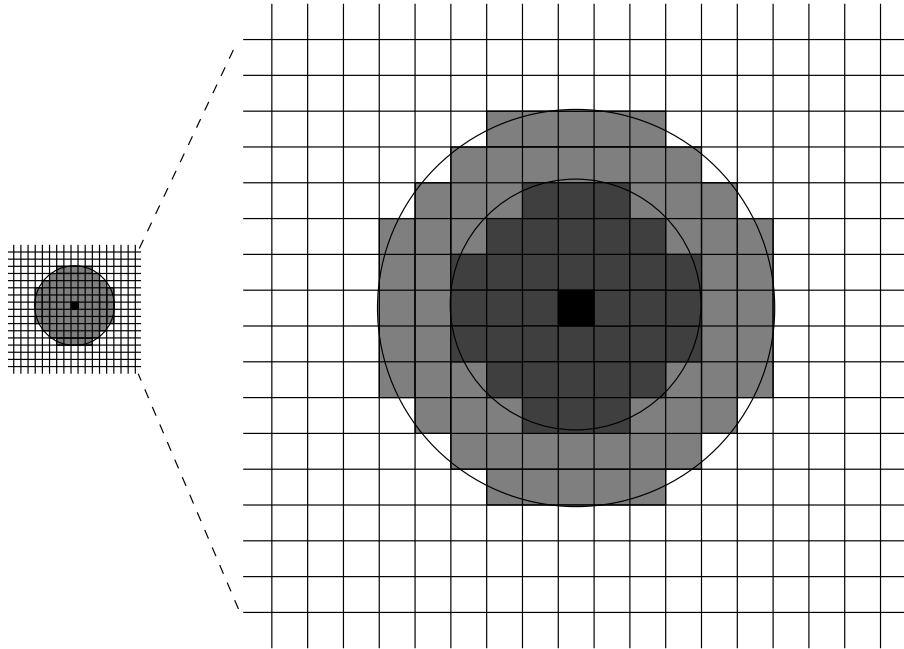
Figure 5.1: Applying the technique of Local Principal Component Analysis presented in section 2.4.5.2.3 to HRCT instead of Micro-CT corresponds to a change of the scale: The median diameter of one third millimetre was represented by a set of 12 voxels when measured with Micro-CT. With HRCT, the same diameter is represented by two voxels. With respect to the constant trabecular structures an estimation of the local dimension of a HRCT voxel may be based on a smaller radius: Instead of taking voxels with a distance of five into account, proposed three voxels in HRCT mode define a distance of $0.45mm$, which may be sufficient.
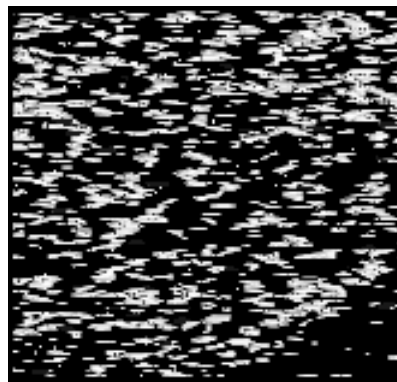
Figure 5.2: Three-dimensional rendering of a HRCT noise induced point process

dependence (both the J and the K-functions are functionals since a point process is mapped to a function, i.e. the J/K-value as function of a distance r in a predefined interval I within the point pattern):

$$Dist^J_{Poisson}(X) = \sum_{r \in I} \|J_{Poisson}(r) - J_X(r)\|, \quad J_{Poisson}(r) = 1 \ \ \forall r \in \mathbb{R} \qquad (5.1)$$

The measure $Dist^K_{Poisson}(X)$ of distance[1] to a Poisson process based on Ripley's K-function can be defined by simply exchanging the J-function by K. Having defined these two functions, a minimisation of them together with a permutation of subsets of points can be used to extract the random pattern of the overall point process.

The algorithm proposed to separate random peaks from structure induced ones is outlined as follows:

algorithm 1. For a given point process X with a structure superimposed by the noise pattern do:

1. Select a subset $X^{test} \subset X$ of randomly chosen points

2. Estimate the distance to a Poisson process based on $Dist^J_{Poisson}(X^{test})$ or $Dist^K_{Poisson}(X^{test})$. If this is the first iteration, go ahead. Otherwise decide, whether the distance has decreased:

   - If yes, accept subset X^{test} by adding it to the previously accepted points $X^{accepted} := X^{accepted} \bigcup X^{test}$.

   - If not,
     - (a) reject it, or
     - (b) accept it only with a (low, predefined) probability p (similar to the Metropolis-Hastings approach to allow to escape from local minima)

3. If the decrease of the distance function stays above a predefined threshold, go back to 1. Otherwise emit the resulting set $X^{structure} := X \setminus X^{accepted}$

A possible modification of the algorithm given above is the incorporation of several characteristics like potential orientations of grey value peaks which may occur in the case of HRCT measurements. Additionally, the volume with respect to a certain threshold can

---

[1]The term measure is not appropriate as the functions defined above not necessarily fulfil all requirements of the mathematical object *measure*. These functions only serve as a relative estimation of distance.

be modelled, too. The integration of these characteristics can be performed by the use of marked Markov point processes [36].

An example for the application of algorithm 1 to a linear structure overlaid by a Poisson process is given in figure 5.1.2.1.

Some problems remain to be solved:

- The algorithm has to be investigated with regard to the convergence to a Poisson process. How is the probability to be chosen to accept increased distances in terms of simulating a Metropolis-Hastings algorithm?

- If a totally random process is given without any deterministic, linear structure, the elimination of a subset of points may indeed result in a pseudo-linear structure just by leaving randomly, but linearly arranged points untouched.

- Points which fit to a Poisson process selected so far may belong to the linear structure which is searched for. Thus, although a point is not of random nature, it may fit into the Poisson process.

These problems have to be investigated when the proposed algorithm is worked out.

5.1.2.2   Simulating osteoporosis by Markov techniques

As stated in chapter 2.4.2.3, the Markov theory allows to extract enough information of a structure to be able to reproduce a similar structure with regard to the structural properties measured and modelled. This technique is formalised in the Metropolis-Hastings algorithm (or Gibbs sampler) [35].

Hence, measuring the structural properties of a certain group of structures like osteoporotic and healthy networks, a group-representative structure may be generated by this technique. First, a clustering problem has to be solved: one had to determine how many structural examples are needed to capture the structural variety of a group, and how many groups are needed to model the variety of osteoporotic and healthy subjects. Subsequently, the structural characteristics of each group could be retrieved by the different measures of the Markov theory and representative, regenerated structures may be generated which may allow to visualise and investigate typical stages of the disease.

Primitives on which the simulation could be based could be either the topological classified voxels with dimensions of one, two or three, or whole models of single trabecular (rods, plates, junctions). For both approaches, the Gibbs sampler could be used.
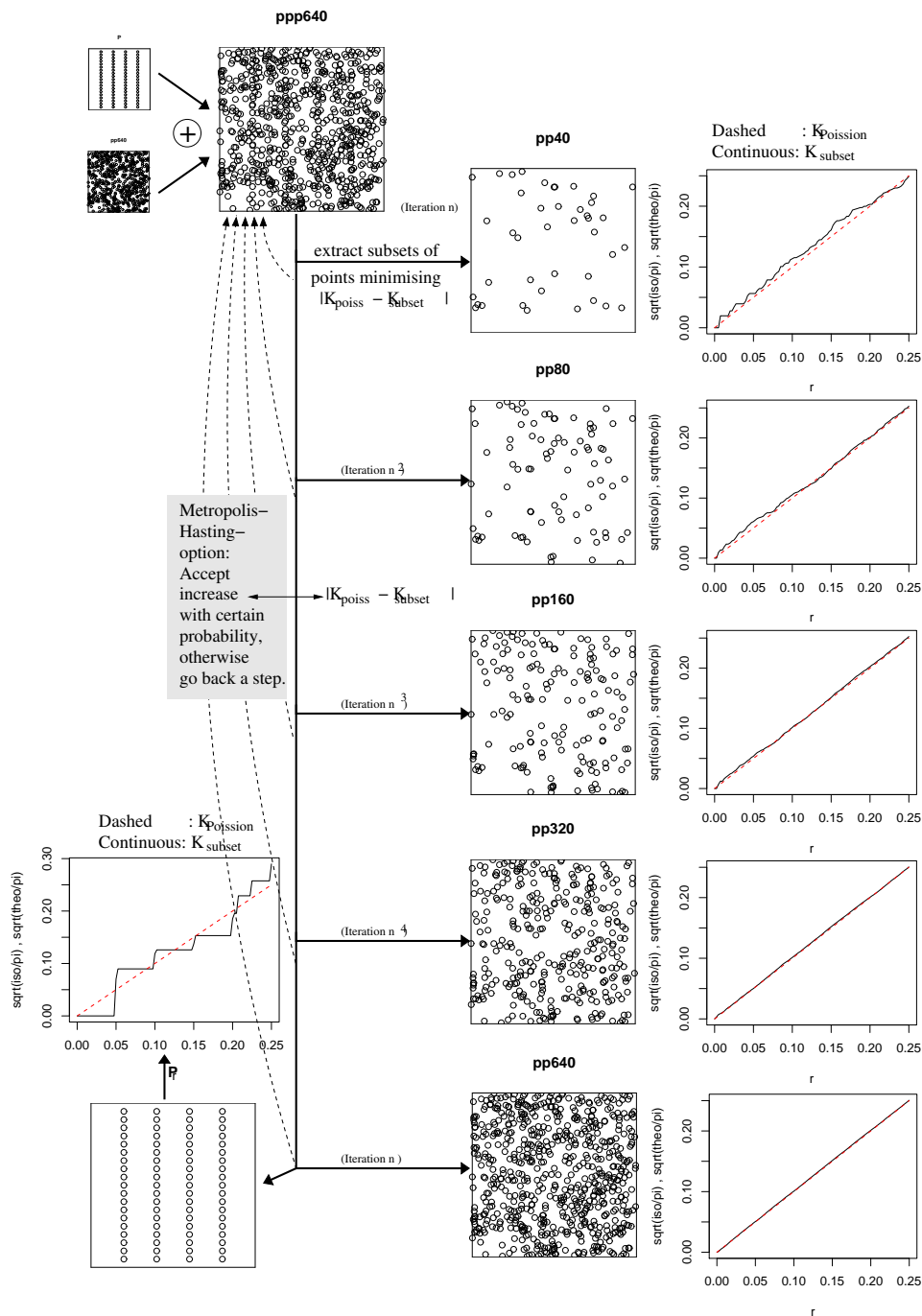
Figure 5.3: Visualisation of a proposed algorithm for elimination of noise induced, random points from a deterministic structure: An iteration includes a selection of randomly chosen points which is added to a temporary point pattern which is subsequently compared to point statistics of a random Poisson process. If the similarity to a Poisson process increases, the selection is accepted. Otherwise, as adaptation of the Metropolis-Hastings algorithm, the selection is accepted only with a certain probability (to be defined by the distance $|K_{Poisson} - K_{Subset}|$), otherwise rejected. (Note: $K(r)$ was transformed to $K'(r) := \sqrt{(K(r)/\pi)}$ for visualisation purposes (for a Poisson process $K'_{Poisson}(r) = r$ holds since $K_{Poisson}(r) = \pi * r^2$))

5.2 Summary of outlook

From the author's point of view the introduction and investigation of Markov techniques to the field of structural characterisation of trabecular networks can be viewed as a start of multiple, possible pathways extending this work.

First, as discussed in this chapter, the application of the methods of this study to in vivo situations may be a first possible goal. This would demand to manage the challenges of high-resolution techniques like decreased signal to noise ratios of in-vivo situations as well as the larger scales of the measurements due to smaller voxel sizes. Certainly, taking biopsies in clinical routine is principally possible, but the degree of invasiveness may be hindering the frequent use of this. Thus, the methods investigated in this study based on biopsies should be transformed to in vivo situations. If successful, this would possibly allow to extend the clinical routine mainly based on bone density measures by structural information.

A further possibility to extend this work would include other modalities like HRMRI, which is under investigation for the possibility to transfer structural characterisations established for Computer Tomography to Magnetic Resonance Tomography [24, 25, 77, 78]. Similarly, an investigation of the usability of the approaches investigated in this study by Micro-MR or HRMRI would be of interest. This would perhaps allow to establish structural measurements by non-radiating techniques.

Finally, as proposed in section 5.1.2.1, Markov techniques may be used to solve further problems not investigated yet: modelling of noise as (marked) point process, regenerating typical representations of healthy or osteoporotic structures, or structures in between these to stages.

The key to success of structural modelling may lie within the capturing of local interactions of structures which is neglected by all integrative approaches simply averaging about the realisation of the stochastical process under investigation. It may be promising to exploit this information capture facility to investigate further pathways within the field of structural research, even behind bony structures: networks and their functions dependent on the network structure can be found multiply in each mammal: the genome, cell systems and their interactions on a biochemical level (e.g. bone remodelling cells like osteoblasts, osteoclasts), hormone systems, nutritional aspects and corresponding organically functions, nervous systems, the brain, etc. Of course, the field of network research contains social systems, epidemic and immunisation networks, traffic networks, economic networks and many more.

Bibliography

[1] S L Silverman. Quality-of-life issues in osteoporosis. *Curr Rheumatol Rep*, 7(1):39–45, Mar 2005.

[2] U Weber and A Schulz. Osteoporose - Ende des therapeutischen Nihilismus. *Der Orthopaede*, 30(7):401, 2001.

[3] L J Melton. Epidemiology of spinal osteoporosis. *Spine*, 22(24 Suppl):2S–11S, Dec 1997.

[4] L Mosekilde, E N Ebbesen, L Tornvig, and J S Thomsen. Trabecular bone structure and strength - remodelling and repair. *J Musculoskelet Neuronal Interact*, 1(1):25–30, Sep 2000.

[5] L J 3rd Melton, S H Kan, H W Wahner, and B L Riggs. Lifetime fracture risk: an approach to hip fracture risk assessment based on bone mineral density and age. *J Clin Epidemiol*, 41(10):985–994, 1988.

[6] A Oden, A Dawson, W Dere, O Johnell, B Jonsson, and J A Kanis. Lifetime risk of hip fractures is underestimated. *Osteoporos Int*, 8(6):599–603, 1998.

[7] T Jalava, S Sarna, L Pylkkanen, B Mawer, J A Kanis, P Selby, M Davies, J Adams, R M Francis, J Robinson, and E McCloskey. Association between vertebral fracture and increased mortality in osteoporotic patients. *J Bone Miner Res*, 18(7):1254–1260, Jul 2003.

[8] M G Glueer, H W Minne, A D Lazarescu, M Pfeifer, and B Begerow. Subjective versus objective quality of life in women with postmenopausal osteoporosis. In *Quality of Life Research*, volume 10, pages 193–306, Amsterdam, The Netherlands, 2001. Springer Science+Business Media B.V., Formerly Kluwer Academic Publishers B.V.

[9] L B Hansen and S F Vondracek. Prevention and treatment of nonpostmenopausal osteoporosis. *Am J Health Syst Pharm*, 61(24):2637–2654, Dec 2004.

[10] T M Link, S Majumdar, S Grampp, G Guglielmi, C van Kuijk, H Imhof, C Glueer, and J E Adams. Imaging of trabecular bone structure in osteoporosis. *Eur Radiol*, 9(9):1781–1788, 1999.

[11] Consensus Development Conference. Nih consens statement. 17(1):1–45, 2000.

[12] M Janet Barger-Lux and Robert R Recker. Bone microstructure in osteoporosis: Transilial biopsy and histomorphometry. *Top Magn Reson Imaging*, 13(5):297–305, Oct 2002.

[13] C M Langton and C F Njeh, editors. *The physical measurement of bone.* IOP Publishing Ltd., 2004.

[14] T C Lee, S Mohsin, D Taylor, R Parkesh, T Gunnlaugsson, F J O'Brien, M Giehl, and W Gowin. Detecting microdamage in bone. *J Anat*, 203(2):161–172, Aug 2003.

[15] L J Dominguez, M Barbagallo, and L Moro. Collagen overglycosylation: A biochemical feature that may contribute to bone quality. *Biochem Biophys Res Commun*, 330(1):1–4, Apr 2005.

[16] H K Genant, M Jergas, L Palermo, M Nevitt, R S Valentin, D Black, and S R Cummings. Comparison of semiquantitative visual and quantitative morphometric assessment of prevalent and incident vertebral fractures in osteoporosis. The Study of Osteoporotic Fractures Research Group. *J Bone Miner Res*, 11(7):984–996, Jul 1996.

[17] M Egermann, J Goldhahn, and E Schneider. Animal models for fracture treatment in osteoporosis. *Osteoporos Int*, Mar 2005.

[18] W S Siu, L Qin, W H Cheung, and K S Leung. A study of trabecular bones in ovariectomized goats with micro-computed tomography and peripheral quantitative computed tomography. *Bone*, 35(1):21–26, Jul 2004.

[19] H Follet, K Bruyere-Garnier, F Peyrin, J P Roux, M E Arlot, B Burt-Pichat, C Rumelhart, and P J Meunier. Relationship between compressive properties of human os calcis cancellous bone and microarchitecture assessed from 2D and 3D synchrotron microtomography. *Bone*, 36(2):340–351, Feb 2005.

[20] L A Feldkamp, S A Goldstein, A M Parfitt, G Jesion, and M Kleerekoper. The direct examination of three-dimensional bone architecture in vitro by computed tomography. *J Bone Miner Res*, 4(1):3–11, Feb 1989.

[21] M A Haidekker, R Andresen, C J Evertsz, D Banzer, and H O Peitgen. Evaluation of the cortical structure in high resolution CT images of lumbar vertebrae by analysing

low bone mineral density clusters and cortical profiles. *Br J Radiol*, 70(840):1222–1228, Dec 1997.

[22] A Mundinger, B Wiesmeier, E Dinkel, A Helwig, A Beck, and J Schulte Moenting. Quantitative image analysis of vertebral body architecture – improved diagnosis in osteoporosis based on high-resolution computed tomography. *Br J Radiol*, 66(783):209–213, Mar 1993.

[23] Y Jiang, J Zhao, D L White, and H K Genant. Micro CT and Micro MR imaging of 3D architecture of animal skeleton. *J Musculoskelet Neuronal Interact*, 1(1):45–51, Sep 2000.

[24] T M Link, S Majumdar, P Augat, J C Lin, D Newitt, Y Lu, N E Lane, and H K Genant. In vivo high resolution MRI of the calcaneus: differences in trabecular structure in osteoporosis patients. *J Bone Miner Res*, 13(7):1175–1182, Jul 1998.

[25] T M Link, K Kisters, M Kempkes, M Kosch, D Newitt, Y Lu, S Waldt, and S Majumdar. Changes in calcaneal trabecular bone structure assessed with high-resolution MR imaging in patients with kidney transplantation. *Osteoporos Int*, 13(2):119–129, 2002.

[26] A M Parfitt. Bone histomorphometry: standardization of nomenclature, symbols and units (summary of proposed system). *Bone*, 9(1):67–69, 1988.

[27] *The Science of Fingerprints*. U.S. Department of Justice, Federal Bureau of Investigation, Washington, DC, USA, 1984.

[28] L Zhang and D Zhang. Characterization of palmprints by wavelet signatures via directional context modeling. *IEEE Trans Syst Man Cybern B Cybern*, 34(3):1335–1347, Jun 2004. Clinical Trial.

[29] M Sengupta and B Karmakar. Mode of inheritance of finger dermatoglyphic traits among Vaidyas of West Bengal, India. *Ann Hum Biol*, 31(5):526–540, Sep 2004.

[30] D R Ashbaugh. Ridgeology. modern evaluative friction ridge identification. http://www.onin.com/fp/ridgeology.pdf.

[31] O Beyer, H-J Girlich, and H-U Zschiesche. *Stochastische Prozesse und Modelle*. Verlag Harri Deutsch, Frankfurt a. Main, 1978.

[32] N Metropolis, A W Rosenbluth, M N Rosenbluth, A H Teller, and E Teller. Equation of state calculations by fast computing machines. *Journal of Chemical Physics*, 21:1087–1092, 1953.

[33] D Mitton, E Cendre, J P Roux, M E Arlot, G Peix, C Rumelhart, D Babot, and P J Meunier. Mechanical properties of ewe vertebral cancellous bone compared with histomorphometry and high-resolution computed tomography parameters. *Bone*, 22(6):651–658, Jun 1998.

[34] G Gimel'farb. *Image Textures and Gibbs Random Fields.* Kluwer Academic Publishers, 1999.

[35] P Brémaud. *Markov Chains.* Springer Verlag, Berlin, Heidelberg, New York, 1999.

[36] M N M van Lieshout. *Markov Point Processes and their Applications.* Imperial College Press, London, 2000.

[37] A A Barker. Monte carlo calculation of the radial distribution functions for a proton-electron plasma. *Australian Journal of Physics*, 18:119–133, 1965.

[38] R Chellappa and A Jain, editors. *Markov Random Fields: Theory and Application.* Academic Press, Boston, 1993.

[39] W Gibbs. *Elementary Principles of Statistical Mechanics.* Yale University Press, 1902.

[40] W. Ebeling, J. Freund, and F. Schweitzer. *Komplexe Strukturen: Entropie und Information.* B. G. Teubner, Stuttgart, Leipzig, 1998.

[41] F P Kelly and B D Ripley. Markov point processes. *Journal of the London Mathematical Society*, 15:188–192, 1993.

[42] A Baddeley and R Turner. Practical maximum pseudolikelihood for spatial point patterns. *Australian and New Zealand Journal of Statistics*, 42:283–322, 2000.

[43] B D Ripley. Modelling spatial patterns. *Journal of the Royal Statistical Society*, 39:172–192, 1977.

[44] A J Baddeley. Spatial sampling and censoring. In O E Barndorff-Nielsen, Kendall W S, and M N M van Lieshout, editors, *Stochastic Geometry: Likelihood and Computation.*, pages 37–78. Chapman and Hall, 1998.

[45] J Ohser. On estimators for the reduced second moment measure of point processes. *Mathematische Operationsforschung und Statistik, Series Statistics*, 14:63–71, 1983.

[46] D Stoyan, W S Kendall, and J Mecke. *Stochastic Geometry and its Applications.* Springer Verlag., 2nd edition, 1995.

[47] D Stoyan and H Stoyan. *Fractals, Random Shapes and Point Fields: Methods of Geometrical Statistics.* John Wiley and Sons., 1994.

[48] N A C Cressie. *Statistics for Spatial Data.* John Wiley and Sons, 1991.

[49] P J Diggle. *Statistical Analysis of Spatial Point Patterns.* Academic Press, 1983.

[50] B D Ripley. *Statistical Inference for Spatial Processes.* Cambridge University Press, 1988.

[51] A Baddeley and R Turner. Spatstat: an R package for analyzing spatial point patterns. *Journal of Statistical Software*, 12(6):1–42, 2005. URL: www.jstatsoft.org, ISSN: 1548-7660.

[52] R Development Core Team. *R: A Language and Environment for Statistical Computing.* R Foundation for Statistical Computing, Vienna, Austria, 2004. ISBN 3-900051-07-0.

[53] R Cowell, A Dawid, S Lauritzen, and D. Spiegelhalter. *Probabilistic Networks and Expert Systems.* Springer Verlag New York, Inc., 1999.

[54] C E Shannon. A mathematical theory of communication. *Bell System Technical Journal*, 27:379, 1948.

[55] H Nyquist. Certain factors affecting telegraph speed. *Bell System Technical Journal*, page 324, 1924.

[56] H Nyquist. Certain topics in telegraph transmission theory. *A.I.E.E Trans.*, 47:617, 1928.

[57] R V L Hartley. Transmission of information. *Bell System Technical Journal*, page 535, 1928.

[58] J Bruske and G Sommer. Topology representing networks for intrinsic dimensionality estimation. In *ICANN*, pages 595–600, 1997.

[59] K Fukunaga and D R Olsen. An algorithm for finding intrinsic dimensionality of data. *IEEE Transactions on Computers*, 20(2):176–183, 1971.

[60] J H Kinney, J S Stolken, T S Smith, J T Ryaby, and N E Lane. An orientation distribution function for trabecular bone. *Bone*, 36(2):193–201, Feb 2005.

[61] G A Fink. *Mustererkennung mit Markov-Modellen.* B. G. Teubner, Stuttgart, Leipzig, 2003.

[62] C E Metz. Basic principles of roc analysis. *Seminars in Nuclear Medicine*, (8):283–298, 1978.

[63] B R McCreadie, R W Goulet, L A Feldkamp, and S Goldstein. Hierarchical structure of bone and micro-computed tomography. In S Majumdar and B K Bay, editors, *Noninvasive Assessment of Trabecular Bone Architecture and The Competence of Bone*, pages 67–83, New York, 2001. Kluwer Academic / Plenum Publishers.

[64] D Marshall, O Johnell, and H Wedel. Meta-analysis of how well measures of bone mineral density predict occurrence of osteoporotic fractures. *BMJ*, 312(7041):1254–1259, May 1996.

[65] Ethel S Siris, Ya-Ting Chen, Thomas A Abbott, Elizabeth Barrett-Connor, Paul D Miller, Lois E Wehren, and Marc L Berger. Bone mineral density thresholds for pharmacological intervention to prevent fractures. *Arch Intern Med*, 164(10):1108–1112, May 2004.

[66] X Banse, J P Devogelaer, E Munting, C Delloye, O Cornu, and M Grynpas. Inhomogeneity of human vertebral cancellous bone: systematic density and structure patterns inside the vertebral body. *Bone*, 28(5):563–571, May 2001.

[67] W Gowin, P I Saparin, J Kurths, and D Felsenberg. Measures of complexity for cancellous bone. *Technol Health Care*, 6(5-6):373–390, Dec 1998.

[68] P Saparin, W Gowin, Kurths J, and D Felsenberg. Quantification of cancellous bone structure using symbolic dynamics and measures of complexity. *Phys. Rev. E*, (58):6449–6459, 1998.

[69] P Saparin, J S Thomsen, S Prohaska, A Zaikin, J Kurths, H-C Hege, and W Gowin. Quantification of spatial structure of human proximal tibial bone biopsies using 3D measures of complexity. *Acta Astronaut*, 56(9-12):820–830, May 2005.

[70] C W Raeth, R A Monetti, D Mueller, H Boehm, Rummeny E J, and T M Link. Comparing nonlinear texture measures for quantifying trabecular bone structures using surrogates. In J M Fitzpatrick and M. Sonka, editors, *Medical Imaging 2004: Image Processing*, volume 5370, pages 207–214, Bellingham, WA, USA, May 2004. International Society for Optical Engineering.

[71] D Mueller, R A Monetti, H Boehm, J Bauer, E J Rummeny, T M Link, and Raeth C W. The 3d-based scaling index algorithm to optimize structure analysis of trabecular bone in postmenopausal women with and without osteoporotic spine fractures. In J M Fitzpatrick and M. Sonka, editors, *Medical Imaging 2004: Image Processing*, volume 5370, pages 225–232, Bellingham, WA, USA, May 2004. International Society for Optical Engineering.

[72] R A Monetti, H Boehm, D Mueller, E J Rummeny, T M Link, and C Raeth. Assessing the biomechanical strength of trabecular bone in vitro using 3d anisotropic

non-linear texture measures: The scaling vector method. In J M Fitzpatrick and M. Sonka, editors, *Medical Imaging 2004: Image Processing*, volume 5370, pages 215–224, Bellingham, WA, USA, May 2004. International Society for Optical Engineering.

[73] H Boehm, T M Link, R A Monetti, D Mueller, E J Rummeny, D Newitt, S Majumdar, and C W Raeth. Application of the minkowski functionals in 3d to high resolution mr images of trabecular bone: Prediction of the biomechanical strength by non-linear topological measures. In J M Fitzpatrick and M. Sonka, editors, *Medical Imaging 2004: Image Processing*, volume 5370, pages 172–180, Bellingham, WA, USA, May 2004. International Society for Optical Engineering.

[74] D C Newitt, S Majumdar, B van Rietbergen, G von Ingersleben, S T Harris, H K Genant, C Chesnut, P Garnero, and B MacDonald. In vivo assessment of architecture and micro-finite element analysis derived indices of mechanical properties of trabecular bone in the radius. *Osteoporos Int*, 13(1):6–17, Jan 2002.

[75] J Tasgal and E M Williams. The effect of prolonged propranolol administration on myocardial transmural capillary density in young rabbits. *J Physiol*, 315:353–367, Jun 1981.

[76] T Hildebrand and P Ruegsegger. Quantification of Bone Microarchitecture with the Structure Model Index. *Comput Methods Biomech Biomed Engin*, 1(1):15–23, 1997.

[77] T M Link and S Majumdar. Osteoporosis imaging. *Radiol Clin North Am*, 41(4):813–839, Jul 2003.

[78] T M Link, J Bauer, A Kollstedt, I Stumpf, M Hudelmaier, M Settles, S Majumdar, E M Lochmueller, and F Eckstein. Trabecular bone structure of the distal radius, the calcaneus, and the spine: which site predicts fracture status of the spine best? *Invest Radiol*, 39(8):487–497, Aug 2004.

Acknowledgments

Erklärung:

Hiermit versichere ich, dass ich die vorliegende Arbeit selbständig verfasst und ausschließlich die angegebenen Hilfsmittel und Quellen verwendet habe.

Haselau, den